

AD A0 67183

LEVEL

33292.000

(2)

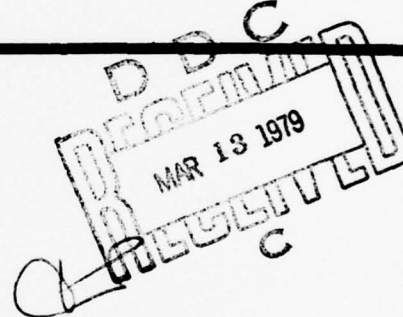
SEMI-ANNUAL TECHNICAL REPORT

1 June 1978 - 30 January 1979

LASER ASSISTED SEMICONDUCTOR DEVICE PROCESSING

DDC FILE COPY

This research was sponsored by the  
Defense Advanced Research Projects  
Agency under ARPA Order No. 3578  
Contract No. MDA903-78-C-0284  
Monitored by: Dr. Isaac Lagnado  
Naval Ocean Systems Center  
Contract Duration: 1 June 1978 - 31 July 1979



DISTRIBUTION STATEMENT A  
Approved for public release  
Distribution Unlimited

TRW Defense and Space Systems Group  
One Space Park  
Redondo Beach, CA 90278

79-08-12-053

(14) TRW -33292-000

(9) SEMI-ANNUAL TECHNICAL REPORT

1 June 1978 - 30 January 1979

(6) "LASER ASSISTED SEMICONDUCTOR DEVICE PROCESSING"

(10) Robert S. White

(12) 172 p.

This research was sponsored by the  
Defense Advanced Research Projects Agency under ARPA Order No. 3578  
Contract No. MDA903-78-C-0284  
Monitored by: Dr. Isaac Lagnado  
Naval Ocean Systems Center  
Contract Duration: 1 June 1978 - 31 July 1979

(15) MDA903-78-C-0284,  
ARPA Order - 3578

The views and conclusions contained in this document are those of the author and should not be interpreted as necessarily representing the official policies, either express or implied, or the Defense Advanced Research Projects Agency or the United States Government.

ACCESSION NO.	
NTIS	REF ID:
000	000
ATTACHMENT	0
1	0
FEB 1979	
AUGUST 1979	
APRIL 1980	
JULY 1980	
OCTOBER 1980	
MARCH 1981	
JUNE 1981	
SEPTEMBER 1981	
DECEMBER 1981	
MAY 1982	
AUGUST 1982	
NOVEMBER 1982	
FEBRUARY 1983	
MAY 1983	
AUGUST 1983	
NOVEMBER 1983	
FEBRUARY 1984	
MAY 1984	
AUGUST 1984	
NOVEMBER 1984	
FEBRUARY 1985	
MAY 1985	
AUGUST 1985	
NOVEMBER 1985	
FEBRUARY 1986	
MAY 1986	
AUGUST 1986	
NOVEMBER 1986	
FEBRUARY 1987	
MAY 1987	
AUGUST 1987	
NOVEMBER 1987	
FEBRUARY 1988	
MAY 1988	
AUGUST 1988	
NOVEMBER 1988	
FEBRUARY 1989	
MAY 1989	
AUGUST 1989	
NOVEMBER 1989	
FEBRUARY 1990	
MAY 1990	
AUGUST 1990	
NOVEMBER 1990	
FEBRUARY 1991	
MAY 1991	
AUGUST 1991	
NOVEMBER 1991	
FEBRUARY 1992	
MAY 1992	
AUGUST 1992	
NOVEMBER 1992	
FEBRUARY 1993	
MAY 1993	
AUGUST 1993	
NOVEMBER 1993	
FEBRUARY 1994	
MAY 1994	
AUGUST 1994	
NOVEMBER 1994	
FEBRUARY 1995	
MAY 1995	
AUGUST 1995	
NOVEMBER 1995	
FEBRUARY 1996	
MAY 1996	
AUGUST 1996	
NOVEMBER 1996	
FEBRUARY 1997	
MAY 1997	
AUGUST 1997	
NOVEMBER 1997	
FEBRUARY 1998	
MAY 1998	
AUGUST 1998	
NOVEMBER 1998	
FEBRUARY 1999	
MAY 1999	
AUGUST 1999	
NOVEMBER 1999	
FEBRUARY 2000	
MAY 2000	
AUGUST 2000	
NOVEMBER 2000	
FEBRUARY 2001	
MAY 2001	
AUGUST 2001	
NOVEMBER 2001	
FEBRUARY 2002	
MAY 2002	
AUGUST 2002	
NOVEMBER 2002	
FEBRUARY 2003	
MAY 2003	
AUGUST 2003	
NOVEMBER 2003	
FEBRUARY 2004	
MAY 2004	
AUGUST 2004	
NOVEMBER 2004	
FEBRUARY 2005	
MAY 2005	
AUGUST 2005	
NOVEMBER 2005	
FEBRUARY 2006	
MAY 2006	
AUGUST 2006	
NOVEMBER 2006	
FEBRUARY 2007	
MAY 2007	
AUGUST 2007	
NOVEMBER 2007	
FEBRUARY 2008	
MAY 2008	
AUGUST 2008	
NOVEMBER 2008	
FEBRUARY 2009	
MAY 2009	
AUGUST 2009	
NOVEMBER 2009	
FEBRUARY 2010	
MAY 2010	
AUGUST 2010	
NOVEMBER 2010	
FEBRUARY 2011	
MAY 2011	
AUGUST 2011	
NOVEMBER 2011	
FEBRUARY 2012	
MAY 2012	
AUGUST 2012	
NOVEMBER 2012	
FEBRUARY 2013	
MAY 2013	
AUGUST 2013	
NOVEMBER 2013	
FEBRUARY 2014	
MAY 2014	
AUGUST 2014	
NOVEMBER 2014	
FEBRUARY 2015	
MAY 2015	
AUGUST 2015	
NOVEMBER 2015	
FEBRUARY 2016	
MAY 2016	
AUGUST 2016	
NOVEMBER 2016	
FEBRUARY 2017	
MAY 2017	
AUGUST 2017	
NOVEMBER 2017	
FEBRUARY 2018	
MAY 2018	
AUGUST 2018	
NOVEMBER 2018	
FEBRUARY 2019	
MAY 2019	
AUGUST 2019	
NOVEMBER 2019	
FEBRUARY 2020	
MAY 2020	
AUGUST 2020	
NOVEMBER 2020	
FEBRUARY 2021	
MAY 2021	
AUGUST 2021	
NOVEMBER 2021	
FEBRUARY 2022	
MAY 2022	
AUGUST 2022	
NOVEMBER 2022	
FEBRUARY 2023	
MAY 2023	
AUGUST 2023	
NOVEMBER 2023	
FEBRUARY 2024	
MAY 2024	
AUGUST 2024	
NOVEMBER 2024	
FEBRUARY 2025	
MAY 2025	
AUGUST 2025	
NOVEMBER 2025	
FEBRUARY 2026	
MAY 2026	
AUGUST 2026	
NOVEMBER 2026	
FEBRUARY 2027	
MAY 2027	
AUGUST 2027	
NOVEMBER 2027	
FEBRUARY 2028	
MAY 2028	
AUGUST 2028	
NOVEMBER 2028	
FEBRUARY 2029	
MAY 2029	
AUGUST 2029	
NOVEMBER 2029	
FEBRUARY 2030	
MAY 2030	
AUGUST 2030	
NOVEMBER 2030	
FEBRUARY 2031	
MAY 2031	
AUGUST 2031	
NOVEMBER 2031	
FEBRUARY 2032	
MAY 2032	
AUGUST 2032	
NOVEMBER 2032	
FEBRUARY 2033	
MAY 2033	
AUGUST 2033	
NOVEMBER 2033	
FEBRUARY 2034	
MAY 2034	
AUGUST 2034	
NOVEMBER 2034	
FEBRUARY 2035	
MAY 2035	
AUGUST 2035	
NOVEMBER 2035	
FEBRUARY 2036	
MAY 2036	
AUGUST 2036	
NOVEMBER 2036	
FEBRUARY 2037	
MAY 2037	
AUGUST 2037	
NOVEMBER 2037	
FEBRUARY 2038	
MAY 2038	
AUGUST 2038	
NOVEMBER 2038	
FEBRUARY 2039	
MAY 2039	
AUGUST 2039	
NOVEMBER 2039	
FEBRUARY 2040	
MAY 2040	
AUGUST 2040	
NOVEMBER 2040	
FEBRUARY 2041	
MAY 2041	
AUGUST 2041	
NOVEMBER 2041	
FEBRUARY 2042	
MAY 2042	
AUGUST 2042	
NOVEMBER 2042	
FEBRUARY 2043	
MAY 2043	
AUGUST 2043	
NOVEMBER 2043	
FEBRUARY 2044	
MAY 2044	
AUGUST 2044	
NOVEMBER 2044	
FEBRUARY 2045	
MAY 2045	
AUGUST 2045	
NOVEMBER 2045	
FEBRUARY 2046	
MAY 2046	
AUGUST 2046	
NOVEMBER 2046	
FEBRUARY 2047	
MAY 2047	
AUGUST 2047	
NOVEMBER 2047	
FEBRUARY 2048	
MAY 2048	
AUGUST 2048	
NOVEMBER 2048	
FEBRUARY 2049	
MAY 2049	
AUGUST 2049	
NOVEMBER 2049	
FEBRUARY 2050	
MAY 2050	
AUGUST 2050	
NOVEMBER 2050	
FEBRUARY 2051	
MAY 2051	
AUGUST 2051	
NOVEMBER 2051	
FEBRUARY 2052	
MAY 2052	
AUGUST 2052	
NOVEMBER 2052	
FEBRUARY 2053	
MAY 2053	
AUGUST 2053	
NOVEMBER 2053	
FEBRUARY 2054	
MAY 2054	
AUGUST 2054	
NOVEMBER 2054	
FEBRUARY 2055	
MAY 2055	
AUGUST 2055	
NOVEMBER 2055	
FEBRUARY 2056	
MAY 2056	
AUGUST 2056	
NOVEMBER 2056	
FEBRUARY 2057	
MAY 2057	
AUGUST 2057	
NOVEMBER 2057	
FEBRUARY 2058	
MAY 2058	
AUGUST 2058	
NOVEMBER 2058	
FEBRUARY 2059	
MAY 2059	
AUGUST 2059	
NOVEMBER 2059	
FEBRUARY 2060	
MAY 2060	
AUGUST 2060	
NOVEMBER 2060	
FEBRUARY 2061	
MAY 2061	
AUGUST 2061	
NOVEMBER 2061	
FEBRUARY 2062	
MAY 2062	
AUGUST 2062	
NOVEMBER 2062	
FEBRUARY 2063	
MAY 2063	
AUGUST 2063	
NOVEMBER 2063	
FEBRUARY 2064	
MAY 2064	
AUGUST 2064	
NOVEMBER 2064	
FEBRUARY 2065	
MAY 2065	
AUGUST 2065	
NOVEMBER 2065	
FEBRUARY 2066	
MAY 2066	
AUGUST 2066	
NOVEMBER 2066	
FEBRUARY 2067	
MAY 2067	
AUGUST 2067	
NOVEMBER 2067	
FEBRUARY 2068	
MAY 2068	
AUGUST 2068	
NOVEMBER 2068	
FEBRUARY 2069	
MAY 2069	
AUGUST 2069	
NOVEMBER 2069	
FEBRUARY 2070	
MAY 2070	
AUGUST 2070	
NOVEMBER 2070	
FEBRUARY 2071	
MAY 2071	
AUGUST 2071	
NOVEMBER 2071	
FEBRUARY 2072	
MAY 2072	
AUGUST 2072	
NOVEMBER 2072	
FEBRUARY 2073	
MAY 2073	
AUGUST 2073	
NOVEMBER 2073	
FEBRUARY 2074	
MAY 2074	
AUGUST 2074	
NOVEMBER 2074	
FEBRUARY 2075	
MAY 2075	
AUGUST 2075	
NOVEMBER 2075	
FEBRUARY 2076	
MAY 2076	
AUGUST 2076	
NOVEMBER 2076	
FEBRUARY 2077	
MAY 2077	
AUGUST 2077	
NOVEMBER 2077	
FEBRUARY 2078	
MAY 2078	
AUGUST 2078	
NOVEMBER 2078	
FEBRUARY 2079	
MAY 2079	
AUGUST 2079	
NOVEMBER 2079	
FEBRUARY 2080	
MAY 2080	
AUGUST 2080	
NOVEMBER 2080	
FEBRUARY 2081	
MAY 2081	
AUGUST 2081	
NOVEMBER 2081	
FEBRUARY 2082	
MAY 2082	
AUGUST 2082	
NOVEMBER 2082	
FEBRUARY 2083	
MAY 2083	
AUGUST 2083	
NOVEMBER 2083	
FEBRUARY 2084	
MAY 2084	
AUGUST 2084	
NOVEMBER 2084	
FEBRUARY 2085	
MAY 2085	
AUGUST 2085	
NOVEMBER 2085	
FEBRUARY 2086	
MAY 2086	
AUGUST 2086	
NOVEMBER 2086	
FEBRUARY 2087	
MAY 2087	
AUGUST 2087	
NOVEMBER 2087	
FEBRUARY 2088	
MAY 2088	
AUGUST 2088	
NOVEMBER 2088	
FEBRUARY 2089	
MAY 2089	
AUGUST 2089	
NOVEMBER 2089	
FEBRUARY 2090	
MAY 2090	
AUGUST 2090	
NOVEMBER 2090	
FEBRUARY 2091	
MAY 2091	
AUGUST 2091	
NOVEMBER 2091	
FEBRUARY 2092	
MAY 2092	
AUGUST 2092	
NOVEMBER 2092	
FEBRUARY 2093	
MAY 2093	
AUGUST 2093	
NOVEMBER 2093	
FEBRUARY 2094	
MAY 2094	
AUGUST 2094	
NOVEMBER 2094	
FEBRUARY 2095	
MAY 2095	
AUGUST 2095	
NOVEMBER 2095	
FEBRUARY 2096	
MAY 2096	
AUGUST 2096	
NOVEMBER 2096	
FEBRUARY 2097	
MAY 2097	
AUGUST 2097	
NOVEMBER 2097	
FEBRUARY 2098	
MAY 2098	
AUGUST 2098	
NOVEMBER 2098	
FEBRUARY 2099	
MAY 2099	
AUGUST 2099	
NOVEMBER 2099	
FEBRUARY 2000	
MAY 2000	
AUGUST 2000	
NOVEMBER 2000	
FEBRUARY 2001	
MAY 2001	
AUGUST 2001	
NOVEMBER 2001	
FEBRUARY 2002	
MAY 2002	
AUGUST 2002	
NOVEMBER 2002	
FEBRUARY 2003	
MAY 2003	
AUGUST 2003	
NOVEMBER 2003	
FEBRUARY 2004	
MAY 2004	
AUGUST 2004	
NOVEMBER 2004	
FEBRUARY 2005	
MAY 2005	
AUGUST 2005	
NOVEMBER 2005	
FEBRUARY 2006	
MAY 2006	
AUGUST 2006	
NOVEMBER 2006	
FEBRUARY 2007	
MAY 2007	
AUGUST 2007	
NOVEMBER 2007	
FEBRUARY 2008	
MAY 2008	
AUGUST 2008	
NOVEMBER 2008	
FEBRUARY 2009	
MAY 2009	
AUGUST 2009	
NOVEMBER 2009	
FEBRUARY 2010	
MAY 2010	
AUGUST 2010	
NOVEMBER 2010	
FEBRUARY 2011	
MAY 2011	
AUGUST 2011	
NOVEMBER 2011	
FEBRUARY 2012	
MAY 2012	
AUGUST 2012	
NOVEMBER 2012	
FEBRUARY 2013	
MAY 2013	
AUGUST 2013	
NOVEMBER 2013	
FEBRUARY 2014	
MAY	

## TABLE OF CONTENTS

<u>SECTION</u>		<u>PAGE</u>
	SUMMARY . . . . .	1
Task 1	LASER INDUCED SURFACE PROCESSING	
1.0	INTRODUCTION . . . . .	3
2.0	LASER HEATING OF SEMICONDUCTORS . . . . .	5
2.1	Summary . . . . .	5
2.2	Introduction . . . . .	6
2.3	Absorption of Laser Light . . . . .	7
2.4	Conversion of Absorbed Photon Energy to Heat . . . . .	10
2.5	Temperature Measurement . . . . .	16
2.5.1	Post-processing Measurement . . . . .	16
2.5.2	Real Time Measurement . . . . .	18
3.0	APPLICATIONS OF LASER INDUCED HEATING . . .	21
3.1	Introduction . . . . .	21
3.2	Laser Anneal of Implanted Gallium Arsenide . . . . .	21
3.3	Ion Implanted Silicon . . . . .	22
3.4	Silicon on Sapphire Experiments . . .	29
3.5	Laser Induced Impurity Diffusion . .	33
3.6	Summary . . . . .	36
Task 2	EVALUATION OF THE LASER BLOW-OFF ION IMPLANTATION SOURCE	
1.0	INTRODUCTION . . . . .	37
2.0	EXPERIMENTAL APPARATUS . . . . .	39
3.0	RESULTS . . . . .	44
	REFERENCES . . . . .	56

APPENDIX A - CONTRIBUTION OF FREE ELECTRONS TO  
OPTICAL ABSORPTION IN SEMICONDUCTORS

APPENDIX B - NUMERICAL SOLUTION OF THERMAL AND  
IMPURITY DIFFUSION DURING LASER-  
INDUCED PROCESSING

APPENDIX C - RUBY LASER SYSTEM USED IN LASER  
PROCESSING EXPERIMENTS

## LIST OF ILLUSTRATIONS

### Task 1

<u>FIGURE</u>		<u>PAGE</u>
1	Plot of $T-T_0$ at $t = t_p$ for GaAs, Normalized to Unit Pulse Energy $E$ , versus Distance from the Irradiated Surface . . . . .	12
2	Plot of $T-T_0$ at $t = t_p$ for Si, Normalized to Unit Pulse Energy $E$ , versus Distance from the Irradiated Surface . . . . .	13
3	Temperature Profiles for GaAs for $\kappa = \text{Constant}$ and $\kappa = \kappa(T)$ . . . . .	15
4	Scope Traces of Laser Pulse and Photodiode Forward Voltage at Constant Current. . . . .	20
5	Reciprocal of Sheet Resistance versus Arsenic Implant Fluences as a Function of Thermal Treatment . . . . .	24
6	Reverse Leakage Current Measured at $V = -15$ Volts for Laser Annealed and Thermal Annealed P and As Implanted Silcicon Planar Diodes . . . . .	28
7	Schematic of Experimental Set-up for Laser Blow-Off and for Laser Treatment of Thin Silicon Layers Obtained in the Blow-off Step. . . . .	30
8	Silicon Deposit on Sapphire with $20 \text{ j/cm}^2$ and $50 \text{ j/cm}^2$ Laser Energy . . . . .	31
9	Photographs of GaAs Surface After Laser Blow-off and GaAs Deposition on Glass as in Step 1 of Figure 7 with the Glass Substrate Replacing the Sapphire . . . . .	32
10	High Magnification Photograph of GaAs on Glass . . . . .	34

Task 2

<u>FIGURE</u>		<u>PAGE</u>
1a	Schematic Diagram of Laser Blow-Off Ion Implantation System . . . . .	40
1b	Photograph of Laser Blow-Off Ion Implantation System . . . . .	41
2	Geometric Arrangement for the Theoretical Model and Experiment . . . . .	47
3	Theoretical Curves for Beam Particle Current Density J versus Time, Normalized to the Time at Which J is a Maximum . . . . .	49
4	Unaccelerated Boron Ion Pulses . . . . .	50
5	Theoretical Curves for $\int_0^{\infty} J dt$ versus Detector Angle $\theta$ at $0^{\circ}$ Constant Distance r and Normalized to the Value for $\theta = 0$ . . . . .	51
6	Applied Research Laboratories IMMA (Ion Microprobe Mass Analyzer) . . . . .	54

## SUMMARY

The objective of Task 1 of this program is to evaluate and characterize laser induced processing of semiconductor materials and devices, with emphasis on the III-V compound series. The work described was performed under contract number MDA903-78-C-0284 during the period of June 1978 to 31 December 1978.

Laser processing comprises three principal phenomena: photon absorption, conversion of absorbed photon energy to heat, and material response to the thermal stimulus. We are examining each of these phenomena in detail both theoretically and experimentally.

We have developed a model that includes, in addition to normal band-to-band absorption, absorption due to laser generated free carriers. The model assumes that the two effects are additive, and that the band-to-band absorption coefficient is constant and equal to its small signal value. We have found that, under these conditions, band-to-band absorption predominates when the laser wavelength is shorter than the bandgap wavelength.

We regard the use of the small signal absorption coefficient, however, to be suspect, especially when the laser wavelength is close to the bandgap wavelength. This issue will be addressed in our on-going analytical studies.

The conversion of photon energy to thermal energy is a two step process. In the first step the photon energy in excess of the bandgap energy is converted directly into lattice heat in times of the order of  $10^{-13}$  seconds; it is therefore deposited in the immediate vicinity of the photon absorption. For GaAs irradiated by ruby laser light, this step accounts for approximately 40% of the absorbed ruby laser energy. The second step, non-radiative recombination of the laser created hole-electron pairs, may, in high quality material, occur far from where the photons were absorbed.

We have developed a thermal model that treats the spatial dependence of each step. The results described in this report are valid for poor quality or damage (as by heavy ion implantation) material. Predictions for laser irradiated, high quality, long carrier lifetime material will be presented in the final report.

We have experimentally demonstrated the superiority of laser processing over standard thermal processing for a number of silicon and gallium arsenide material configurations. We have also devised an experiment having the potential for in-situ real-time measurements of the laser induced material temperatures.

The objective of Task 2 is to evaluate the laser blow-off ion implantation source.

This new ion implantation technique utilizes pulsed laser irradiation of a solid surface of pure dopant material to produce a high temperature plasma of dopant ions. The plasma expands into vacuum, reducing the charge density to the point where an externally applied electric field can be used to extract ions from the plasma. In principle these ions can be accelerated to an arbitrarily high energy and can be used to implant semiconductor materials. A subtle aspect of this method is the pulsed nature of the ion beam current. For reasonable values of ion energy and ion areal density, it appears that annealing temperatures can be reached in the implanted regions for very short times at each laser pulse.

Measurements have been made and results obtained largely in the order of laser performance, implant plasma production, plasma plume characteristics, ion current and areal uniformity, implant material deposition without acceleration, and implant with high energy implant ions.

## Task 1

### LASER INDUCED SURFACE PROCESSING

#### 1.0 INTRODUCTION

The application of laser annealing to semiconductor device processing has attracted the attention of researchers throughout the world. During 1978 a considerable amount of experimental data was disclosed. In addition to three major conferences in Catania, Sicily, Budapest, Hungary and Boston, numerous papers appeared. Two reviews<sup>1,2</sup> pointed up the potential of laser processing, twenty-one short papers<sup>3-23</sup> in Applied Physics Letters presented data and one extensive investigation was described in the Journal of Applied Physics.<sup>24</sup>

Most of the studies involved annealing ion implanted surfaces, although two described laser-assisted doping,<sup>8,10</sup> two described the regrowth of deposited amorphous silicon films,<sup>11,12</sup> one the effect of annealing doped polycrystalline silicon layers,<sup>22</sup> and one the reaction of metal films with the silicon underneath.<sup>22</sup>

The lasers used were pulsed ruby,<sup>3,8,9,16,24</sup> pulsed Nd:YAG (References 6,7,10,11,12,13,19,20 and 22) cw Ar<sup>4,5,14,15,18</sup> and cw Nd:YAG.<sup>21</sup> Since the radiant energy does not have to be coherent, two of the studies investigated the use of flash lamps,<sup>7,23</sup> and found that they did indeed result in an annealing effect.

The majority of the studies of laser annealing of ion implanted material was performed on heavily damaged material. The implant energies and dosages employed were sufficient to induce amorphous surface layers. Irradiation of the surface by high power pulsed lasers caused melting of the amorphous layer, and liquid phase epitaxial regrowth occurred during re-solidification. Redistribution of the implanted dopant also took place. Of particular interest is the observation that the regrown layers are largely free of crystalline defects.

When annealing is accomplished through the use of scanned cw Argon ion lasers, epitaxy occurs without a redistribution of the implanted species. This suggests solid phase epitaxy, rather than liquid phase, is the regrowth mechanism.

The production potential of laser processing has not as yet been established. To do so, the rather spectacular laboratory demonstrations must be systematically studied and the critical processing parameters characterized. For example, although a number of thermal models predicting laser induced temperature profiles are available, there exists no direct experimental confirmation of these predictions.

Analytical and experimental studies of the laser induced temperature profiles represent a significant fraction of our effort. In addition, we report the results of a number of exploratory material and device processing experiments.

## 2.0 LASER HEATING OF SEMICONDUCTORS

### 2.1 Summary

Laser heating of semiconductors involves a number of physical mechanisms which may be operative in parallel or in sequence. It is conceptually convenient to categorize the process as comprising two major steps or events:

- absorption of the laser light, and
- conversion of the absorbed optical energy to heat.

The absorption of the laser light by a semiconductor may be due to a photon-phonon interaction, a photon-free carrier interaction, a photon-bound carrier interaction creating hole-electron pairs, or a combination of these mechanisms. When the photon energy exceeds the semiconductor bandgap energy, the dominant mechanism at low light intensities is the creation of hole-electron pairs. At the high intensities employed in laser processing, however, photogenerated carriers may become extremely numerous, approaching densities of  $10^{20}/\text{cm}^3$ , and must be considered as possible sources of absorption.

We have analyzed free carriers absorption, and conclude that it is sufficiently small to be neglected in the presence of band-to-band absorption. At wavelengths longer than the bandgap energy, however, it is the principal absorption mechanism, and may have a coefficient as large as  $10^3 \text{ cm}^{-1}$ . A detailed discussion of this phenomenon is given in Section 2.3 and Appendix A.

Absorbed optical energy is converted into heat in two ways:

- relaxation of highly excited electron-hole pairs to thermodynamic equilibrium with the lattice,
- non-radiative recombination of electron-hole pairs.

The first mechanism takes place rapidly, imparting the excess energy to the lattice in the immediate vicinity of the photon absorption, and its contribution to lattice heating is

significant ( $\sim 37\%$  and  $\sim 20\%$  for ruby light absorbed in silicon and gallium arsenide, respectively).

Non-radiative recombination in high quality materials is a relatively slow process. Recombination may, therefore, take place over a region considerably larger than the optical absorption volume as a result of carrier diffusion during the recombination lifetime. Thus, when diffusion is appreciable, the energy deposited per unit volume, and hence the temperature, are less than those estimated assuming no charge diffusion.

The thermal model presented in Section 2.4 and Appendix B does not include charged particle diffusion. Thus, it is primarily applicable to short lifetime material. A more complete model has been formulated but not as yet programmed.

We have applied the results of the thermal analysis to the study of species diffusion, and conclude that the effect of single pulse heating is insignificant.

Laser processing is, therefore, precluded as a means of obtaining sensible solid phase diffusion. Species diffusion in laser induced liquid phases is not treated here.

An experimental effort to obtain data on temperatures in laser irradiated semiconductor materials has not been successful. A brief discussion of the experiment and reasons for its lack of success are given in Section 2.5. This section also contains a description of a proposed new experiment, which if successful, will provide temperature-time histories at a finite number of planes located beneath the surface of the irradiated material.

## 2.2 Introduction

Laser heating of a solid is the transformation of photon energy to phonon energy. The possible mechanisms are numerous; their applicability depends upon the particular system, and they

may be operative in parallel or in sequence. The following sections present detailed discussions of the mechanisms of laser heating of semiconductors.

### 2.3 Absorption of Laser Light

Optical energy may be absorbed by a material through either of the following reactions:

- photon energy  $\neq$  phonon energy
- photon energy  $\neq$  charge carrier energy  $\neq$  phonon energy.

The first, important at long wavelengths (GaAs and Si,  $\lambda \gtrsim 20 \mu$ ), will not be considered here because high power lasers operating in this spectral range do not exist. The second, in which the photons interact with the electron structure of the material, is important to laser heating of semiconductors, and will be discussed in detail.

#### Photon Energy $\neq$ Charge Carrier Energy:

This transfer may occur by direct free carrier absorption, or, if the photon energy exceeds the semiconductor bandgap energy, by hole-electron pair creation. Free carrier absorption is normally of minor importance compared to pair creation. It can, however, dominate if the photon energy is less than the bandgap energy, and indeed is responsible for thermal runaway in germanium windows used in high power infrared lasers. Heating by free carrier absorption in germanium increases the number of thermally excited carriers, thereby increasing the absorption. This sequence results ultimately in catastrophic failure of the window.

Free carrier absorption can also dominate when the photon energy is greater than the bandgap energy, provided the laser power is high enough to first elevate the carrier concentration sufficiently by pair creation. Laser processing frequently employs power densities of  $10^7$  to  $10^8$  watts/cm<sup>2</sup>,

corresponding to pair creation rates of the order of  $10^{25} \text{ sec}^{-1}$  to  $10^{26} \text{ sec}^{-1}$ .\* We have calculated carrier concentrations, taking into account losses due to recombination and charge carrier diffusion. The approach and results are reviewed briefly in the next paragraph; the analysis is in Appendix A.

The instantaneous concentration of photogenerated carriers  $n(x,t)$  in a semiconductor is the solution to the transport equation,

$$\frac{\partial n}{\partial t} = g - \frac{\Delta n}{\tau} + \frac{D \partial^2 n}{\partial x^2} \quad (1)$$

where  $\tau$  and  $D$  are the minority carrier lifetime and diffusion constant, respectively, and  $g$  is the photogeneration rate given by

$$g = \alpha F e^{-\alpha x},$$

where  $\alpha$  is the optical absorption coefficient and  $F = F(t)$  is the photon flux incident on the semiconductor (reflection is ignored). We have calculated the carrier concentrations,  $n(x,t)$  for a variety of values of laser intensity and pulse length, of carrier photogeneration rate, and of times required for a carrier to recombine and to diffuse an optical absorption distance. Our predictions span a range from  $10^{17} \text{ cm}^{-3}$  to  $10^{20} \text{ cm}^{-3}$ . We have also estimated the free carrier absorption coefficient at concentrations in this range for several laser wavelengths, and compared it with the corresponding band-band coefficient. Our estimates, shown in Table 1, indicate that band-band absorption remains the primary mechanism for ruby laser light on Si, GaAs and Ge, and for Nd laser light on Ge and Si (except, perhaps,

---

\* In the absence of losses pair creation at these rates would deplete the valance band in very short times.

Table 1. Absorption Coefficient  $\alpha$  Associated With Free Carriers Compared to Bandedge Absorption  $\alpha$ .  
 n is the carrier density and  $\omega_p$  is the material plasma frequency.

Semicon- ductor	n( $\text{cm}^{-3}$ )	$\omega_p$ (rad)	Absorption Coefficient $\alpha(\text{cm}^{-1})$			
			Ruby $\alpha_n$	$\alpha$	$N_d$ $\alpha_n$	$\text{CO}_2$ $\alpha_n$
Si	$10^{17}$	$7 \times 10^{12}$	$10^{-3}$		$3 \times 10^{-3}$	$3 \times 10^{-1}$
	$10^{18}$	$2 \times 10^{13}$	$10^{-2}$	$\sim 5 \times 10^3$	$3 \times 10^{-2}$	3
	$10^{19}$	$7 \times 10^{13}$	$10^{-1}$		0.3	$3 \times 10^1$
	$10^{20}$	$2 \times 10^{14}$	1		3	$3 \times 10^2$
GaAs	$10^{17}$	$2 \times 10^{13}$	$1.6 \times 10^{-2}$		$4 \times 10^{-2}$	4
	$10^{18}$	$7 \times 10^{13}$	$1.6 \times 10^{-1}$	$\sim 5 \times 10^4$	$4 \times 10^{-1}$	$4 \times 10^1$
	$10^{19}$	$2 \times 10^{14}$	1.6		4	$4 \times 10^2$
	$10^{20}$	$7 \times 10^{14}$	16		40	$4 \times 10^3$
Ge	$10^{17}$	$5 \times 10^{12}$	$2 \times 10^{-4}$		$6 \times 10^{-4}$	$6 \times 10^{-2}$
	$10^{18}$	$1.5 \times 10^{13}$	$2 \times 10^{-3}$		$6 \times 10^{-3}$	$6 \times 10^{-1}$
	$10^{19}$	$5 \times 10^{13}$	$2 \times 10^{-2}$	$\sim 10^5$	$6 \times 10^{-2}$	$\sim 10^4$
	$10^{20}$	$1.5 \times 10^{14}$	$2 \times 10^{-1}$		$6 \times 10^{-1}$	$6 \times 10^{-1}$

at carrier densities in excess of  $10^{20} \text{ cm}^{-3}$ ). Free carrier absorption, however, dominates at CO<sub>2</sub> wavelengths for all three materials and at Nd wavelengths for GaAs, and, as discussed earlier, is the initiating mechanisms for thermal runaway.

#### 2.4 Conversion of Absorbed Photon Energy to Heat

The laser induced temperature distribution in a semiconductor is described in a one-dimensional approximation by the thermal transport equation,

$$\frac{\partial T}{\partial t} - \frac{\partial}{\partial x} \left[ \frac{K(T)}{C_p(t)} \frac{\partial T}{\partial x} \right] = \frac{S(x,t)}{C_p} , \quad (2)$$

where C<sub>p</sub>(t) and K(t) are the specific heat and thermal conductivity, respectively, and S(x,t) is the heat source and power density. When the laser photon energy exceeds the bandgap energy, S(x,t) must be decomposed into two terms. The first describes heating due to relaxation of carriers from photon-excited distributions to quasi-thermal distributions within the conduction and valence bands. It is given approximately by

$$S_1(x,t) = (hv - E_g) \propto F(t) e^{-\alpha x} , \quad (3)$$

where hv is the laser photon energy and E<sub>g</sub> is the bandgap energy. S<sub>1</sub>(x,t) is proportional to the optical absorption coefficient, and therefore has the same spatial dependence, because excited carriers relax in times of the order of  $10^{-13}$  seconds, too short for significant spatial redistribution.

The second heat source term, describing nonradiative hole-electron recombination, is

$$S_2(x,t) = E_g \frac{[n(x,t) - n_0]}{\tau} , \quad (4a)$$

where  $n_0$  is the equilibrium carrier density,  $\tau$  is the recombination lifetime, and  $n(x,t)$  is the solution to (1), the electron transport equation. This term must be included for materials characterized by long carrier lifetimes and diffusion lengths such as high quality silicon.

Poor quality materials, such as ion-implant damaged Si or GaAs, have short diffusion lengths; therefore for them  $S_2(x,t)$  like  $S_1(x,t)$ , is proportional to the optical absorption coefficient,

$$S_2(x,t) = E_g \alpha F(t) e^{-\alpha x} , \quad (4b)$$

and Equation (2) may be written as

$$\frac{\partial T}{\partial t} - \frac{\partial}{\partial x} \left[ \frac{\kappa(T)}{C_p(T)} \frac{\partial T}{\partial x} \right] = \frac{h\nu\alpha F(t) e^{-\alpha x}}{C_p(T)} \quad (5)$$

Numerical solutions to Equation 5 for silicon and gallium arsenide are given in Appendix B. These solutions are for  $C_p$  constant,  $\kappa = \kappa(T)$  as obtained from empirical data and a laser pulse shape given by,

$$F(t) = \begin{cases} F_0 \left[ 1 - \left( \frac{t-t_m}{t_m} \right)^2 \right] & 0 < t < t_m \\ F_0 \exp \left[ - \left( \frac{t-t_m}{t_m} \right)^2 \right] & t > t_m \end{cases}$$

The pulse length  $t_p$  is defined by  $F(t_p) = F(t_m)/2$  where  $t_p > t_m$ . Figures 1 and 2 derived from Figures 4, 5, 6 and 8, 9 and 10 of Appendix B show temperature profiles at  $t = t_p$  for various values of  $t_p$ .

---

\* Because of the temperature dependence of  $\kappa$  these curves are accurate only for the pulse energies given in Figures 8, 9, and 10. Scaling to different energies will give only approximate temperatures. This is especially true for the long pulse lengths, where thermal conductivity has a significant role in determining the temperature distribution.

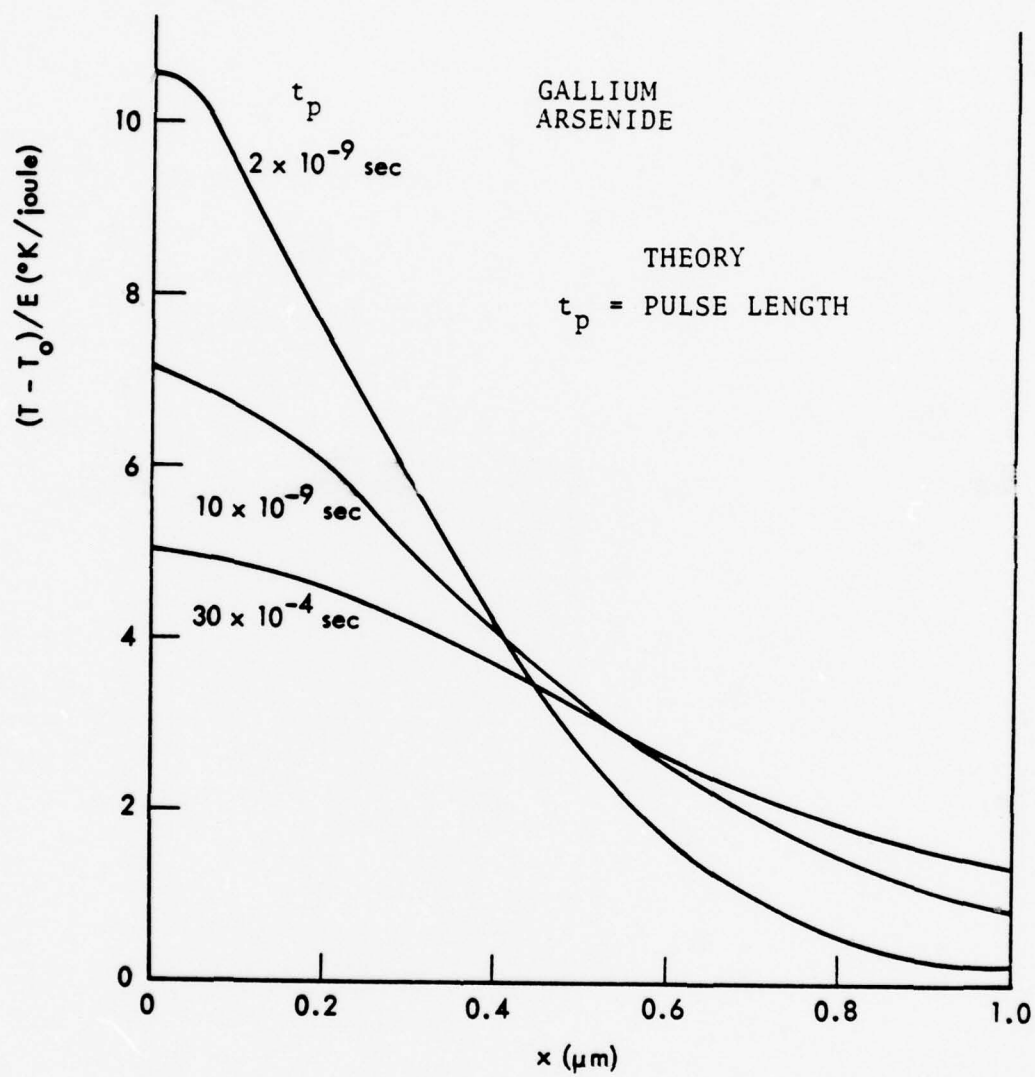


Figure 1. Plot of  $T - T_0$  at  $t = t_p$  for GaAs, Normalized to Unit Pulse Energy  $E$ , versus Distance from the Irradiated Surface.  $T_0$  is the ambient temperature of the sample.

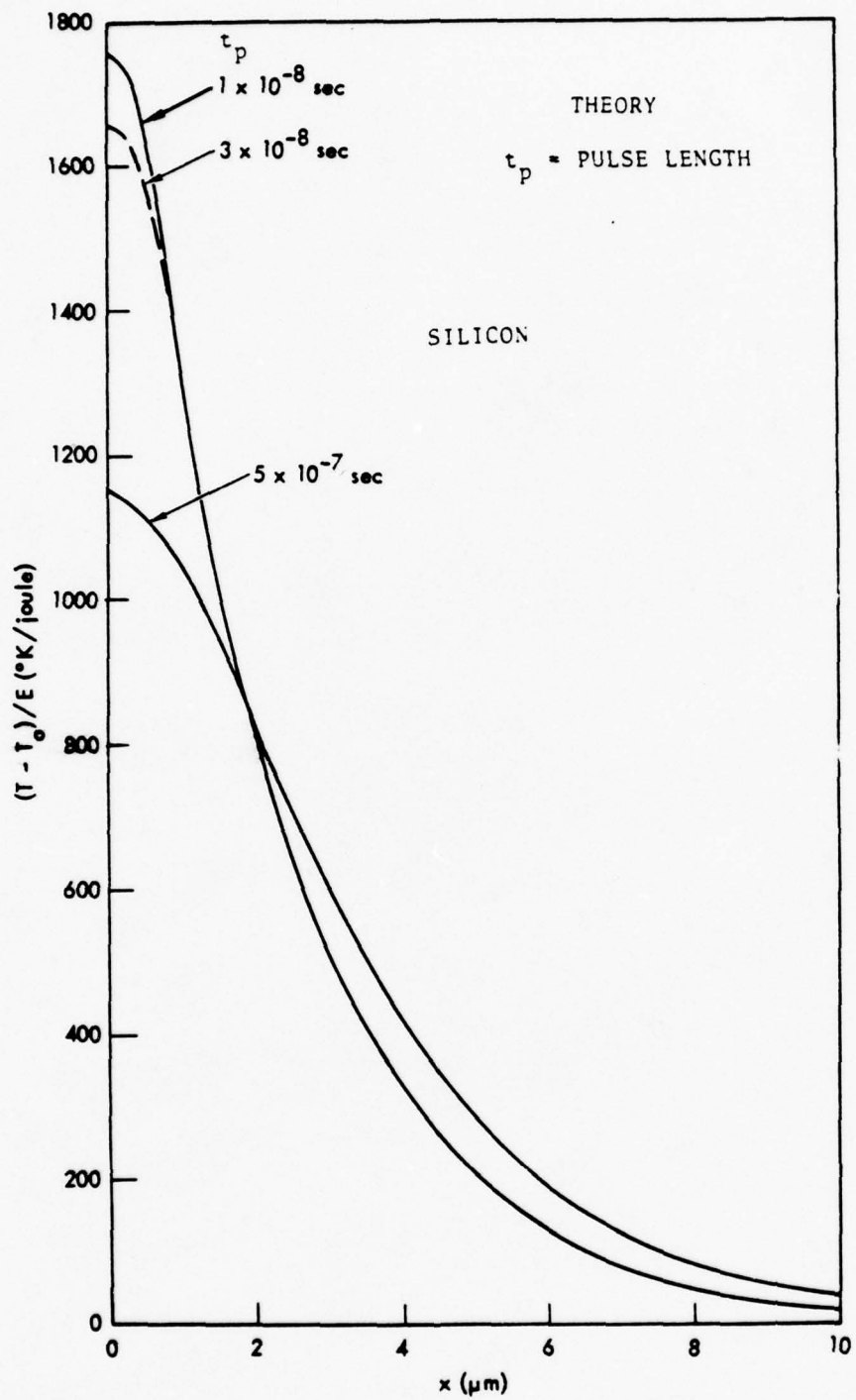


Figure 2. Plot of  $T - T_0$  at  $t = t_p$  for Si, Normalized to Unit Pulse Energy  $E$ , versus Distance from the Irradiated Surface.  $T_0$  is the ambient temperature of the Sample.

These curves demonstrate the efficiency of short pulses in producing high surface temperature gradients. A pulse is defined as short if its length is less than or equal to the time  $t = C_p / \kappa \alpha^2$ , it takes the deposited heat to diffuse one optical absorption length. For ruby laser wavelengths, pulse lengths of the order of  $5 \times 10^{-9}$  sec and  $100 \times 10^{-9}$  sec for GaAs and Si respectively, satisfy this requirement. For Nd wavelengths in silicon, the absorption depth  $1/\alpha$  is approximately 300 microns and pulse lengths of the order of  $10^{-3}$  seconds may be considered short.

Figure 3 derived from Figures 8 and 8a of Appendix B, show the effect of assuming  $\kappa$  is constant in temperature. The thermal conductivities of silicon and gallium arsenide decrease with increasing temperature. Therefore, for a constant input flux, higher temperature gradients and higher surface temperatures must be established to maintain continuity of power flow within the sample as the surface is heated. A long pulse length was chosen for Figure 3 to emphasize the effect of neglecting the temperature dependence of  $\kappa$ . If the pulse length is short compared to thermal diffusion times, thermal conductivity has minimal effect on the initial temperature profiles, as evidenced by the top two curves of Figure 2.

In summary, our analyses have shown:

- Bandgap absorption predominates over free carrier absorption when  $h\nu > E_g^+$ .
- Laser heating efficiency, defined as the ratio of maximum surface temperature to laser pulse energy, increases with decreasing pulse length.

---

<sup>†</sup> Nd irradiation in silicon is perhaps a borderline case because of the small separation between the photon energy and the bandgap energy.

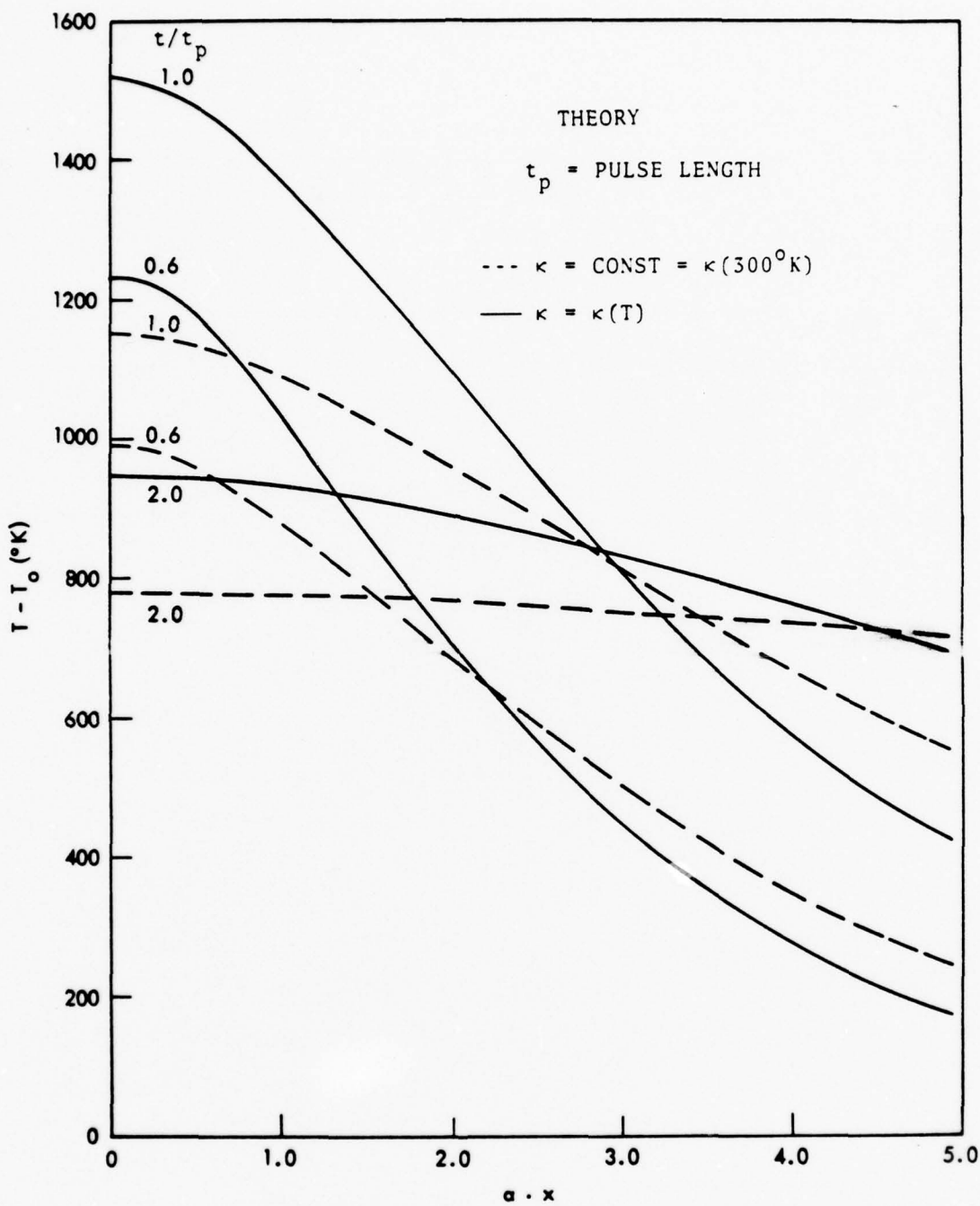


Figure 3. Temperature Profiles for GaAs for  $\kappa = \text{Constant}$  and  $\kappa = \kappa(T)$ . Laser pulse power is  $10^7$  watts/cm<sup>2</sup> and its pulse length is  $3 \times 10^{-8}$  seconds.

- The diffusion of photogenerated charge carriers can reduce the thermal energy deposition density in the semiconductor, a significant effect in high quality material.
- Temperature profile estimates based on the assumption of constant thermal conductivity  $\kappa$  differ significantly from those derived on the basis of  $\kappa = \kappa(T)$ .

## 2.5 Temperature Measurement

We have performed two different kinds of experiments to determine laser induced temperature profiles; both are based on electrical measurements. The first uses thermally influenced properties measured after the completion of laser processing; the second provides the real-time temperature variation during the laser pulse.

### 2.5.1 Post-processing Measurement

Neutron bombardment transmutes one of the naturally occurring isotopes of silicon to phosphorus, which as an impurity in a silicon crystal, can be electrically activated by heating. The distribution of activated phosphorus is then a measure of the temperature history of the crystal after the neutron bombardment; it can be determined as a function of depth from measurements of the spreading resistance. Therefore, the temperatures achieved in silicon crystals during laser processing can, in principle, be inferred afterwards from electrical measurements, provided the crystal has previously been prepared by neutron irradiation.

In our experiment high resistivity ( $10^4 \Omega\text{-cm}$ ) intrinsic silicon samples were prepared by neutron bombardment. Because the transmutable isotope is uniformly distributed and the sample thicknesses were much less than the neutron mean free path, the

resulting phosphorus distributions were assumed to be uniform. A number of the samples were activated by oven annealing at various temperatures and for varying lengths of time. Their resistivities were then measured, and the activation energy calculated from the measurements.

The remaining samples were irradiated with  $2.5 \text{ J/cm}^2$  to  $3.5 \text{ J/cm}^2$  of ruby laser light. According to our thermal model the silicon surface should have approached or exceeded melting temperature. Nevertheless, spreading resistance data contained no evidence of phosphorus activation, and microscopic surface examination revealed only small area, localized melting.

The failure to achieve uniformly high surface temperatures can be explained in terms of charge carrier diffusion. Because of the high quality of the silicon substrates, the lifetimes and hence the diffusion lengths, of the photogenerated carriers are probably quite large. Thus, as discussed in Section 2.4, the absorbed laser energy is deposited over a larger volume than the absorption volume and the temperature elevation is lessened. The observed local surface melting could be due to the existence of discrete defects acting as non-radiative recombination centers.

As a preliminary test of the above interpretation, we repeated the experiment with silicon in which surface damage had been introduced to decrease the lifetimes and diffusion distances of photogenerated carriers; the surface damage was introduced by implanting neon ions with a fluence of  $10^{15} \text{ cm}^{-2}$ . This time we found surface activation at  $1.5 \text{ J/cm}^2$  of laser energy density, supporting the carrier diffusion explanation.

We are continuing these experiments with the emphasis on achieving high temperatures in high quality silicon. Increasing the laser flux by focusing the beam is the most direct approach, but is limited to increases of about a factor of 4 because of the need to maintain a processed area of approximately  $0.25 \text{ cm}^2$ .

for measurement purposes. Other approaches, such as decreasing the carrier lifetime through ion implantation, will also be considered.

### 2.5.2 Real Time Measurement

The temperature at a fixed distance inside a semiconductor can be measured during laser pulse illumination by embedding a planar p-n junction in it, and monitoring the junction's diode characteristics. The forward biased diode current is

$$I = I_0(T) [\exp(eV/kT) - 1] , \quad (6)$$

with

$$I_0(T) \sim \exp(-E_g/kT) ,$$

where  $E_g$  is the bandgap energy,  $k$  is Boltzmann's constant, and  $V$  is the voltage applied to the diode. It follows from (6) that, if the diode current is kept fixed, the variation of the voltage with temperature is given by

$$\frac{dV}{dT} = -2 \times 10^{-3} \text{ volts}/^\circ\text{C} . \quad (7)$$

This value is independent of the semiconductor material up to temperatures of the order of  $300^\circ\text{C}$  to  $500^\circ\text{C}$ , and has been experimentally verified. Thus, by monitoring the diode voltages under fixed current conditions and using Equation (7), one can follow the temperature variation at known junction depths.

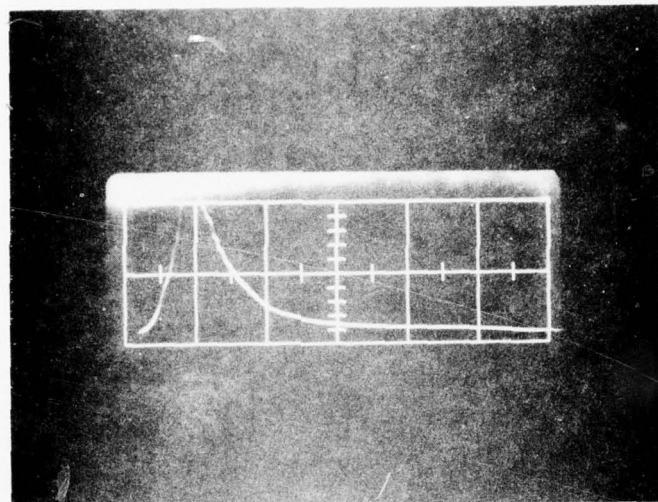
The diode voltage will be influenced by photogenerated charges appearing at the junction, and this effect must be distinguished from the thermal effect. A natural separation will probably occur because of the difference between the diffusion or drift times of the carriers and the diffusion time of the thermal pulse. Interference between the two effects may be further minimized by such methods as using material with carrier lifetimes short enough to prevent their arrival at the junction.

A preliminary experiment has been performed. A commercial silicon solar cell was irradiated with pulsed (10 nsec) ruby radiation while being operated as a constant current forward biased diode. Figure 4b shows the diode voltage as a function of time. The voltage pulse resulting from the photogenerated carriers is not visible in this photograph, but appears as a narrow positive peak at the beginning of the trace. The small negative peak occurring at approximately 10  $\mu$ sec is in the direction expected if the junction were heated.

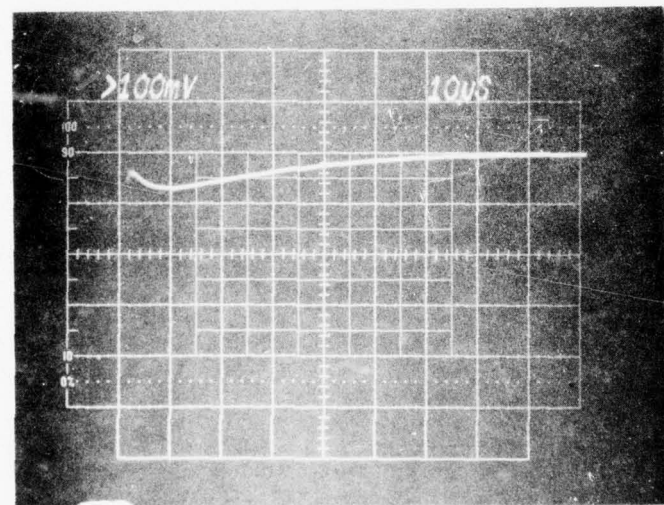
The appearance of the negative peak at times long after the termination of the laser pulse, and the fact that it is negative in contrast to the positive optical signal are encouraging. Since we have no information on the structure of this cell, however, we refrain from analysing these data in greater detail.

We shall obtain planar diodes of known geometry, and repeat this experiment. If we are successful in this approach, we shall obtain the temperature history at a known distance from the surface, which may then be compared with theoretical predictions.

To summarize, the preliminary experimental efforts to determine the laser induced temperature profiles did not yield positive results. We believe that one experiment failed due to insufficient laser power. The second showed an effect that may be temperature related, but we have insufficient data to confirm our hypothesis. We plan to correct the deficiencies of these two experiments and continue this study.



(a)



(b)

Figure 4. Scope Traces of Laser Pulse (a) and Photodiode Forward Voltage (b) at Constant Current. Sweep rates are  $10^{-9}$  sec/div and  $10^{-9}$  sec/div respectively.

### 3.0 APPLICATIONS OF LASER INDUCED HEATING

#### 3.1 Introduction

Thermal processing of semiconductors is widely employed in the fabrication of solid state devices. Examples include annealing and electrical activation of dopant impurities, sintering of evaporated contacts and diffusion of dopants. In each case the processing results in the modification of the surface or a region located within a few microns of the surface. Because laser heating is similarly localized, it should be an ideal way to accomplish these various processings. We have investigated several such applications, and the results are described below. The laser employed was a Q-switched ruby oscillator and amplifier combination. This system delivers  $0\text{-}3 \text{ j/cm}^2$  (unfocused) in a  $10^{-8}$  second pulse at the rate of one pulse per minute. A complete description of the ruby system is given in Appendix C.

#### 3.2 Laser Anneal of Implanted Gallium Arsenide

Two sets of experiments have been performed on Si implanted GaAs wafers, and both sets indicate successful activation of the implanted species over a broad range of laser pulse energy settings.

The samples were from a semi-insulating GaAs wafer which had been coated with a three part thin film -  $\text{Si}_3\text{N}_4$ ,  $\text{SiO}_2$ , Al. This film was subsequently patterned to give holes approximately 100 mils x 200 mils in the film. The wafer was then ion implanted with  $3 \times 10^{13} \text{ P}$  followed by  $3 \times 10^{13} \text{ Si}$  with energies about 200 keV.

This wafer was broken and 1 part was laser annealed in air ambient with energies from  $\sim .4$  to  $\sim 2 \text{ j/cm}^2$ . The second part was laser annealed in vacuum with pulse energies ranging from  $\sim .1$  to  $\sim 3 \text{ j/cm}^2$ . These samples are referred to by the designators 10A and 10B, respectively.

Table 2. Preliminary Evaluation of Si Implanted  
GaAs, Laser Annealed in Air

ENERGY	SURFACE	BREAKDOWN	ISOLATION	C-V PLOT DATA
2 j/cm <sup>2</sup>	extensive orange peel, surface loss	3V @ 20 $\mu$ a	excellent	data unreliable
1.45 j/cm <sup>2</sup>	extensive orange peel	$\sim$ 6V @ 20 $\mu$ a variable	excellent	data unreliable
.4 j/cm <sup>2</sup>	some orange peel, no apparent material loss.	$\sim$ 6V @ 20 $\mu$ a	excellent	data unreliable

Table 2 summarizes our preliminary evaluation of samples 10A. The C-V data indicated poor Schottky barriers at the probe contacts. The reason for this is not known at this time.

Evaluation of wafer 10B is not yet complete, but the following statements can be made:

- 1) The high energy pulses ( $2-3 \text{ j/cm}^2$ ) evaporate material from the surface.
- 2) The low energy pulses ( $E < .5 \text{ j/cm}^2$ ) cause no surface damage.
- 3) All energies tested gave some activation of the implanted species, but energies less than about  $.2 \text{ j/cm}^2$  are clearly less effective than the higher energies.
- 4) The isolation between implanted areas was excellent in all cases.

### 3.3 Ion Implanted Silicon

Several implanted, amorphous silicon structures were studied. In each case, laser induced regrowth and activation proved superior to standard thermal processing.

Arsenic Implanted Silicon: Silicon wafers were implanted with arsenic ion fluences of  $2 \times 10^{15}$ ,  $6 \times 10^{15}$ , and  $1 \times 10^{16}$  arsenic atoms per  $\text{cm}^2$  at 50 keV implant energies. The calculated arsenic concentrations within the crystal are  $1.1 \times 10^{21}$ ,  $3.5 \times 10^{21}$  and  $5.5 \times 10^{21}$  per  $\text{cm}^3$ , respectively.<sup>+</sup> These high fluences, of interest to emitter technology, cause the silicon surface to become amorphous.

One set of implanted samples was subjected to standard oven annealing procedures and another set to laser induce thermal treatment. Sheet resistance measurements were made on all samples. The results are shown in Table 3. In all cases, the resistance of the laser treated samples is lower than that of the oven treated samples. This improvement is especially notable for the highest implant fluence.

Some of these data are plotted in Figure 5 as  $1/R$  versus implant dosage. This format is especially instructive because  $1/R$  is proportional to conductivity, which is given by  $\sigma = n\mu$ , where  $n$  and  $\mu$  are the number density and mobility, respectively, of the free carriers. Also shown is the ideal conductivity curve based on the assumption of proportionality between the number of free carriers and the arsenic fluence (assuming constant mobility). The failure of the data to follow the ideal curve can be due to either a sub-linear dependence of  $n$  on dosage or decreasing mobility with increasing dosage. Both effects are expected because the equilibrium solubility limit of arsenic in silicon is exceeded for fluences in excess of  $3 \times 10^{15} \text{ cm}^{-2}$ , hence limiting  $n$ , and because impurity scattering by undissolved arsenic tends to decrease  $\mu$ .

---

<sup>†</sup> These are the densities at the maximum of the expected gaussian distribution. We note that the solid solubility of As in Si under equilibrium conditions is  $1.8 \times 10^{21} \text{ cm}^{-3}$ . The higher dosages exceed this limit significantly.

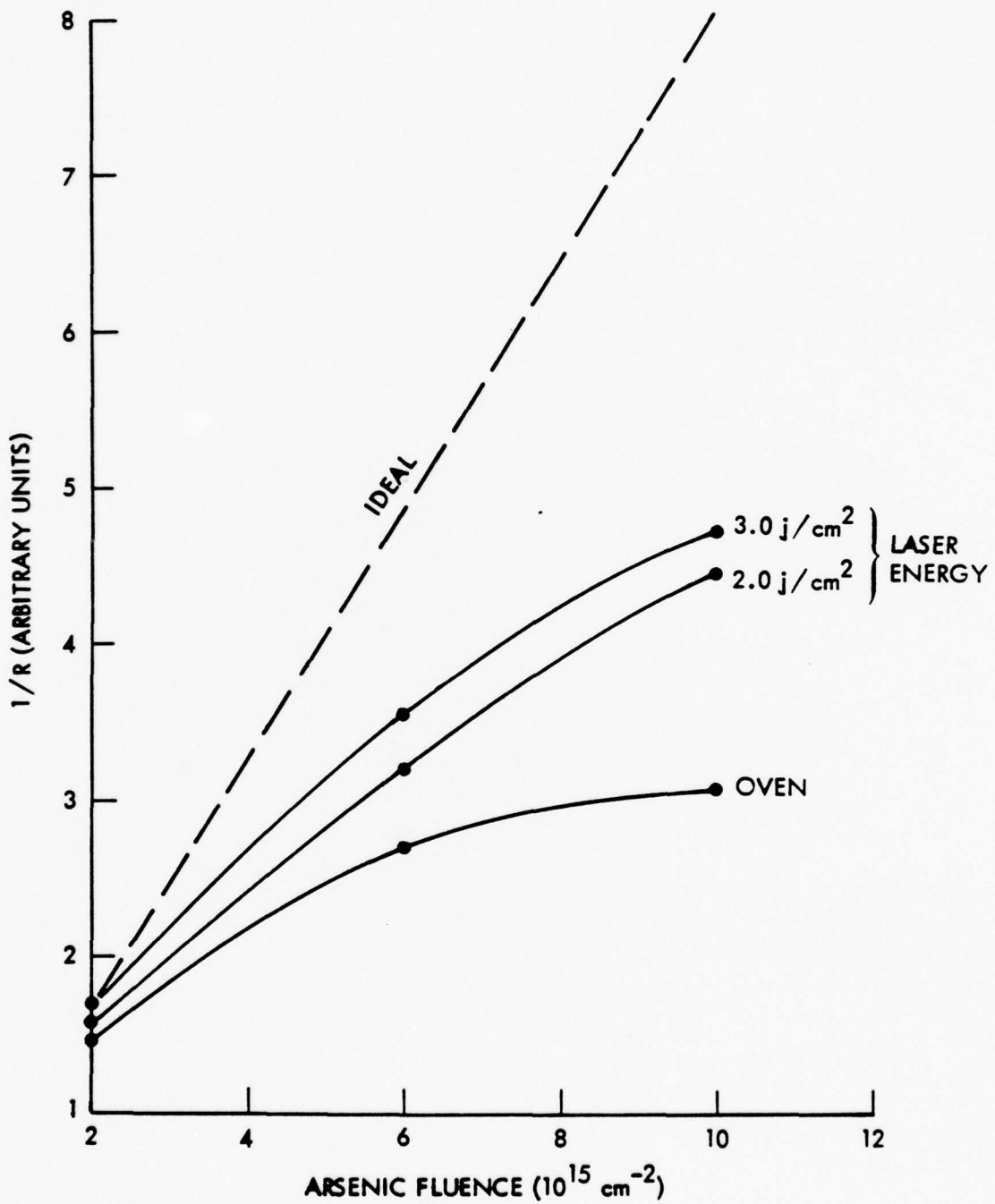


Figure 5. Reciprocal of Sheet Resistance versus Arsenic Implant Fluences as a Function of Thermal Treatment

Oven annealing the laser processed samples caused the conductivity to drop to approximately the thermal-anneal-only values, as shown in Table 4. We infer from this result that laser processing obtains solid solution concentrations in excess of equilibrium limits. Similar results on B, P, Sb and As in silicon have been reported by C.W. White, et al.<sup>16</sup>

The data in the last column of Table 3 show that less laser energy is required to obtain large percentage decreases in resistance as the arsenic concentration is increased. This trend is consistent with the observation that the density of non-radiative recombination sites increases with increasing arsenic fluences, thereby increasing the conversion efficiency of laser energy into heat in the localized damaged region.

Laser Annealed Silicon Diodes: Planar n/p diode structures were fabricated from arsenic implanted and phosphor implanted, p-type ( $5 \Omega\text{-cm}$ ) silicon. Implant fluences in both cases were  $5 \times 10^{15} \text{ cm}^{-2}$ . Each of the amorphous silicon surfaces was irradiated by a single laser pulse, with pulse energies ranging from 0.5 to  $3.0 \text{ J/cm}^2$ . After irradiation, contacts were evaporated onto the structures and their reverse leakage currents measured and compared to measurements on diodes made by standard thermal processing techniques with the same implanted material. The results are shown in Figure 6. These data show again the superiority of laser processing over oven processing. They also show that there exists an optimal laser anneal energy density, below which annealing is incomplete and above which the laser radiation apparently causes damage to the material. The resistance data shown in Table 3 do not indicate an optimum. These data are not in conflict, however, since diode performance is governed not only by the resistance of the constituent layers but also by the quality of the junction between the layers.

Table 3. Sheet Resistance Data of Arsenic Implanted Silicon  
Following Oven Anneal and Laser Anneal

SAMPLE	ARSENIC FLUENCE ( $\text{cm}^{-2}$ )	TYPE OF ANNEAL	SHEET RESISTANCE R, ( $\Omega/\text{squared}$ )	$100 \left[ \frac{R_{\text{oven}} - R_{\text{laser}}}{R_{\text{oven}}} \right]$
ES-1B		OVEN	68.16	---
ES-1A	$2 \times 10^{15}$	LASER ( $\text{j/cm}^2$ )	67.65	0.7
		1.5	62.11	8.9
		2.0	58.95	13.5
		2.4	58.17	14.7
		3.0		
ES-2B		OVEN	36.79	---
ES-2A	$6 \times 10^{15}$	LASER ( $\text{j/cm}^2$ )	34.61	5.9
		1.5	31.27	15.0
		2.0	30.53	17.0
		2.4	28.28	23.1
		3.0		
ES-3B		OVEN	32.88	---
ES-3A	$10 \times 10^{15}$	LASER ( $\text{j/cm}^2$ )	21.45	34.8
		1.5	22.51	31.5
		2.0	21.01	36.1
		2.4	21.15	35.7
		3.0		

Table 4. Sheet Resistivities After Laser Anneal (LA) and  
Laser Anneal Followed by Thermal Anneal (TA) at 900°C.

Arsenic Fluence at 50 keV (ions/cm <sup>2</sup> )	Laser Energy J/cm <sup>2</sup>	Laser Anneal Only	Laser Anneal +15 min Thermal Anneal	R(Ω/squared) Laser Anneal +30 min Thermal Anneal
2 × 10 <sup>15</sup>	0	---	84.2	79.9
	1.5	67.7	72.7	75.8
	2.0	62.1	69.8	65.4
	2.4	59.0	63.5	60.4
	"	58.2	61.1	62.6
	0	---	71.7	63.5
6 × 10 <sup>15</sup>	1.5	34.6	50.6	47.0
	2.0	31.3	41.9	---
	2.4	30.5	39.6	---
	"	28.3	40.8	---
	3.0	---	63.0	58.0
	0	---	52.9	54.3
1 × 10 <sup>16</sup>	1.5	21.5	42.7	37.5
	2.0	22.5	35.4	33.6
	2.4	21.0	33.4	33.5
	"	21.2		

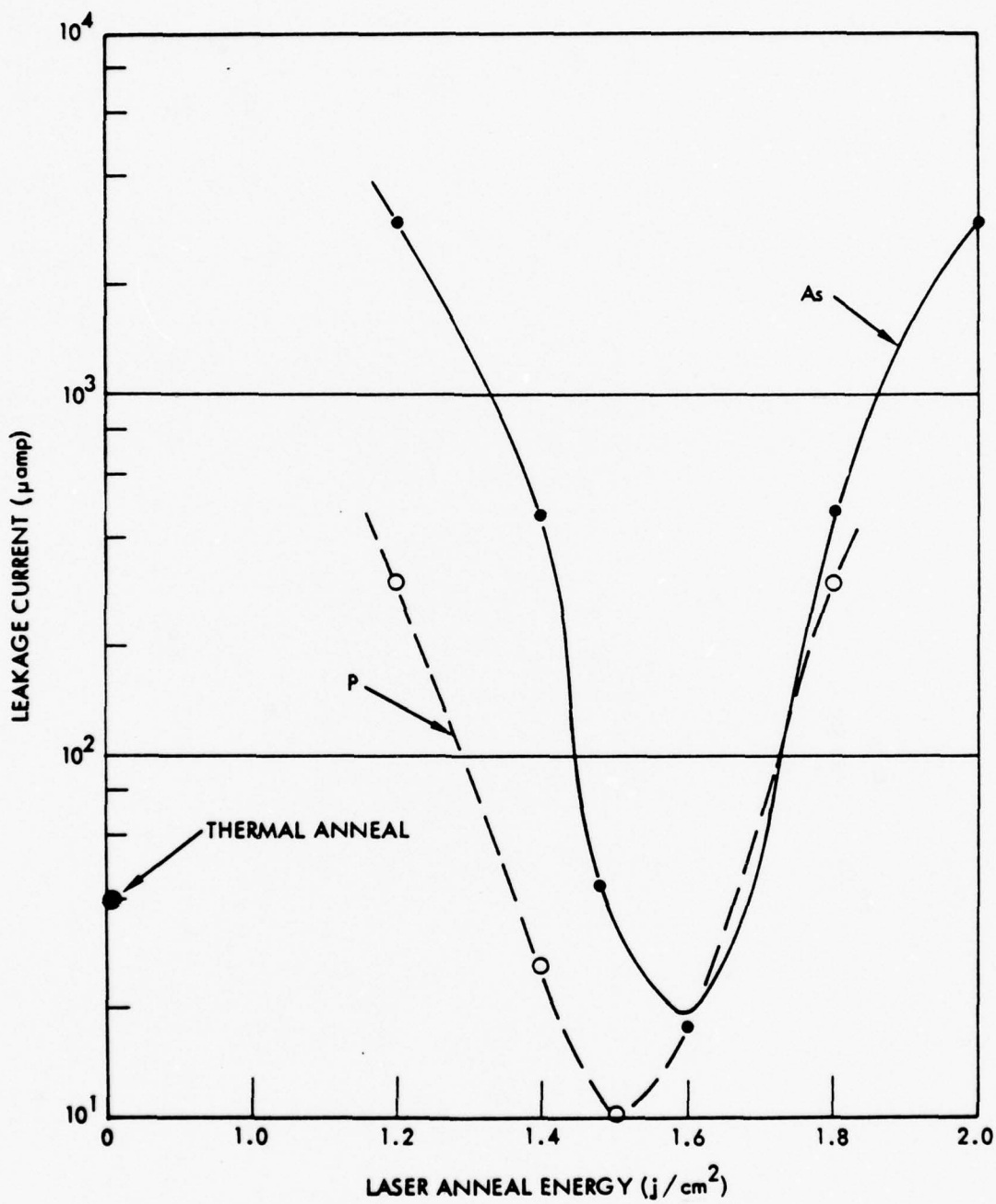


Figure 6. Reverse Leakage Current Measured at  $V = -15$  Volts for Laser Annealed and Thermal Annealed P and As Implanted Silicon Planar Diodes.

### 3.4 Silicon on Sapphire Experiments<sup>+</sup>

Experimental studies of laser processing of silicon on sapphire were initiated. The laser blow-off concept was employed in these preliminary experiments to obtain the silicon on sapphire deposit. Figure 7 shows a schematic of the experimental arrangement used for this process (Step 1), and for the subsequent step (Step 2) of laser processing of the silicon film obtained in Step 1.

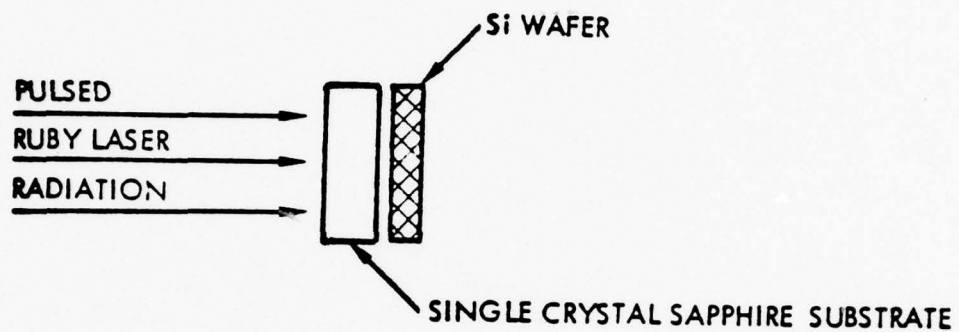
Totally unanticipated results were obtained through the application of Step 1 at high laser blow-off intensities. The thin silicon films possess extensive long range order as evidenced in Figures 8b and 8c. Similar order was not observed in films deposited by lower blow-off intensities, or at any intensity when glass substrates were substituted for the crystalline sapphire. Thus the order shown in Figure 8 is definitely relatable to the high blow-off intensities and to the presence of the crystalline substrate. The mechanism responsible for this high degree of order is not known at this time.

Application of Step 2 to the silicon films of Figures 8b, and 8c at laser intensities of  $10 \text{ j/cm}^2$  resulted in a decrease in the order of the layers. The domains shown in Figure 8c lost their regular shape, appeared crumbled and were no longer closely packed.

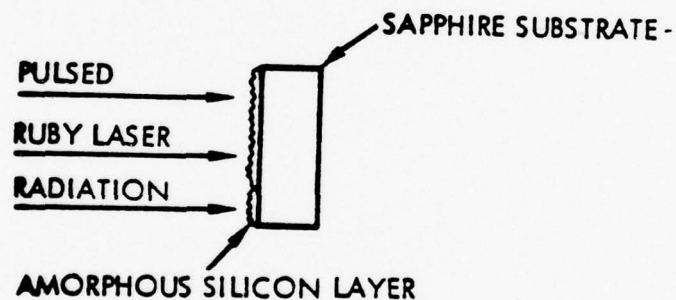
We also irradiated single crystal GaAs through a glass slide placed in contact with the GaAs. Figures 9a and 9b are photographs of the irradiated GaAs surface and the blow-off deposition on the glass. Both surfaces show a regular periodic structure. Similar surface periodicity has been observed by others.<sup>7,25,26</sup>

---

<sup>+</sup> This work was performed on IR&D funds. We include a discussion of it here because of its potential relevance to laser processing of semiconductor devices.



STEP 1: BLOW-OFF



STEP 2: LASER PROCESSING

Figure 7. Schematic of Experimental Set-up for Laser Blow-off and for Laser Treatment of Thin Silicon Layers Obtained in the Blow-off Step.

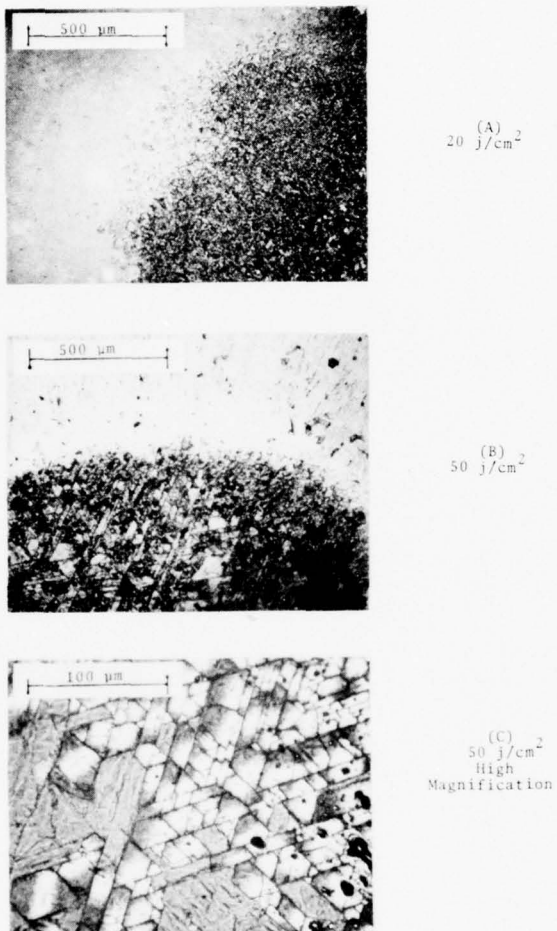
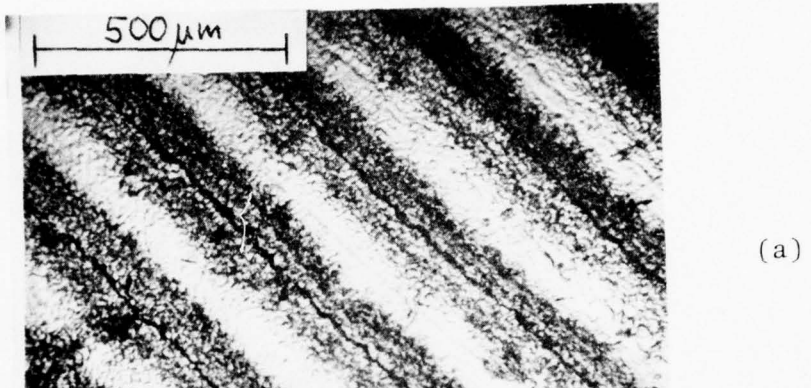
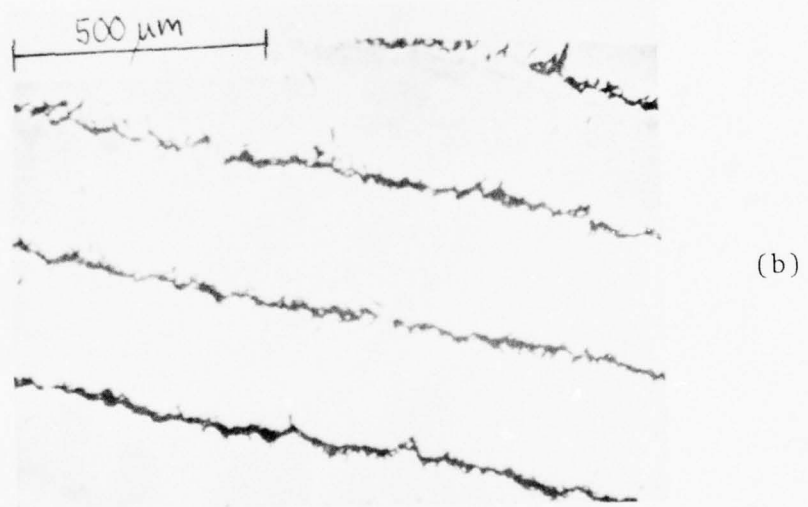


Figure 8. Silicon Deposit on Sapphire with  $20 \text{ J}/\text{cm}^2$  (top) and  $50 \text{ J}/\text{cm}^2$  (center and bottom) Laser Energy. The  $20 \text{ J}/\text{cm}^2$  deposit has nearly no long range order, while the  $50 \text{ J}/\text{cm}^2$  has well developed long range order.



(a)



(b)

Figure 9. Photographs of (a) GaAs Surface After Laser Blow-off and (b) GaAs Deposition on Glass as in Step 1 of Figure 7 with the Glass Substrate Replacing the Sapphire.

Maracus, et al<sup>25</sup> ascribe the phenomenon to a nonlinear interaction between simultaneously oscillating axial modes of the laser. Others<sup>26</sup> relate it to an interference effect between the primary laser beam and an optical wave scattered from a surface disturbance. Whatever the cause, the presence of these irregularities are undesirable from a device point of view.

The material deposited on the glass appears to mirror the structure of the silicon substrate. Photographs at a higher magnification such as Figure 10 show that the dark lines of Figure 9b represent highly irregular deposits of material.

### 3.5 Laser Induced Impurity Diffusion

We have considered the use of laser heating to activate solid state diffusion of dopants in semiconductors; this method is potentially superior to bulk heating because of its ability to yield much sharper impurity profiles. In Appendix B we present a detailed analysis comparing concentration distributions induced by the two techniques. Here we simply indicate by nondetailed physical reasoning why sharper profiles are to be expected from laser heating.

In dopant diffusion the particle flux  $\vec{j}$  is proportional to the negative gradient of the concentration C,

$$\vec{j} = - D(T) \nabla C . \quad (8)$$

The proportionality constant D(T) is the particle diffusivity, which is very strongly dependent on temperature T. To illustrate the strength of this dependence we note that for a dopant having an activation energy of 1 ev the ratio of D at  $1000^{\circ}\text{K}$  to D at  $300^{\circ}\text{K}$  is  $D(1000^{\circ}\text{K})/D(300^{\circ}\text{K}) = 10^{12}$ . Therefore, at temperatures in the vicinity of  $1000^{\circ}\text{K}$  the flow rate is enormously greater than at room temperature even for smaller concentration gradients.

In bulk heating the sample temperature is uniform, so D(T)

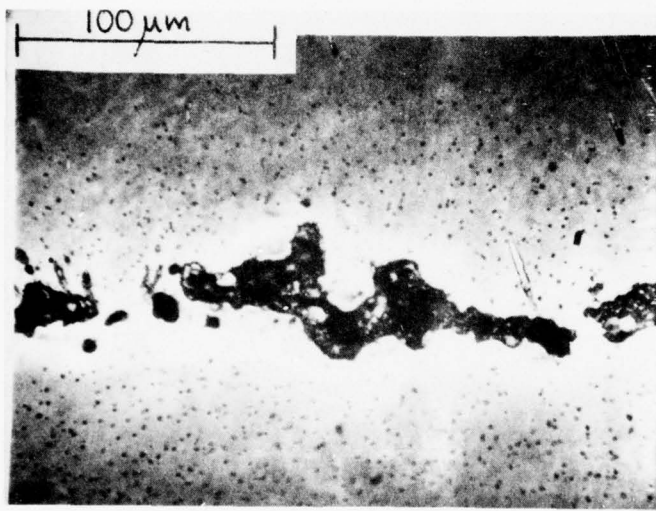


Figure 10. High Magnification Photograph of GaAs on Glass.  
Scene is enlarged view of a section of a dark  
line of Figure 9b.

is constant throughout the sample and the diffusion rate at any point depends exclusively on the concentration gradient. By contrast, in laser processing the diffusivity is extremely large in the localized heated region and extremely small elsewhere. Therefore, the impurities diffuse essentially only within the region of large  $D(T)$  and not outside; the result is then a sharp concentration cut-off at the edge of the heated region.

The dopant concentration  $C$  must satisfy the continuity equation,

$$\frac{\partial C}{\partial t} + \nabla \cdot \vec{j} = S , \quad (9)$$

where  $S$  is the source term in particles per unit volume per unit time. Insertion of Equation (8) for the particle flux into (9), and reduction of the result to one dimension, lead to the diffusion equation,

$$\frac{\partial C}{\partial t} - \frac{\partial}{\partial x} (D \frac{\partial C}{\partial x}) = S , \quad (10)$$

whose numerical solution is treated in Appendix B. The detailed results presented there confirm quantitatively the above contention that laser heating can produce much more sharply defined dopant profiles than can bulk heating.

Significant diffusion requires in excess of  $10^4$  laser pulses. This number is, for all practical purposes, beyond the capabilities of existing high power pulsed lasers. For this reason we have not performed experiments on laser induced solid phase diffusion.

Development of high power, high repetition rate visible gas lasers is being pursued in a number of laboratories. The most promising candidate for laser induced diffusion is the excimer laser. When average powers of the order of  $10^3$  watts are available, further investigation of this application should be pursued.

### 3.6 Summary

- Laser annealing of ion implanted GaAs and Si was demonstrated to be superior to oven anneal in a number of experiments.
- Laser annealing obtains solid solutions of impurities in excess of equilibrium values.
- Laser induced solid phase diffusion produces steep impurity distribution boundaries. Application is limited at present time due to lack of availability of high average power ( $10^3$  watts) visible lasers.

## Task 2

### EVALUATION OF THE LASER BLOW-OFF ION IMPLANTATION SOURCE

#### 1.0 INTRODUCTION

Ion implantation of dopants in semiconductor materials has become a standard practice in the manufacture of solid state electronic devices. Ion implantation is a non-equilibrium process that permits a degree of control over the spatial distribution of dopant atoms in the host crystal that cannot be achieved through thermal diffusion. Dopant species with low diffusion rates even at elevated temperatures can often be handled with relative ease through ion implantation. However, a deleterious side effect of ion implantation is damage to the host crystal caused by the high energy ions necessary to penetrate to the desired depths. High temperature annealing is commonly used to repair implant-induced damage. In some cases the annealing process itself causes a degradation of the implanted material. For example, high temperature annealing of implanted GaAs results in migration of As atoms from the crystal. In large scale integrated circuits, heat treating may alter the properties of the intrinsic material at locations remote from ion implanted sites. The following part of this report describes progress towards developing a new ion implantation technique which shows promise of providing a self-annealing feature as well as being relatively simple, fast, with large areal coverage and amenable to a very wide range of dopant species.

This new ion implantation technique utilizes pulsed laser irradiation of a solid surface of pure dopant material to produce a high temperature plasma of dopant ions. The plasma expands into vacuum, reducing the charge density to the point where an externally applied electric field can be used to extract ions from the plasma. In principle these ions can be accelerated to an arbitrarily high energy and can be used to implant semiconductor

materials. A subtle aspect of this method is the pulsed nature of the ion beam current. For reasonable values of ion energy and ion areal density, it appears that annealing temperatures can be reached in the implanted regions for very short times at each laser pulse. Thus the possibility presents itself that the use of high intensity short duration ion beam pulses for ion implantation may be accompanied by self-annealing of the implant damage. One of the main objectives of this program is to carefully examine this possibility experimentally by systematically evaluating the characteristics of semiconductor devices implanted with this laser blow-off technique over a variety of practical conditions. This report describes the progress to this time.

## 2.0 EXPERIMENTAL APPARATUS

A schematic diagram and picture of the ion implantation system used in these tests is shown as Figures 1a and 1b. This system is an adaptation of the high intensity metal ion beam source described in Reference 27. The ions to be implanted are created by pulsed laser irradiation of a solid block of the implant material. In the present case a Nd:YAG laser is Q-switched with a Pockels cell, producing a 1 joule laser pulse with less than 0.1 microsecond length at a wavelength of 1.06 micron. The laser beam passes through steering prisms and vacuum system windows and is focused to a 2 mm diameter spot on the implant material by a 60 cm focal length lens. Tests thus far have utilized a solid boron target. This laser target is located in an electric field-free region, with the normal to its surface directed approximately toward the silicon wafer to be implanted. The laser beam strikes the surface from an angle of about 25° to the normal. The position and angle of the boron target are adjustable to optimize the intensity and uniformity of the ion beam in the direction of the silicon wafer, since these parameters are complicated functions of the laser beam energy and angle.<sup>27,28</sup>

The result of the rapid deposition of laser energy on the implant material surface is to produce a high temperature plasma "bubble" of implant material ions and electrons, which "blow-off" from the surface. In the present configuration this plasma bubble expands freely until it reaches the ion acceleration region. This distance is presently 37 cm. In the first measurements no acceleration was utilized, and the silicon wafers and an array of current measuring Faraday cups were placed at this position. This set-up allowed the measurement of implant ion fluence and areal uniformity. This configuration may prove to be valuable in its own right as a method for depositing a thin layer of certain materials for subsequent laser diffusion processing, since atoms of essentially any solid dopant can be deposited under

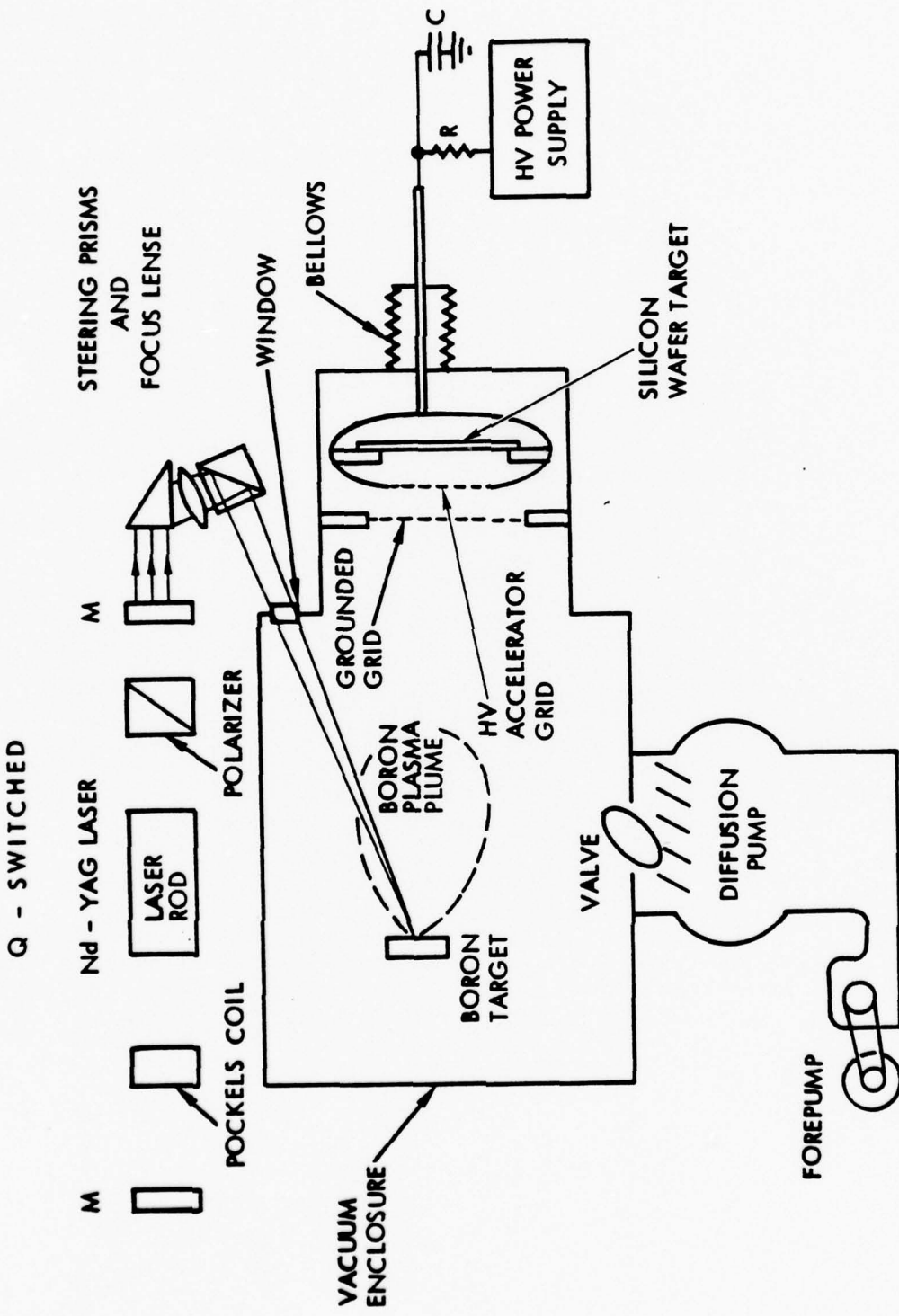


Figure 1a. Schematic Diagram of Laser Blow-Off Ion Implantation System

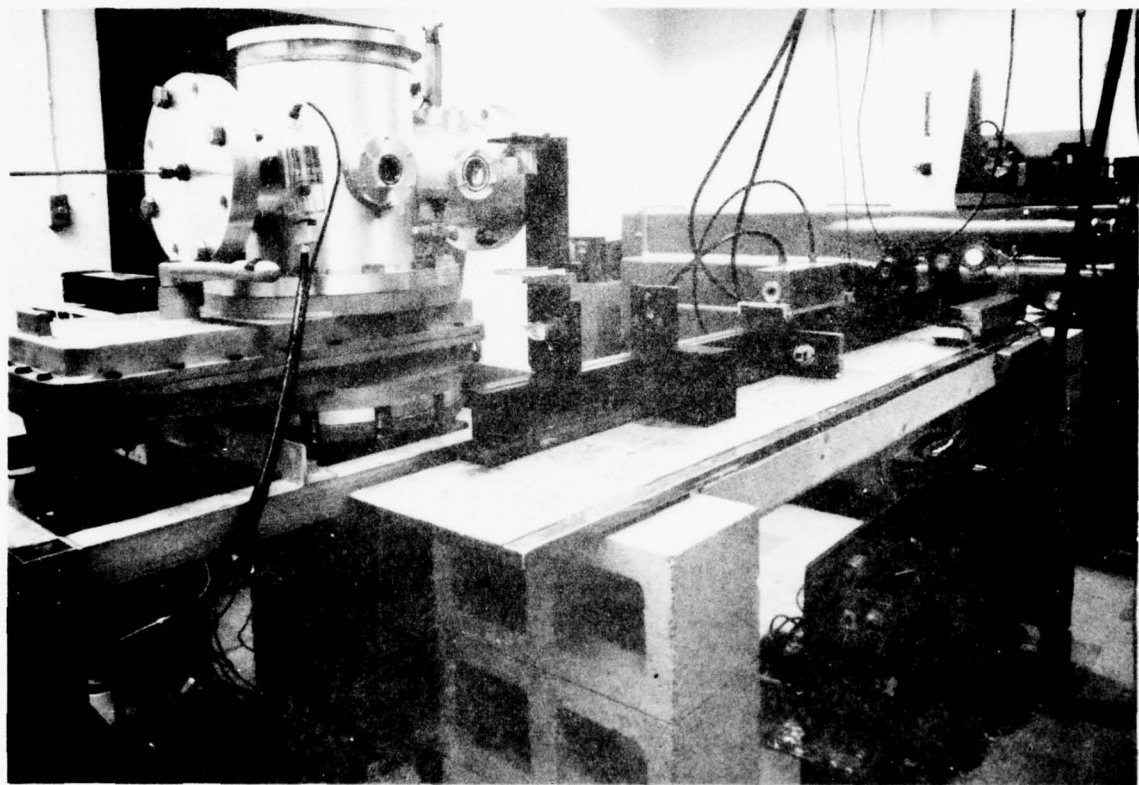


Figure 1b. Photograph of Laser Blow-Off  
Ion Implantation System

vacuum conditions. The ion energies are a few hundred electron volts in this case, and thus barely penetrate the surface.

In the case where high energy implantation is to be used, acceleration of the implant ions is necessary as they reach the acceleration region. In the present configuration, this acceleration occurs between the grids shown. The first grid is held at the same potential as the field-free plasma expansion region. The second is held at a high negative voltage equal to the ion kinetic energy in eV desired. The silicon wafer is held at the same potential as the second grid at a distance approximately one centimeter beyond. This "drift" distance is intended to wash out any non-uniformity in implant caused by grid shadows or focusing effects. The drift distance cannot be too long because space charge spreading becomes severe because the plasma electrons are rejected by the ion acceleration region. The grids are presently 100 mesh stainless steel.

For initial tests, two types of silicon wafers have been obtained from Monsanto. Both types are 3 inches in diameter and 0.015 inches thick, are oriented 100, and have resistivities of 10 ohm-centimeters. One type is N doped with phosphorus and the other type is P doped with boron. In order to economize on wafer material, the wafers are cut into cm-size chips for use when the measurements permit.

The accelerating voltage is supplied by a Plastic Capacitors Inc., 50 kV power supply, which charges an 0.05 microfarad capacitor across the accelerating grids. In the event of arc breakdown, the grids would have to dissipate 60 joules of energy. If an accelerating region area of  $100 \text{ cm}^2$  and an implant ion density of 1 microcoulomb/cm<sup>2</sup>/pulse is considered, the accelerating voltage drops from 50 kV to 48 kV during the pulse. A larger capacitance value would reduce the voltage change, but the present value is safer during development.

The vacuum system consists of fairly standard components

including a 10 inch oil diffusion pump with water-cooled baffle and mechanical forepump. This system should be adequate for developmental purposes, but final definitive quantitative device tests may necessitate an ultra-high vacuum system to minimize surface contamination.

### 3.0 RESULTS

Measurements have been made and results obtained largely in the order of laser performance, implant plasma production, plasma plume characteristics, ion current and areal uniformity, implant material deposition without acceleration, and implant with high energy implant ions.

The Nd:YAG laser is operating at an output energy up to 1 joule per Q-switched pulse. This is lower than anticipated and appears to involve a problem with the polarizer and Pockels cell. The output energy also varies more from shot to shot than had been expected, about  $\pm$  5 to 10 percent. This leads to a roughly similar variation in implant ion fluence from shot to shot. Although the laser energy and stability are less than might be desired, they should be sufficient to carry out the present tasks. So long as each ion pulse is monitored, and a number of shots are used per implant dose, it should be possible to control the total implant dose within the necessary limits. It was therefore decided to accept the laser performance as is for now, and move ahead with other aspects. It is certain that better laser performance is possible, and that eventually when high pulse repetition rates are needed a different laser will be necessary in any event.

A piece of pure, solid boron of dimension of order 1 cm was obtained for the laser blow-off target, that is, the source of implant ions. The actual purity is thought to be high, but this will be checked mass spectrometrically during analysis of the blow-off deposited material, as described below. Even with many laser shots, very little cratering of the boron occurred. This is consistent with earlier work, which indicated that less than one micron of material is removed per shot. No apparent difficulty was encountered in the implant ion plasma production.

In order to examine the characteristics of the expanding

plasma plume with regard to ion energy, current and number density, and angular distribution, an array of 5 Faraday cups was placed symmetrically along an arc perpendicular to the normal to the boron laser target in a plane containing the normal. The cups were 41 cm from the target and were spaced  $4.2^\circ$  apart with respect to the target, that is, the 5 cups observed the target at angles of  $8.4^\circ$ ,  $4.2^\circ$  and  $0^\circ$  each side of the normal. The distance between centers of the outer cups was 12 cm. The Faraday cups detected ions within the expanding plasma plume as the ions reached the cup collectors. These cups were designed and tested for high current operation at the plasma densities encountered. The effective detection area was  $1 \text{ cm}^2$ . These cups were of planar construction so that the ion transit time within the cup was negligibly small compared to the transit time from the laser target to the cup. Elements within the cup were electrically biased to suppress secondary electron emission. The Faraday cups could be operated in either the current sensing mode or the total charge collection mode, with the signals displayed directly on an oscilloscope in either case. The present results with boron ions are consistent with earlier theoretical and experimental work<sup>2</sup> done in this laboratory on laser blow-off plumes. This work involved a model based on the following physical assumptions.

It was assumed that the deposited laser energy vaporizes and ionizes  $N_0$  particles from a small region of the source material surface. This hot plasma "bubble" of  $N_0$  ions begins to expand against the substrate and imparts momentum to it, thereby giving the center of mass of the  $N_0$  ions a velocity  $v_{cm}$  in the laboratory coordinate frame. Because of symmetry,  $v_{cm}$  is normal to the surface. After the center of mass of the  $N_0$  ions has moved a distance from the surface, the number density of ions remains high enough so that most of the  $N_0$  ions equilibrate at a temperature  $T$  relative to their center of mass, which continues

to move at  $v_{cm}$ . That is, an observer moving with the center of mass would observe an essentially spherically symmetric plasma "bubble" in equilibrium at T, and freely expanding. As the number density continues to decrease, the ion velocity distribution corresponding to equilibrium at temperature T becomes "frozen" in the center-of-mass system. A laboratory observer at a larger distance from the source laser spot observes ions arriving with velocity essentially along a line from source spot to observer, but with a plume-like angular distribution due to the center-of-mass velocity  $v_{cm}$  superimposed on the purely thermal velocity distribution.

The theory thus consists simply of calculating the number density  $\rho$  and current density  $\vec{j}$  of ions to be observed in the laboratory frame resulting from  $N_0$  ions expanding with spherical symmetry and having equilibrium velocity distribution corresponding to T in their center-of-mass system, and with a superimposed center-of-mass velocity  $v_{cm}$ .

Figure 2 shows the coordinate system for the theoretical model. The present adaptation differs in that a solid target is struck by the laser beam on the front surface. The current density of ions  $\vec{j}$  in ions per unit area per unit time is given by

$$\vec{j}(r, \theta, \lambda, \eta) = \left(\frac{512}{9}\right) \left(\frac{2}{\pi}\right)^{3/2} \left(\frac{kT}{m}\right)^{1/2} \frac{N_0}{r^3} \exp\left(-\frac{3\lambda^2}{2}\right) \cdot (\phi\eta)^{-4} \\ \times \exp\left\{\left[-\frac{32}{3}(\phi\eta)^{-2}\right] \left[1 - 3(\lambda \cos \theta)(\phi\eta)/4\right]\right\} \hat{r}$$

where

$$\phi = \left\{ \sqrt{(\lambda \cos \theta)^2 + \frac{16}{3}} - (\lambda \cos \theta) \right\} ,$$

$$t_{max} = \frac{3}{8} \phi \sqrt{m/3kT} r ,$$

$$\eta = t/t_{max} ,$$

and

$$\lambda v_{RMS} = v_{cm} = \lambda \sqrt{3kT/m}$$

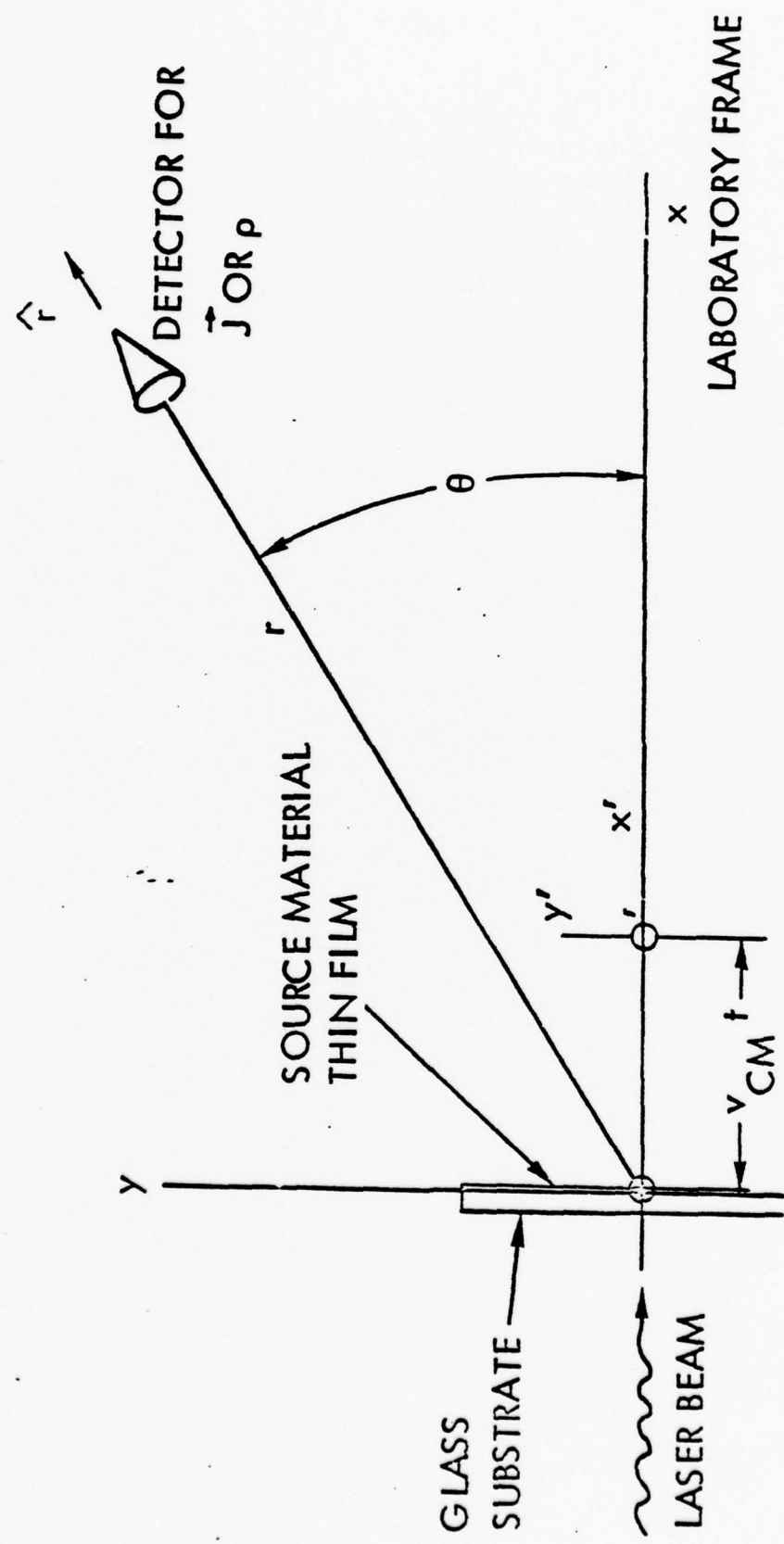


Figure 2. Geometric Arrangement for the Theoretical Model and Experiment

gives the relation defining the "blow-off" parameter  $\lambda$ . Small  $\lambda$  implies small  $v_{cm}$  and hence a broad angular distribution, while large  $\lambda$  implies a narrow "plume". The other parameters above include time  $t$ , ion mass  $m$ , Boltzmann's constant  $k$ , temperature  $T$ , and time of  $J_{max}$ ,  $t_{max}$ . Figure 3 shows these results graphically in terms of  $J/J_{max}$  versus  $\eta$ , and therefore represents an expected picture of  $\dot{J}$  versus  $t$  on an oscilloscope trace of a current sensing Faraday cup. Picture A of Figure 4 shows an actual trace of a boron ion pulse from the present measurement. The points on Figure 3 are the same data plotted there. The skewness away from the theoretical curves has been noted before<sup>28</sup> for ions, while the agreement is quite good for neutral atom blow-off.<sup>28</sup> The  $\lambda$  values depends on laser energy density and the target materials, and are thus subject to some control. The general agreement with theory is sufficiently good to predict currents and densities as functions of time, distance and angles. Of particular importance is the sensitivity of the angular distribution to  $\lambda$ , as seen next. The total number of ions passing across unit area normal to  $\hat{r}$  per pulse is given by

$$\int_0^\infty \dot{J} dt = \frac{N_0}{4\pi r^2} \sqrt{\frac{2}{\pi}} \exp(-3\lambda^2/2)$$

$$x = \sqrt{3/2} (\lambda \cos \theta) + \sqrt{\pi}(1/2 + x^2)(1 + \operatorname{erf} x) e^{x^2} \hat{r}$$

where  $x = \sqrt{3/2} (\lambda \cos \theta)$

and  $\operatorname{erf} x = \frac{2}{\sqrt{\pi}} \int_0^x \exp(-u^2) du$ .

Figure 5 shows these theoretical angular distributions as functions of  $\lambda$ . Also included are previous experimental points obtained for aluminum ions and present points obtained for boron ions.

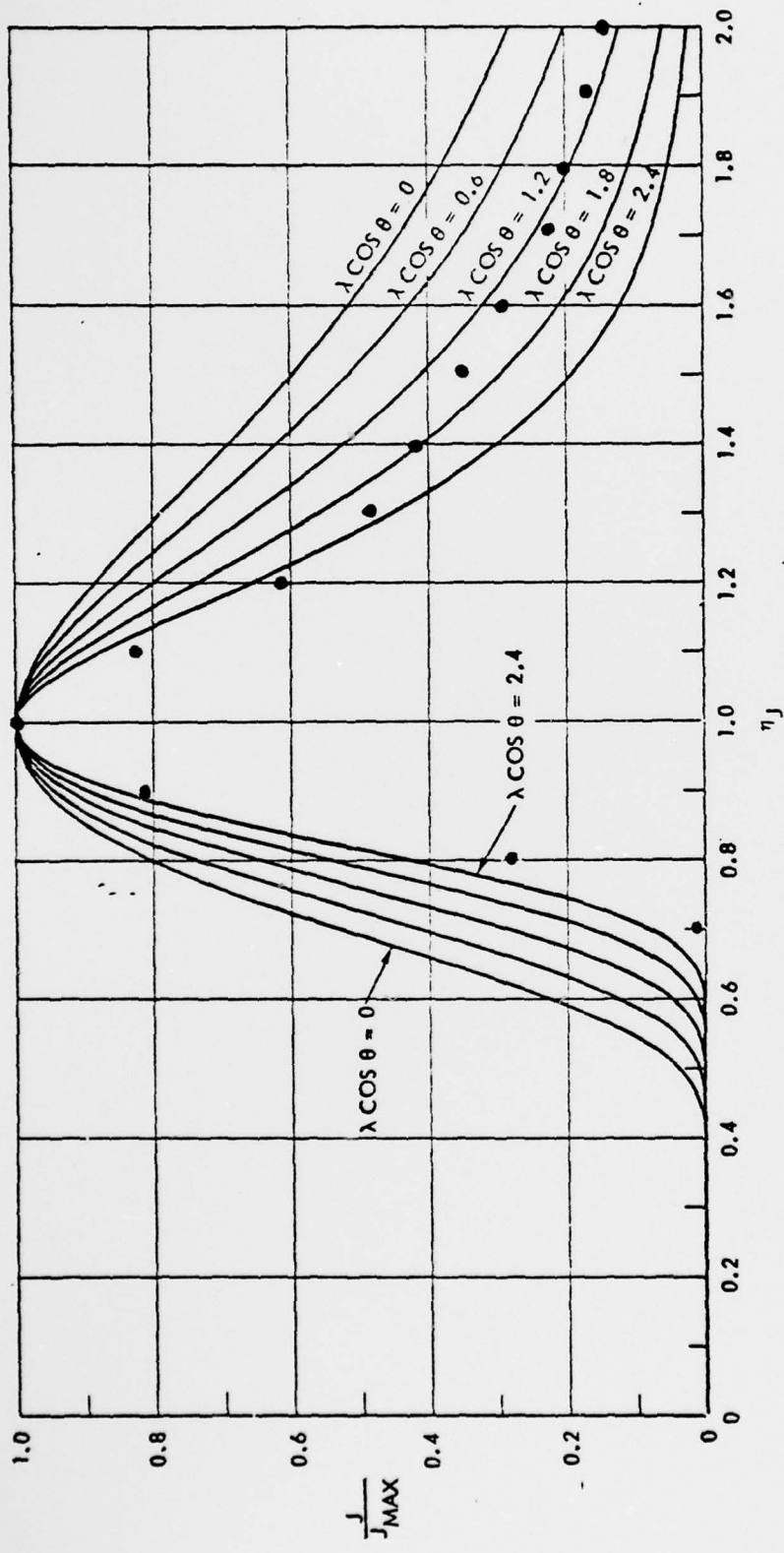
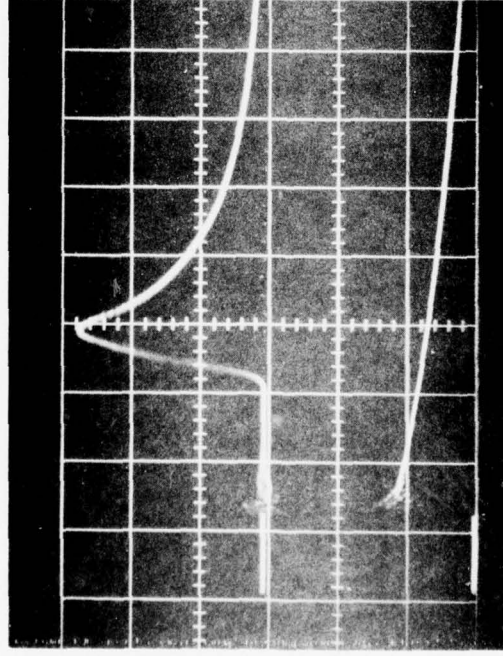
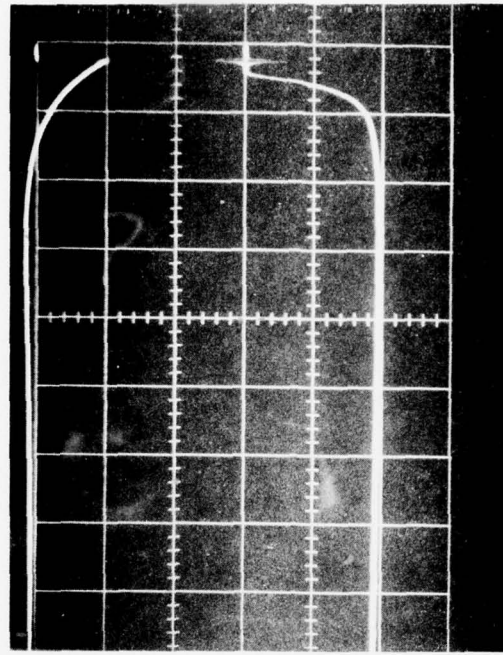


Figure 3. Theoretical Curves for Beam Particle Current Density  $\frac{J}{J_{MAX}}$  versus Time, Normalized to the Time at Which  $\frac{J}{J_{MAX}}$  is a Maximum. Points are measured values for boron ions. Boron ion current vs time.



(a)



(b)

Upper: Boron Ion Current vs Time  
Lower: Laser Energy and Timing Marker

Upper: Boron Ion Collected Charge vs Time  
Lower: Laser Energy and Timing Marker

Figure 4. Unaccelerated Boron Ion Pulses

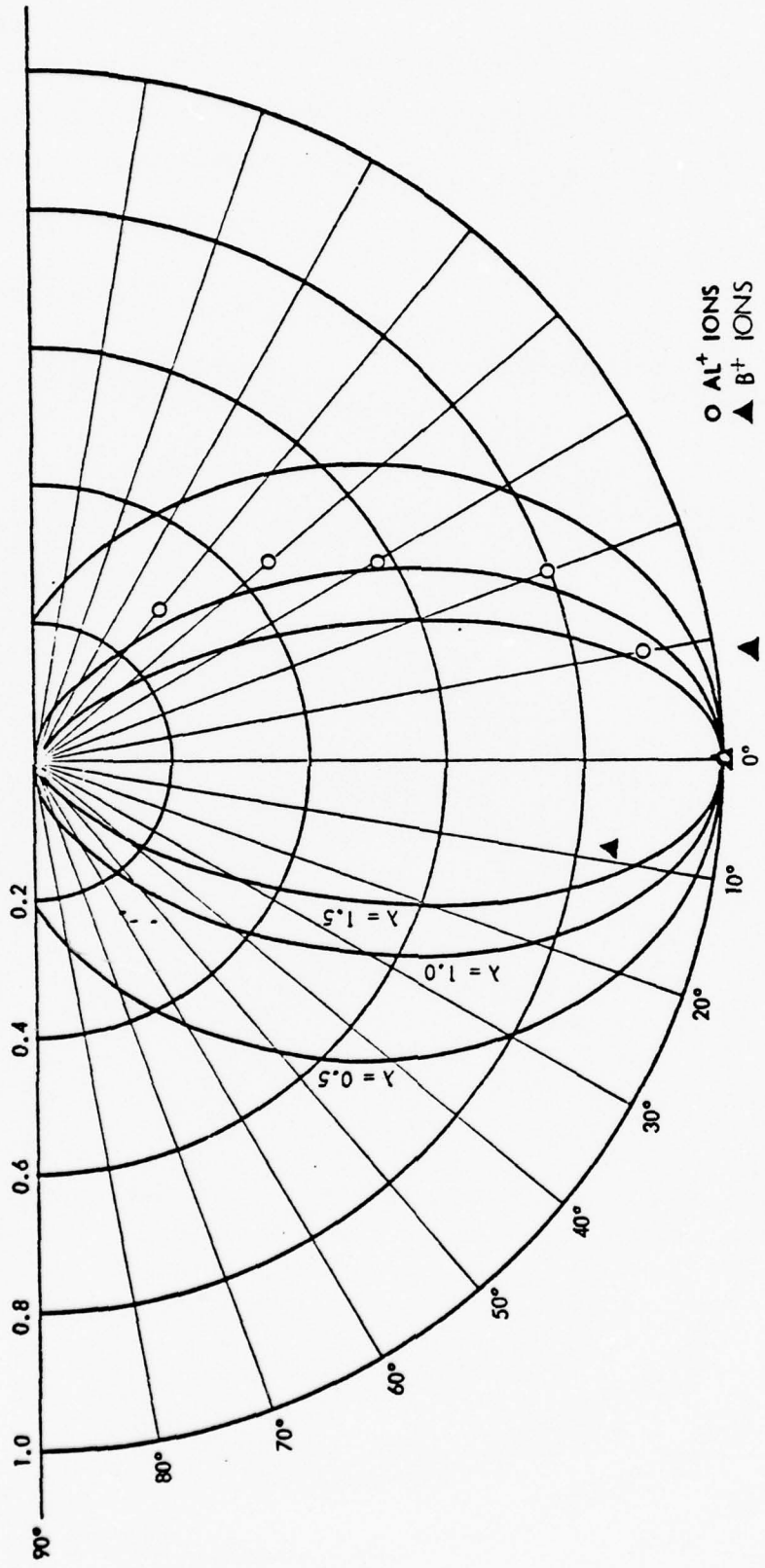


Figure 5. Theoretical Curves for  $\int_0^\infty j dt$  versus Detector Angle  $\theta$  at Constant Distance  $r$  and Normalized to the Value for  $\theta = 0$ . Points are measured values for aluminum and boron ions.

It is obvious that small values of  $\lambda$  are necessary if one is to implant large areas with high uniformity without "rastering" the wafer between shots. The ion arrival time profiles may also be very important in self-annealing aspects, since the thermal pulse will reflect the arrival time pulse. Figures 4 and 5 from Reference 27 show examples of widely differing angular distributions depending on laser beam conditions. The presently obtained angular distributions are adequate for present purposes and will be optimized further, but it is clear that variations in ion fluence as a function of angle put eventual limits on the size of wafers which can be implanted with high uniformity over the surface.

Measurements have been made to determine the actual ion current and areal implant ion density by combining Faraday cup array current measurements with implant ion deposition without acceleration. The currents and charge collected are displayed directly on an oscilloscope for the two outer and the middle Faraday cups in the array. The apertures of the other two cups are covered with silicon wafer chips. A number of laser shots are then made to deposit boron on the silicon chips, at the same time summing the charge collected on either side of the chips. Table 1 shows the results of one such run. In this particular case, cup A was on the side of the normal toward the laser beam, and the results show the asymmetry toward the laser beam which was reported earlier.<sup>27</sup> The uniformity of  $\pm 2\%$  over the 3 cm interval between cups A and M is acceptable for now, but the  $\pm 8\%$  variation between cups B and M is not. This run shows a particular strong dependence on angle, a dependence itself dependent on laser conditions as noted above.

The silicon chips deposited with boron in runs like Table 1 are presently being analyzed on an Applied Research Laboratories IMMA (Ion Microprobe Mass Analyzer). A schematic diagram of this instrument is shown as Figure 6. It will be used extensively in early work before actual semiconductor devices are implanted,

Table 1. Boron on Silicon Experimental Results

SHOT NUMBER	RELATIVE LASER ENERGY	CHARGE COLLECTED (MICROCOULOMBS)		
		CUP A	CUP M	CUP B
1	13.1	OFF SCREEN (~1.05)	.98	.80
2	9.9	.98	.92	.79
3	8.5	.79	.77	.67
4	8.6	.75	.73	.63
5	8.4	.78 4.35	.75 4.15	.65 3.54

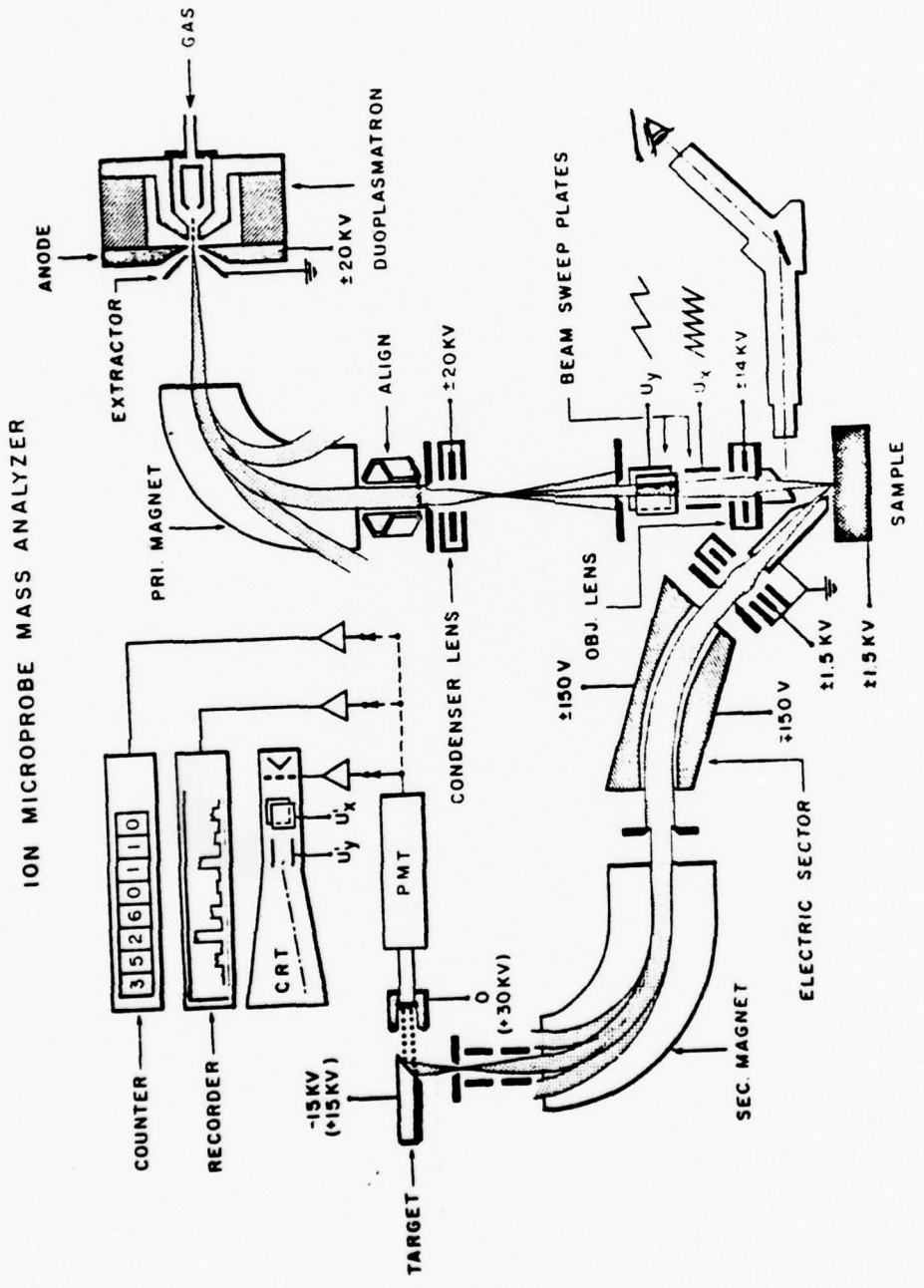


Figure 6. Applied Research Laboratories IMMA  
(Ion Microprobe Mass Analyzer)

in order to determine implant uniformity, purity, and depth profiles. Actual semiconductor device implants will of course be necessary to prove the effectiveness of the blow-off implant method in the final analysis.

Tests using high energy accelerated ions have just commenced and no meaningful report can be made at this time.

## REFERENCES

1. "Laser Annealing Shows Promise for Making p-n Junctions", Physics Today, July 1978.
2. "Laser Annealing: Processing Semiconductors Without a Furnace", Science, 28 July 1978.
3. R.T. Young, et al, Appl. Phys. Lett., 32(3), 139, 1 February 1978.
4. A. Gat and J.F. Gibbons, Appl. Phys. Lett., 32(3), 142, 1 February 1978.
5. A. Gat and J.F. Gibbons, Appl. Phys. Lett., 32(5), 276 1 March 1978.
6. G.K. Celler, et al, Appl. Phys. Lett., 32(8), 464, 15 April 1978.
7. H.J. Leamy, et al, Appl. Phys. Lett., 32(9), 535, 1 May 1978.
8. R.T. Young, et al, Appl. Phys. Lett., 33(1), 14, 1 July 1978.
9. P. Baeri, et al, Appl. Phys. Lett., 33(2), 137, 15 July 1978.
10. K. Affolter, et al, Appl. Phys. Lett., 33(2), 185, 15 July 1978.
11. S.S. Lau, et al., Appl. Phys. Lett., 33(2), 130, 15 July 1978.
12. J.C. Bean, et al., Appl. Phys. Lett., 33(3), 227, 1 August 1978.
13. J.C. Muller, et al., Appl. Phys. Lett., 33(4), 287, 15 August 1978.
14. J.S. Williams, et al., Appl. Phys. Lett., 33(6), 542, 15 September 1978.
15. D.H. Auston, et al, Appl. Phys. Lett., 33(6), 539, 15 September 1978.
16. C.W. White, et al., Appl. Phys. Lett., 33(7), 662, 1 October 1978.
17. R.L. Cohen, et al, Appl. Phys. Lett., 33(8), 751, 15 October 1978.
18. A. Gat, et al., Appl. Phys. Lett., 33(8), 775, 15 October 1978.

19. M. von Allmen, et al., Appl. Phys. Lett., 33(9), 824, 1 November 1978.
20. M. Miyao, et al., Appl. Phys. Lett., 33(9), 828, 1 November 1978.
21. W.A. Porter, et al., Appl. Phys. Lett., 33(10), 15 November 1978.
22. J.M. Poate, et al., Appl. Phys. Lett., 33(11), 918, 1 December 1978.
23. H.A. Bomke, et al., Appl. Phys. Lett., 33(11), 955, 1 December 1978.
24. J. Narayan, R.T. Young, and C.W. White, J. Appl. Phys. 47(7), 3912 (1978).
25. G.N. Marcas, et al., Appl. Phys. Lett., 33(5), 453, 1 September 1978.
26. N.R. Isenor, Appl. Phys. Lett., 31, 148 (1977).
27. "Intense Accelerated Metal Ion Beam Utilizing Laser Blow-off", J.F. Friichtenicht, N.G. Utterback, and J.R. Valles, Rev. Sci. Instru., 47, 1489 (1976).
28. "Atomic and Ionic Beam Source Utilzing Pulsed Laser Blow-off", N.G. Utterback, S.P. Tang, and J.F. Friichtenicht, Physics of Fluids, 19, 900 (1976).

APPENDIX A

CONTRIBUTION OF FREE ELECTRONS TO  
OPTICAL ABSORPTION IN SEMICONDUCTORS

## I. INTRODUCTION

The purpose of this report is to establish whether free carrier contribution to optical absorption in semiconductors will significantly modify absorption characteristics of intrinsic semiconductors. The work which is described in this report has been stimulated by an idea of using lasers for processing of surface regions of semiconductor materials.

Laser-induced surface processing (LISP) is based on the notion that, when irradiated by a laser whose radiation is strongly absorbed in the processed material, the surface of the irradiated material is elevated to high temperatures in controllable manners. In the usual mode of operation, LISP uses a high-power laser whose frequency is higher than the semiconductor band gap frequency, thus causing in it band-to-band transitions. High densities of free carriers may result due to photoexcitation of electrons into the conduction band. One then asks whether these high densities will contribute significantly to the optical properties of the absorbing material, specifically, to its absorption characteristics. Significant changes in the optical properties of the semiconductor would in turn affect absorption of the laser beam, i.e., the process through which the carriers have been created.

It is well known that high concentrations of free carriers in metals may cause significant absorption in visible or infrared, due to collective motion of the carriers. The absorption peaks up just below the plasma frequency. In semiconductors, high carrier concentrations may be obtained by heavy doping of the semiconductors, thermal excitation at elevated temperatures, carrier photo-generation and current injection, among other things. The relative importance of the contribution of the free carriers to optical absorption will depend on the radiation frequency. In the frequency region below the band gap energy, free carrier absorption may be the major mechanism of optical absorption. In the frequency region above the band gap energy, band-to-band transitions may be expected to be stronger than collective excitations unless the carrier concentration is very high. Thus, the strength of the absorption is expected to depend on the number of free carriers, carrier lifetimes and frequency. It is the carrier contribution to optical absorption in the frequency region above the bandgap frequency which is of interest in LISP.

The increase in the number of free carriers in strongly absorbing semiconductors during LISP is due to (i) carrier photogeneration and (ii) thermal excitation of a large number of free carriers. As has already been noted, the primary mechanisms for optical absorption in strongly-absorbing semiconductors are band-to-band transitions, creating (for long pulse length and long carrier lifetimes) large instantaneous concentrations of photo-electrons. The source of the thermally excited electrons is heat; thermal excitations occur after carriers photo-excited into the conduction band relax back into the valence band, transferring optical energy to thermal vibrations of the lattice.

It may be of interest to note here that thermal runaway in semiconductor laser windows is caused by thermal excitations. These windows are fabricated from intrinsic semiconductors transparent to the laser frequency. However, for high power lasers, even a very low residual absorption causes the window to heat up, thus thermally exciting carriers into the conduction band and rapidly increasing absorption with temperature.

This report will be organized as follows. The number of photo-excited and thermally-generated carriers during LISP will be calculated in Section II. The diffusion equation will be used for estimating values of instantaneous densities of the photogenerated carriers. A theory of optical absorption through collective motion of free electrons is developed in Section III. In Section IV we calculate the absorption coefficient due to the free electrons as a function of frequency and further discuss our results.

## II. CARRIER CONCENTRATION

### II.1 TRANSPORT OF PHOTOGENERATED CARRIERS

The instantaneous concentration of photogenerated carriers  $n(x,t)$  in a semiconductor in the absence of an accelerating electric field is obtained in the low carrier concentration approximation by solving the following diffusion equation,

$$\frac{dn}{dt} = g - \frac{\Delta n}{\tau} + D \frac{\partial^2 n}{\partial x^2} , \quad (1)$$

where the generation function  $g$  gives the photogeneration rate of the carriers,

$$g = \alpha F e^{-\alpha x} , \quad (2)$$

where  $\alpha$  is optical absorption coefficient and  $F = F(t)$  gives the rate of the photon flux incident at a unit surface of the semiconductor.

$$\Delta n = n(x,t) - n_0 , \quad (3)$$

where  $n_0$  is the equilibrium carrier concentration,  $\tau$  and  $D$  are minority carrier lifetimes and diffusion constant, respectively.

Assuming that  $g$ ,  $\tau$  and  $D$  are independent of carrier concentration, Eq. (1) can be solved by using Green function techniques. For the boundary conditions,

$$j(x=0,t) \equiv - D \frac{\partial n}{\partial x} \Big|_{x=0} = 0 \quad (4)$$

and

$$n(x = \infty) = n_0 , \quad (5)$$

the Green function is

$$G(x,x',t-t') = \frac{1}{\sqrt{4\pi D(t-t')}} \sum_{n=-\infty}^{+\infty} \left( e^{-\frac{(x-x'-2n\ell)^2}{4D(t-t')}} + e^{-\frac{(x+x'-2n\ell)^2}{4D(t-t')}} \right) e^{-\frac{(t-t')}{\tau}} (-1)^n , \quad (6)$$

where  $\ell$  is the semiconductor thickness. The boundary conditions (4) and (5) describe the physical situation when there is no flux of carriers across the semiconductor front surface, and carrier concentration at the slab back boundary is constant ( $n_0$  is the equilibrium minority carrier concentration).

The solution of Eq. (1) is then given by

$$n(x,t) = \int_0^\infty dx' \int_0^t dt' G(x,x', t-t') g(x',t') , \quad (6)$$

where the generation function  $g(x,t)$  is given by Eq. (2).

For the slab thickness  $\ell$  such that

$$\ell \gg 1/\alpha , \quad (7)$$

the semiconductor can be replaced by a semi-infinite medium, with the result that the summation  $\sum_n$  in Eq. (6) is reduced to one term, namely, term  $n=0$ . Carrier concentration is then equal to

$$n(x,t) = \int_0^\infty dx' \int_0^t dt' G(x,x', t-t') \alpha F(t') e^{-\alpha x'} , \quad (8)$$

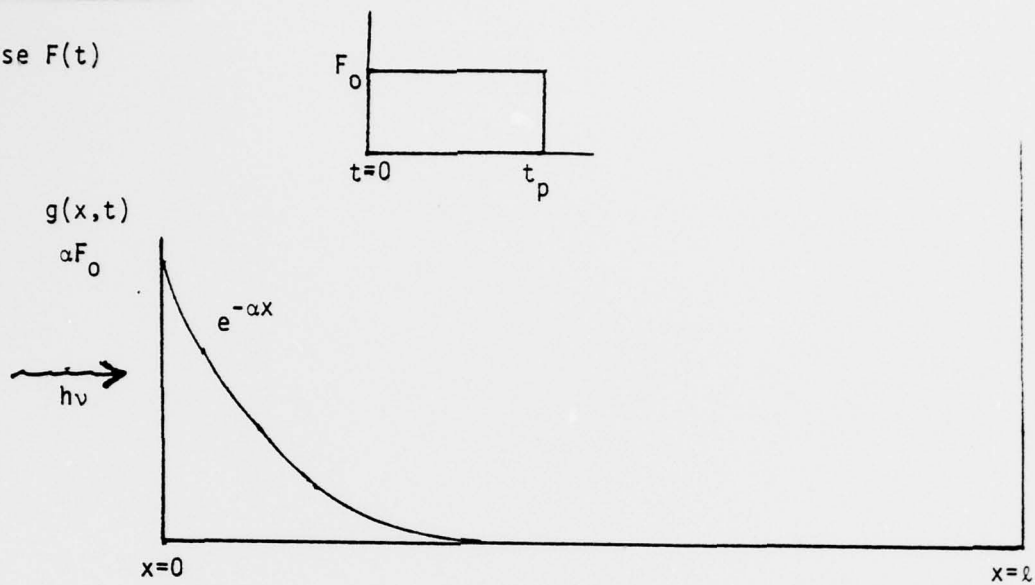
where the Green function is

$$G(x,x',t-t') = \frac{1}{\sqrt{4\pi D(t-t')}} e^{-\frac{(t-t')}{\tau}} \left( e^{-\frac{(x-x')^2}{4D(t-t')}} + e^{-\frac{(x+x')^2}{4D(t-t')}} \right) . \quad (9)$$

Our reason for solving the transport equation is to find out whether the instantaneous concentration of photoexcited carriers is sufficiently large so that the strength of free carrier-induced optical absorption becomes comparable with band-to-band absorption. In order to estimate the strength of the effect, we have evaluated the concentration of carriers photoexcited at the semiconductor front surface for a square shape laser pulse (see Figure 1). Carrier concentration at  $x = 0$  gives an upper estimate for concentrations inside the semiconductor ( $x > 0$ ).

## Light Absorption

Pulse F(t)



## Carrier Transport

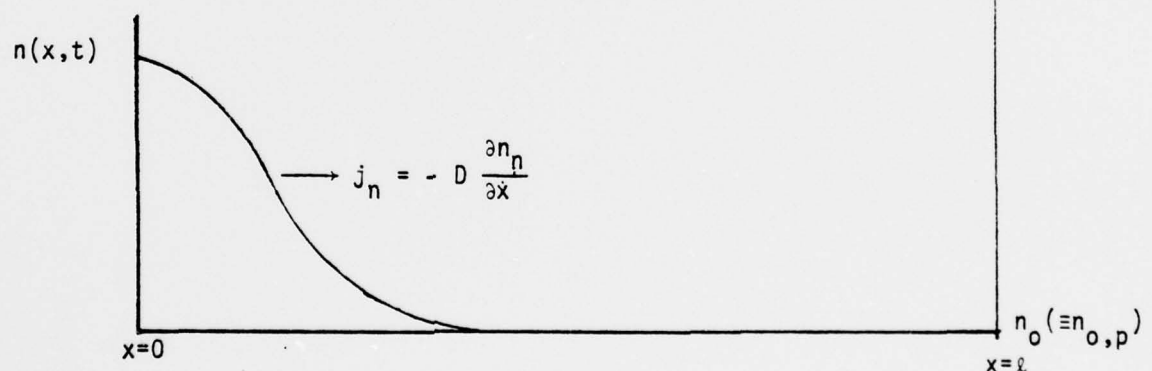


Figure 1. Photogeneration and transport of carriers in a semiconductor slab.

For the square-shape laser pulse, the generation function  $F(t)$  is equal to

$$\begin{aligned} F(t) &= F_0 & 0 < t < t_p , \\ F(t) &= 0 \end{aligned} \quad (10)$$

where  $t_p$  is the length of the laser pulse and  $F_0$  is a (constant) number of arriving photons at the semiconductor front surface. Using Eqs. (9) and (10), Eq. (8) then reduces to

$$n(x=0, t) = \int_{t-t_p}^t dt' e^{-t'(\frac{1}{\tau} - D\alpha^2)} \operatorname{erfc}(\alpha\sqrt{Dt'}) , \quad (11)$$

where  $\operatorname{erfc}(z)$  is the complementary error function.

Clearly, the number of the photogenerated carriers is largest at the end of the laser pulse. Since, for our purposes, we are interested in the maximum values of the concentration of the photo-excited carriers, in what follows, we shall be concerned with the integral,

$$n(0, t_p) = \alpha F_0 \int_0^{t_p} dt e^{-t(\frac{1}{\tau} - D\alpha^2)} \operatorname{erfc}(\alpha\sqrt{Dt}) . \quad (12)$$

Inspecting Eq. (12), we find that there exist various physical regimes of our interest characterized by relative length of three time constants: laser pulse length ( $t_p$ ), carrier lifetime ( $\tau$ ) and "diffusion" time ( $1/D\alpha^2$ ). In order to obtain approximate expressions for the concentrations, in what follows, we shall therefore evaluate Eq. (12) in the following limits:

1. Steady state or a very long pulse limit:  $t_p \gg \tau, t_p \gg 1/D\alpha^2$ .

Setting the integral upper boundary to infinity,  $t_p \rightarrow \infty$ , Eq. (10) yields

$$n(0, t_p) \approx \frac{\alpha F_0 \tau}{1 + \alpha L} , \quad (13)$$

where the diffusion length  $L = \sqrt{Dt}$ . That is, photocarrier concentration is limited by the length of the carrier lifetime or the length of the diffusion time, whichever is smaller. Here, the "diffusion time" is defined as the length of time it takes the carrier to diffuse away from the surface region (of the depth  $1/\alpha$ ), where the carrier was originally created, into the semiconductor interior.

## 2. Short pulse.

### 2.1 Pulse shorter than diffusion time: $t_p < 1/D\alpha^2$ .

Expanding the error function for small arguments, Eq. (12) yields

$$n(0, t_p) \approx \alpha F_0 \frac{\left( e^{-t_p(\frac{1}{\tau} - D\alpha^2)} - 1 \right)}{D\alpha^2 - \frac{1}{\tau}} . \quad (14)$$

In order to better understand the physical content of this result, we further reduce Eq. (14) in the following limits:

#### 2.1.1 $\tau < t_p$ ( $t_p < 1/\alpha^2 D$ ).

$$n(0, t_p) \approx \alpha F_0 \tau . \quad (15)$$

For the carrier lifetime shortest of the three time constant, carrier concentration is carrier lifetime-limited.

#### 2.1.2 $t_p < \tau$ ( $\tau < 1/\alpha^2 D$ or $\tau < 1/\alpha^2 D > t_p$ ).

$$n(0, t_p) \approx \alpha F_0 t_p . \quad (16)$$

For the pulse length shorter than the carrier lifetime, the concentration is pulse length-limited.

### 2.2 Pulse longer than diffusion time: $t_p > 1/D\alpha^2$ .

In this limit, the integral in Eq. (12) is broken into two intervals, namely,  $t < 1/D\alpha^2$  and  $t > 1/D\alpha^2$ . In the first interval, the error function is expanded for small arguments. In the second interval, the error function is expanded for large arguments. We obtain

$$n(0, t_p) = \alpha F_0 \int_0^{1/\alpha^2 D} dt e^{-t(\frac{1}{\tau} - D\alpha^2)} \left( 1 - \frac{1}{\sqrt{\pi}} \alpha \sqrt{Dt} \right) + \int_{1/\alpha^2 D}^{t_p} dt \frac{e^{-t/\tau}}{\sqrt{\pi} \alpha \sqrt{Dt}}$$

$$= \alpha F_0 \left[ \frac{e^{-\frac{1}{\alpha^2 D}(\frac{1}{\tau} - D\alpha^2)}}{D\alpha^2 - \frac{1}{\tau}} - 1 + \frac{1}{\alpha} \sqrt{\frac{\tau}{D}} \left( \operatorname{erf} \sqrt{\frac{t_p}{\tau}} - \operatorname{erf} \left( \frac{1}{\alpha \sqrt{D\tau}} \right) \right) \right] . \quad (17)$$

A further insight into Eq. (17) is obtained by reducing it into simpler expressions for the following limiting cases:

### 2.2.1 $t_p < \tau$ ( $t_p > 1/D\alpha^2$ ).

Equation (17) reduces to

$$n(0, t_p) \approx F_0 \sqrt{\frac{t_p}{D}} . \quad (18)$$

This result, Eq. (18), can be better understood by rewriting it into the following form,

$$n(0, t_p) \approx \frac{F_0}{\sqrt{Dt_p}} \cdot \frac{1}{\frac{t_p}{\tau}} . \quad (18')$$

Notice that the denominator of Eq. (18') has the dimension of velocity. That is, for  $t_p < \tau$ , carrier concentration is limited by carrier diffusion within the time interval equal to the length of the laser pulse.

### 2.2.2 $1/D\alpha^2 < \tau < t_p$ .

Equation (17) reduces to

$$n(0, t_p) \approx F_0 \sqrt{\frac{\tau}{D}} , \quad (19)$$

which can be rewritten as

$$n(0, t_p) \approx \frac{F_0}{\sqrt{D\tau}} \cdot \frac{1}{\frac{\tau}{\tau}} . \quad (19')$$

That is, by analogy with Eq. (18'), for  $\tau < t_p$ , the concentration is limited by carrier diffusion within the time interval equal to the carrier lifetime.

$$2.2.3 \quad \underline{\tau < 1/D\alpha^2 < t_p} .$$

Equation (17) reduces to

$$n(0, t_p) \approx \alpha F_0 \tau . \quad (20)$$

That is, carrier concentration is limited by carrier lifetime. (It should be noted here that Eqs. (19) and (20) in fact reproduced the steady state result, viz., Eq. (13)).

The results, Eqs. (13) through (20), are summarized in Table 1. It is seen that the following "rule-of-thumb" applies. The surface concentration of the photoexcited carriers is limited by the length of the shortest time interval in the problem,  $t_p$  or  $\tau$ , if these are the shortest time intervals; or, in the case of fast carrier diffusion, by diffusion of carriers within the time interval  $t_p$  or  $\tau$ , whichever is shorter. Comments in the third column of Table 1 refer to real physical cases to which the respective limiting expressions apply. The values of the representative parameters (i.e., time constants, mobilities, diffusivities) used for identifying the various physical regimes are also listed in Table 1. In the last column of Table 1 are listed plasma frequencies corresponding to the maximum concentrations (column four). The plasma frequencies were obtained by evaluating the expression,

$$\omega_p = \left( \frac{4\pi n e^2}{\epsilon m_e} \right)^{1/2} , \quad (21)$$

where  $\epsilon$  is the dielectric constant and  $m_e$  is electron effective mass. The maximum concentrations were evaluated for the photon flux  $F_0 = 3 \times 10^{25} \text{ cm}^{-2} \text{s}^{-1}$ , where  $F_0 = P_0/\hbar v$ .  $P_0$  is the peak power of the ruby laser ( $\lambda = .6943 \mu\text{m}$ ) and was taken  $P_0 = 10^7 \text{ W/cm}^2$ . The pulse width was 30 nanoseconds. The pulse was square-shaped.

## II.2 SURFACE RECOMBINATION VELOCITY

The effect of the presence of the surface in the vicinity of the active region is to introduce additional carrier-loss mechanism into the problem. It is customary to define an effective surface recombination velocity  $s$  of minority carriers by the expression:

$$D \frac{\partial n}{\partial x} \Big|_{x=0} = s \Delta n(0) = s(n(0) - n_0) , \quad (22)$$

TABLE I. MAXIMUM INSTANTANEOUS CONCENTRATIONS OF PHOTOEXCITED ELECTRONS AT THE SURFACE  
OF A P-TYPE SEMICONDUCTOR IRRADIATED BY A SQUARE-SHAPE RUBY LASER PULSE  
OF THE PEAK POWER  $P_0 = 10^7 \text{ W/cm}^2$ .

PHOTOELECTRON CONCENTRATIONS

Physical Regime		Concentrations		Comments	
$t_p > \tau_n$	$\tau_n > 1/D_n \alpha^2$	$F_0 \tau_n / L_n$		$n_p (\text{cm}^{-3})$	$\omega_p (\text{s}^{-1})$
$t_p < \tau_n$	$\tau_n < 1/D_n \alpha^2$	$\alpha F_0 \tau_n$	Quality and lightly damaged GaAs	$\approx 2 \times 10^{20}$	$\approx 3 \times 10^{14}$
	$\tau_n < 1/D_n \alpha^2$	$\alpha F_0 \tau_n$	Damaged GaAs	$\approx 3 \times 10^{18}$	$\approx 4 \times 10^{13}$
$t_p < \tau_n$	$\tau_n > 1/D_n \alpha^2$	$F_0 \sqrt{t_p / D_n}$	Quality and damaged silicon	$\approx 3 \times 10^{21}$	$\approx 1.2 \times 10^{14}$
	$\tau_n > 1/D_n \alpha^2$	$\alpha F_0 t_p$			
$t_p < \tau_n$	$\tau_n < 1/D_n \alpha^2$	$\alpha F_0 t_p$			

SEMICONDUCTOR PARAMETERS ( $T = 300^\circ\text{K}$ ,  $\alpha = 10^4 \text{ cm}^{-1}$ ,  $t_p = 3 \times 10^{-8}$  seconds)

Semi-conductor	Quality				Heavily Damaged		
	$\tau_n (\text{s})$	$\mu_n (\frac{\text{cm}^2}{\text{Vs}})$	$D_n (\frac{\text{cm}^2}{\text{s}})$	$L_n (\text{cm})$	$\frac{1}{D_n \alpha^2} (\text{s})$	$\mu_n (\frac{\text{cm}^2}{\text{s}})$	$D_n (\frac{\text{cm}^2}{\text{s}})$
Silicon	$10^{-3}$	$10^3$	25	.15	$4 \times 10^{-10}$	$10^{-7}$	$10^2$
GaAs	$10^{-8}$	$8 \times 10^3$	200	$1.4 \times 10^{-3}$	$5 \times 10^{-11}$	$10^{-11}$	$25$

where  $n_0$  is equilibrium concentration of minority carriers. Thus, if one wishes to account for the effect of the surface recombination on carrier concentration, Eq. (22) will replace the boundary condition, Eq. (4), of the previous section.

The transport equation, Eq. (1), with the boundary conditions, Eqs. (5) and (22) may be solved using again the Green function techniques. We have not constructed complete Green function for this problem. However, we have solved Eq. (1) directly for the case of the steady state. In the steady state, solution to Eq. (1) with the boundary conditions Eq. (5) and (22) and with the source term Eq. (2) applied over a long period of time, is

$$\Delta n = \frac{\alpha F \tau}{1 - \alpha^2 L^2} \left( -\frac{(s + \alpha D)}{s + L/\tau} e^{-x/L} + e^{-\alpha x} \right), \quad (23)$$

where all parameters were defined in Section 2.1.

Taking the limit of large  $s$ ,  $s > \alpha D$  and  $s > L/\tau$ , Eq. (23) reduces at  $x = 0$  to the simple expression:

$$\Delta n(0) \approx \frac{F_0}{s(1 + 1/L\alpha)}. \quad (24)$$

Thus, in the case of a rapid surface recombination, concentration of photoexcited carriers is limited by surface recombination velocity,  $s$ , as expected. Intuitively, one expects a similar result also for the transient case: For a finite pulse length, carrier concentration will be surface recombination-limited if the surface velocity is higher than any of the other characteristic velocities in the problem, i.e., if

$$s > \left( \frac{1}{\alpha \tau}, \frac{L}{\tau}, \frac{1}{\alpha t_p}, \alpha D \right). \quad (25)$$

In the other cases, i.e., for the surface recombination slower than any of the characteristic velocities, carrier concentrations will be limited by the corresponding velocities, viz., Eqs. (15) through (20).

### II.3 THERMAL EXCITATIONS

Heating the semiconductor to high temperatures will have a threefold effect on the semiconductor properties: (i) increase of intrinsic carrier

densities, (ii) increase of extrinsic carrier densities, and (iii) temperature dependence of carrier lifetimes, mobilities and diffusivities.

### II.3.1 Intrinsic Carrier Densities

Intrinsic carrier densities of Ge, Si and GaAs as a function of reciprocal temperature are shown in Figure 2.

### II.3.2 Extrinsic Carrier Densities

In the limit of low temperature ( $kT < E_g - E_d$ ) or a high doping concentration, the ratio of ionized dopants at temperature  $T_1$  and  $T_2$  is

$$\frac{n(T_2)}{n(T_1)} \approx \exp \left[ -\frac{E_g - E_d}{2k} \left( \frac{1}{T_2} - \frac{1}{T_1} \right) \right], \quad (26)$$

where  $E_g - E_d$  is the position of the dopant level below the bottom of the conduction band. In the limit of high temperature, or low doping, the ionized dopant concentration is approximately constant, equal to the total dopant concentration,

$$n \approx N .$$

Thus, at elevated temperatures, the maximum concentration of extrinsic electrons is equal to the dopant concentration, yielding the following plasma frequencies ( $\omega_p = (4\pi n e^2 / \epsilon_m)^{1/2}$ ):

$$\text{GaAs} \qquad \omega_p \approx 6.2 \times 10^4 \sqrt{N} \quad (27a)$$

$$\text{Si} \qquad \omega_p \approx 2 \times 10^4 \sqrt{N} \quad (27b)$$

### II.3.3 Temperature Dependence of Physical Constants

Temperature dependence of semiconductor parameters such as lifetimes, mobilities and diffusivities is rather complex. In the context of the present investigation, changes in temperature will modify intervals of physical regimes defined in Table 1 of Section II.2. Due to their complexity, and their comparatively small effect, we shall neglect these temperature changes in the present problem.

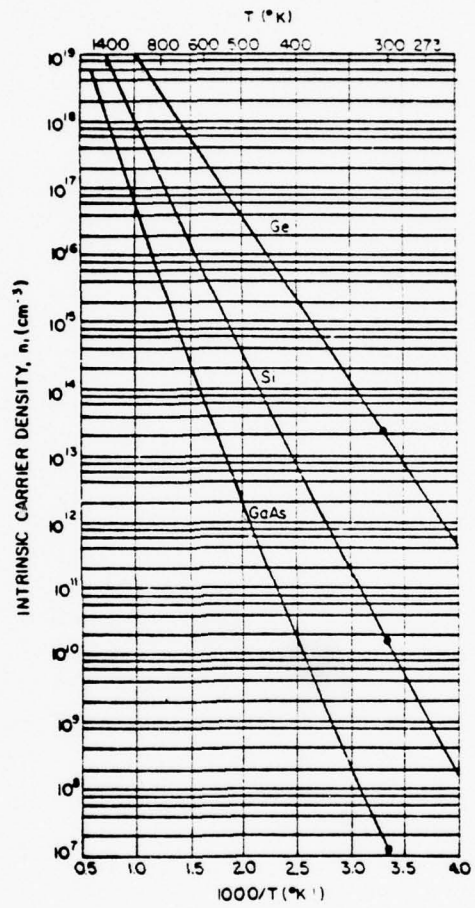


Figure 2. Intrinsic carrier densities of Ge, Si, and GaAs as a function of reciprocal temperature.

### III. EFFECTS OF FREE ELECTRONS ON SEMICONDUCTOR ABSORPTION

#### III.1 PROPAGATION OF ELECTROMAGNETIC WAVES IN A LOSSY MEDIUM

Attenuation of electromagnetic waves in semiconductors follows from solving Maxwell Equations in a conducting medium. Solving the Maxwell Equations for the electromagnetic wave,

$$E = E_0 \exp [i(\bar{k}x - \omega t)] , \quad (28)$$

propagating in a lossy medium, one obtains for the complex (frequency-dependant) wave vector  $\bar{k}$ ,

$$\bar{k}^2 = \bar{\epsilon} \frac{\omega^2}{c^2} , \quad (29)$$

where  $\omega$  is the angular frequency and the generalized complex dielectric constant  $\bar{\epsilon}$  is

$$\bar{\epsilon} = \epsilon + i \frac{4\pi\sigma}{\omega} . \quad (30)$$

Alternatively, since the generalized complex conductivity is

$$\bar{\sigma} = \sigma + \frac{i\omega}{4\pi} (1 - \epsilon) . \quad (31)$$

Equation (31) can be rewritten as

$$\bar{\epsilon} = 1 + \frac{i4\pi\bar{\sigma}}{\omega} . \quad (32)$$

In Eqs. (29) - (32),  $\bar{\epsilon}, \bar{\sigma}$  and  $\epsilon, \sigma$  are complex and real quantities, respectively, and are functions of angular frequency  $\omega$ . Using Eq. 30, the generalized refractive index  $\bar{n}$ ,

$$\bar{n} \equiv \sqrt{\bar{\epsilon}} = n + ik , \quad (33)$$

can be written as

$$n^2 - k^2 = \epsilon \quad (34)$$

$$kn \frac{\omega}{2\pi} = \sigma , \quad (35)$$

where  $n$  is the real part of the generalized refractive index  $\bar{n}$  and  $\kappa$  (the imaginary part of  $\bar{n}$ ) is related to the extinction coefficient  $\alpha$  (extinction of energy carried by the electromagnetic wave), by

$$\alpha = 2\kappa \frac{\omega}{c} . \quad (36)$$

Hence, the absorption coefficient  $\beta$  (describing attenuation of the amplitude of the electromagnetic wave) is equal to

$$\beta \equiv \frac{\alpha}{2} = \kappa \frac{\omega}{c} \quad (37)$$

and the electromagnetic wave is

$$E = E_0 e^{i(kx - \omega t) - \beta x} . \quad (38)$$

We note that Eqs. (34) and (35) can be rewritten alternatively as

$$n^2 = \frac{1}{2} \left( \epsilon + \sqrt{\epsilon^2 + 16\pi^2 \frac{\sigma^2}{\omega^2}} \right) \quad (39)$$

$$\kappa^2 = \frac{1}{2} \left( -\epsilon + \sqrt{\epsilon^2 + 16\pi^2 \frac{\sigma^2}{\omega^2}} \right) , \quad (40)$$

giving  $n$  and  $\kappa$  directly in terms of  $\epsilon$  and  $\sigma$ . Once the dielectric constant and conductivity are known, the above Equations completely describe dispersion and attenuation of electromagnetic waves propagating in a lossy medium.

### III.2 ELECTRON SUSCEPTIBILITY AND CONDUCTIVITY

In a radiation field, the current of the free carriers has a component in phase and a component out of phase with the electric field. The in-phase current contributes to the conductivity and the out-of-phase component contributes to the susceptibility. In order to estimate the free carrier contribution to  $\sigma$  and  $\epsilon$ , it is convenient to employ a model of a damped oscillator. In this model, carrier motion is described by the following equation of motion,

$$m(\ddot{x} + \tau^{-1}\dot{x} + \omega_0^2 x) = eE_0 e^{-i\omega t}, \quad (41)$$

where the damping constant  $\tau$  is electron "relaxation" time and  $\omega_0$  is the restoring force. Since, for free carriers, there is no local restriction on their motion, in what follows, the restoring force will be neglected.

Putting  $\omega_0 = 0$ , and using the definitions polarization  $P = n\epsilon x$  and current  $j = n\epsilon \dot{x}$ , we obtain

$$\bar{\epsilon} \equiv \epsilon_0 + 4\pi \frac{P}{E} = \left(1 + \frac{i\omega_p^2 \tau}{\omega(1 - i\omega\tau)}\right) \epsilon_0, \quad (42)$$

$$\bar{\sigma} \equiv \frac{j}{E} = \frac{n\epsilon^2 \tau}{m(1 - i\omega\tau)}, \quad (43)$$

where  $\omega_p$  is the plasma frequency,  $\omega_p^2 = (\frac{4\pi n e^2}{\epsilon m})$ , and  $n$  is the free electron density. It is straightforward to verify that Eqs. (42) and (43) satisfy the relations of Section III.1. Rewriting Eqs. (42) and (43) as

$$\epsilon = \left(1 - \frac{\omega_p^2 \tau^2}{1 + \omega_p^2 \tau^2}\right) \epsilon_0 \quad (44)$$

and

$$\sigma = \frac{n\epsilon^2 \tau}{m(1 + \omega_p^2 \tau^2)}, \quad (45)$$

and substituting them into Eqs. (39) and (40), the absorption coefficient can now be evaluated.

The final remark will concern time constant  $\tau$ .  $\tau$  is the relaxation time, which, in the context of the damped oscillator model, is related to carrier mobility,

$$\tau = \mu \frac{m}{e}. \quad (46)$$

where  $m$  and  $e$  are electron effective mass and charge, respectively.

#### IV. ABSORPTION COEFFICIENT

The refraction and absorption coefficients associated with free electrons are calculated by substituting Eqs. (44) and (45) into Eqs. (39) and (40). The results are sketched in Figures 2 through 4.

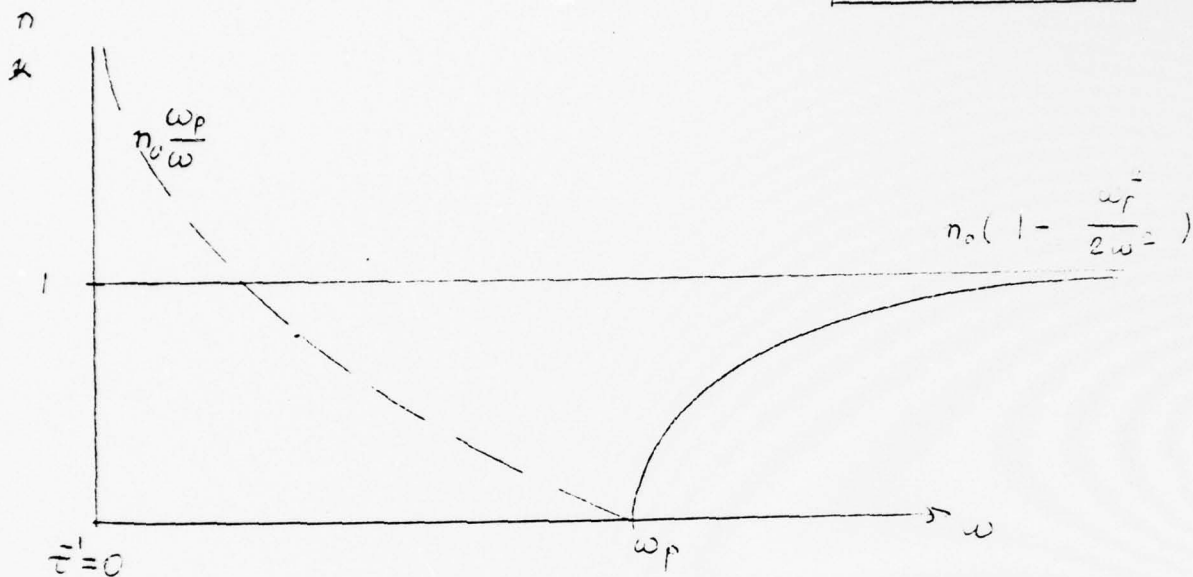
In Figure 3, we plot the qualitative behavior of both the real and imaginary parts of the generalized refractive index versus frequency for the case of  $\tau = \infty$ . This is a rather illustrative case. It shows that, in the absence of any loss mechanism, there is a total reflection at frequencies  $\omega < \omega_p$ . At  $\omega < \omega_p$ , the wave is evanescent with the skin depth  $\delta (\delta \equiv \beta^{-1})$  approaching infinity as frequency  $\omega$  approaches  $\omega_p$ . In the frequency region above the plasma frequency,  $\omega > \omega_p$ , there is zero absorption ( $\kappa = 0$ ), the wave being partially reflected and partially transmitted. There is a practically complete transmission at very high frequencies.

In Figure 4, we sketch the qualitative behavior of real and imaginary parts of the generalized refractive index,  $n$  and  $\kappa$ , respectively, versus frequency for both, the case  $\omega_p > \tau^{-1}$  and  $\omega_p < \tau^{-1}$ . Also noted in Figure 4 are leading terms of expansions of  $n$  and  $\kappa$  versus  $\omega$  in various frequency regimes; that is, regimes defined by relative magnitudes of parameters  $\omega$ ,  $\omega_p$  and  $\tau^{-1}$ . The leading terms were obtained by expanding expressions for  $n$  and  $\kappa$  in terms of smallness parameters appropriate to the various regimes. It is seen that finite values of  $n$  and  $\kappa$  are obtained at all frequencies indicating partial transmission, reflection and absorption of electromagnetic waves in all the frequency regions.

In Figure 5, we sketch qualitatively the imaginary part of the refractive index,  $\kappa$ , and the absorption coefficient  $\beta$ ; Figure 5.1 shows the case of  $\omega_p < \tau^{-1}$  and Figure 5.2 the case  $\omega_p > \tau^{-1}$ . By comparing Figure 5.1 and 5.2, it is seen that the qualitative behavior of  $\beta$  in the two cases is the same. The absorption coefficient starts from zero at  $\omega = 0$  and grows approximately with frequency as  $(\omega)^{1/2}$  until  $\omega$  approaches frequency  $\omega = \omega_p$  or  $\tau^{-1}$ , whichever is smaller. Absorption then levels off (attains maximum value) until the frequency reaches  $\tau^{-1}$  or  $\omega_p$ , whichever is larger. Thereafter,  $\beta$  decays inversely proportional to the second power of the frequency,  $\beta \sim \omega^{-2}$ .

Thus, we can see that there exist several frequency regions in which the absorption coefficient behaves differently. It is easy to verify that, for

$n$	—
$k$	— — —



total reflection      partial reflection and transmission

evanescent wave

skin depth  $\delta$

$$\lim_{\omega \rightarrow \omega_p^-} \delta \rightarrow \infty$$

zero absorption

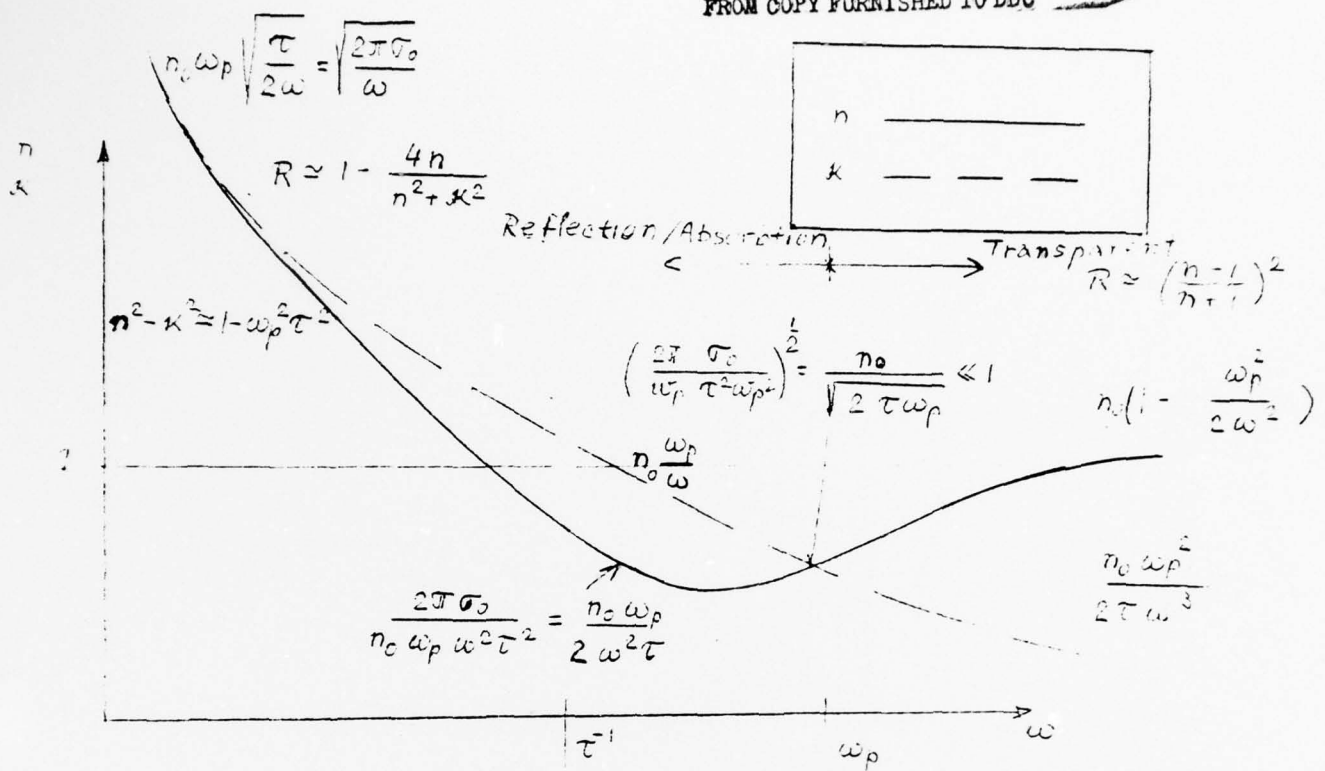
$$R = \frac{(n-1)^2 + k^2}{(n+1)^2 + k^2} \rightarrow \frac{(n-1)^2}{(n+1)^2}$$

$$T = \frac{(1-R)^2 e^{-2\alpha d}}{1-R^2 e^{-2\alpha d}} \rightarrow \frac{1-R}{1+R}$$

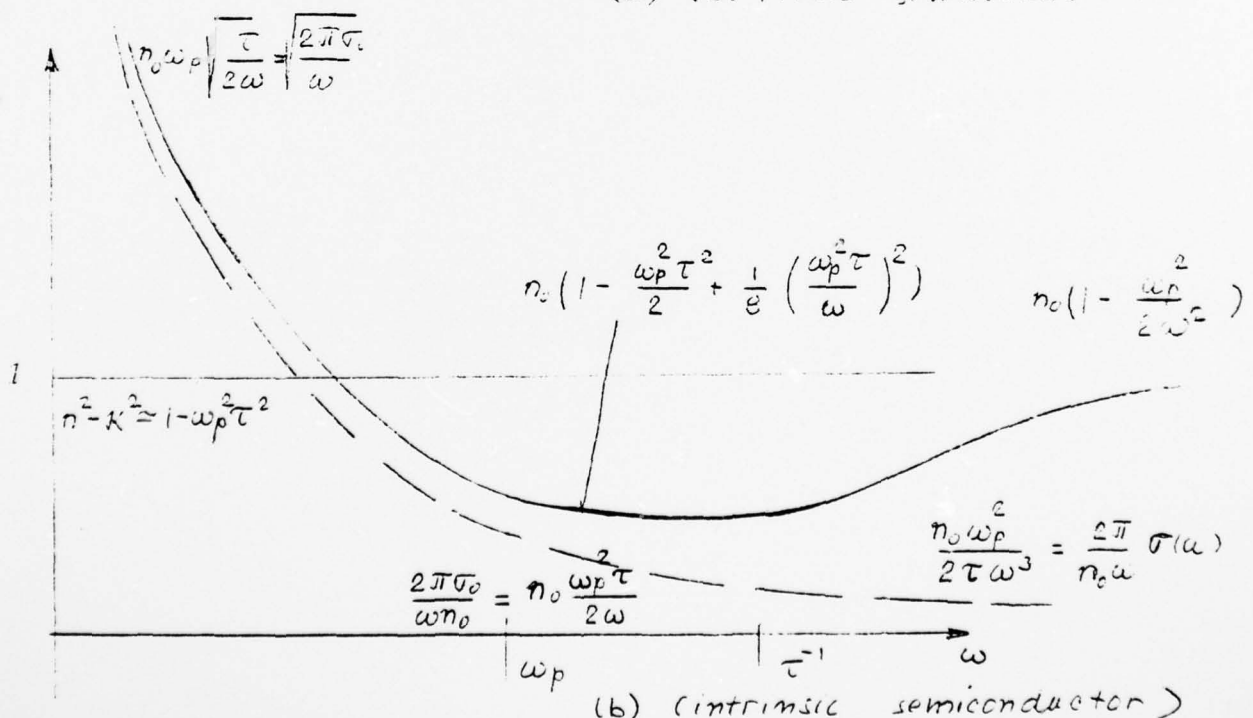
$$A = \frac{(1-R)(1-e^{-\alpha d})}{1-R e^{-\alpha d}} \rightarrow 0$$

(Good metals:  $\tau^{-1} \ll \omega_p$ ,  $\lambda_p \approx 1.3 \mu m$ )

Figure 3. Real ( $n$ ) and imaginary ( $k$ ) parts of the generalized refractive index in the absence of any absorption mechanism. (Good metal approximation:  $\tau^{-1} \ll \omega_p$ ,  $\lambda_p \approx 1.3 \mu m$ .)

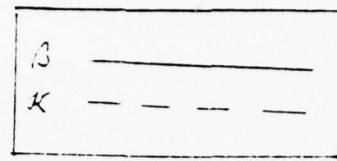


(a) (extrinsic semiconductor)

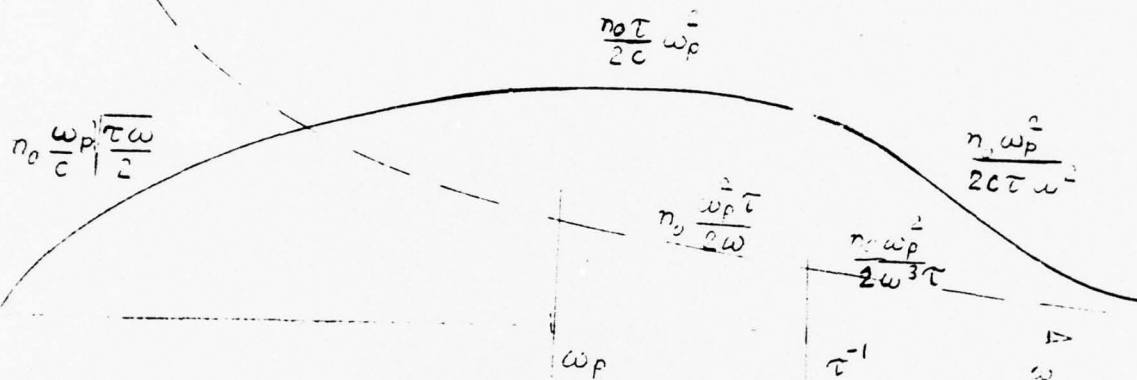


(b) (intrinsic semiconductor)

Figure 4. Qualitative plot of the real ( $n$ ) and imaginary ( $k$ ) parts of the generalized refractive index. a)  $\omega_p > \tau^{-1}$  (extrinsic semiconductor); b)  $\omega < \tau^{-1}$  (intrinsic semiconductor).



THIS PAGE IS BEST QUALITY PRACTICABLE  
FROM COPY FURNISHED TO DDC

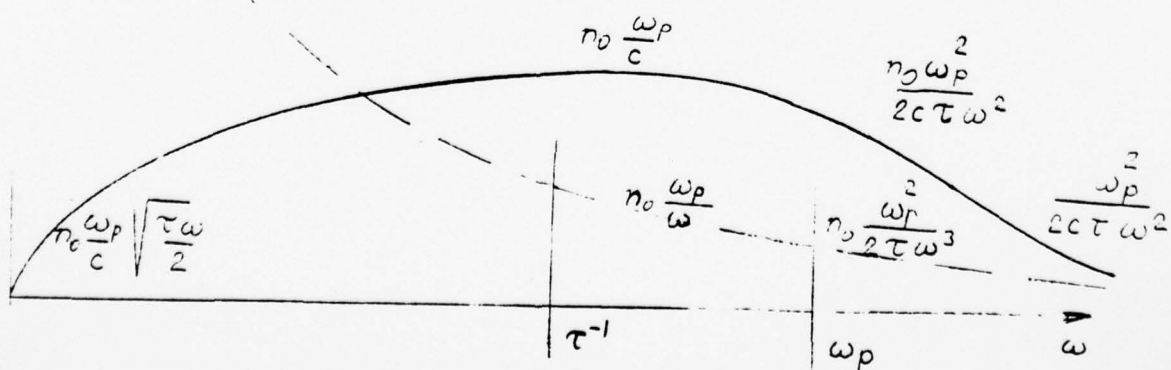


(a) (intrinsic semiconductor)

$$n_r \omega_p \sqrt{\frac{\pi}{2\omega}} \gg 1$$

Refraction  $\approx 1$

Transparent



(b) (extrinsic semiconductor)

Figure 5. Qualitative behavior of the imaginary part of the index of refraction ( $\kappa$ ) and the optical absorption coefficient ( $\beta$ ) due to the free electron effect. (a)  $\tau^{-1} > \omega_p$  (intrinsic semiconductors); b)  $\omega_p > \tau^{-1}$  (extrinsic semiconductors).

semiconductors, unless the semiconductor is intrinsic, the limit of  $\tau^{-1} < \omega_p$  usually applies. Using Eq. (46), one finds that typical values of  $\tau$  range from  $4 \times 10^{-13}$  to  $4 \times 10^{-12}$  seconds (Si, InAs, GaAs and Ge); therefore,  $\tau^{-1} < \omega_p$  for electron concentrations above, typically,  $10^{14} \text{ cm}^{-3}$ . Hence, for most semiconductors, the absorption coefficient  $\beta = \omega_p/c$  in the frequency region of  $\tau^{-1} < \omega < \omega_p$  and  $\beta = \omega_p^2/2c\tau\omega^2$  for frequencies  $\omega > \omega_p$ . A list of calculated values of  $\beta$  at the ruby frequency ( $\lambda = .694 \mu\text{m}$ ) and at  $7 \mu\text{m}$  for silicon, InAs, GaAs and germanium for doping concentrations of  $10^{17}$ ,  $10^{18}$  and  $10^{19} \text{ cm}^{-3}$  is given in Table 2.

In Table 2, the effect of frequency and carrier concentration on values of  $\beta$  is clearly seen. Absorption peaks up in the vicinity of  $\omega = \omega_p$ . With frequencies increasing into the near infrared region of the spectrum, the absorption decreases until, in the visible region of the spectrum, it becomes very small. We note that this region also coincides with the region of the onset of strong band-to-band transitions, hence, in semiconductors, the effect of free carriers on the optical properties becomes important really only at frequencies lower than the bandgap frequency. Whereas at frequencies  $\omega \leq \omega_p$ , the absorption coefficient  $\beta = \omega_p/c \approx 10^4 \text{ cm}^{-1}$  for electron concentration of  $n \approx 10^{19} \text{ cm}^{-3}$ , the value of the absorption coefficient at the band gap frequency is lower than this maximum value by several orders of magnitude.

We note, finally, that in the near infrared region, where the frequency  $\omega > \omega_p$ , it holds that

$$16\pi^2\sigma^2/\omega^2 < \epsilon , \quad (47)$$

and hence,

$$n \approx \sqrt{\epsilon} . \quad (48)$$

In addition, if the carrier concentration is not too high, the dielectric constant  $\epsilon$  may be approximated by its value in the absence of free electrons,  $\epsilon \approx \epsilon_0 = n_0^2$ . Therefore, electrons affect optical properties only through their contribution to conductivity, influencing  $\kappa$  or  $\beta$ , but not  $n$ :

$$\beta = \frac{\omega}{c} \kappa = \frac{2\pi}{n_0} \frac{\sigma}{c} = \frac{n_0 \omega_p^2}{2c \omega^2 \tau} , \quad (49)$$

which is the expression written in Figure 4 for the limit of  $\omega > (\tau^{-1}, \omega_p)$ .

TABLE 2. ABSORPTION COEFFICIENT ASSOCIATED WITH FREE ELECTRONS.

Semiconductor $\tau$ (sec)	$n$ ( $\text{cm}^{-3}$ )	$\omega_p$ (rad)	$\lambda_p$ ( $\mu\text{m}$ )	Absorption Coefficient $\alpha$ ( $\text{cm}^{-1}$ )		
				$\omega = 3 \times 10^{15}$ rad (Ruby: $\lambda = 694 \mu\text{m}$ )	$\omega \approx 2 \times 10^{15}$ rad (Nd: $\lambda = 1.06 \mu\text{m}$ )	$\omega = 3 \times 10^{14}$ rad ( $\lambda = 6.3 \mu\text{m}$ )
Si	$10^{17}$	$7 \times 10^{12}$	269	$10^{-3}$	$3 \times 10^{-3}$	$10^{-1}$
	$10^{18}$	$2 \times 10^{13}$	90	$10^{-2}$	$3 \times 10^{-2}$	1
	$10^{19}$	$7 \times 10^{13}$	27	$10^{-1}$	.3	10
	$10^{20}$	$2 \times 10^{14}$	9	1	3	$10^2$
InAs	$10^{17}$	$3 \times 10^{13}$	63	$3 \times 10^{-2}$	$8 \times 10^{-2}$	3
	$10^{18}$	$10^{14}$	20	$3 \times 10^{-1}$	$8 \times 10^{-1}$	30
	$10^{19}$	$3 \times 10^{14}$	6.3	3	8	$3 \times 10^2$
	$10^{20}$	$10^{16}$	2	30	80	Metallic
GaAs	$10^{17}$	$2 \times 10^{13}$	94	$1.6 \times 10^{-2}$	$4 \times 10^{-2}$	1.6
	$10^{18}$	$7 \times 10^{13}$	30	$1.6 \times 10^{-1}$	$4 \times 10^{-1}$	16
	$10^{19}$	$2 \times 10^{14}$	9.4	1.6	4	160
	$10^{20}$	$7 \times 10^{14}$	3	16	40	Metallic
Ge	$10^{17}$	$5 \times 10^{12}$	377	$2 \times 10^{-4}$	$6 \times 10^{-4}$	$2 \times 10^{-2}$
	$10^{18}$	$1.5 \times 10^{13}$	120	$2 \times 10^{-3}$	$6 \times 10^{-3}$	$2 \times 10^{-1}$
	$10^{19}$	$5 \times 10^{13}$	37.7	$2 \times 10^{-2}$	$6 \times 10^{-2}$	2
	$10^{20}$	$1.5 \times 10^{14}$	12	$2 \times 10^{-1}$	$6 \times 10^{-1}$	20

In the usual mode of its operation, LISP utilizes lasers whose radiation is strongly absorbed in the processed material, necessitating frequency regimes above the band gap frequencies. The ruby laser is used for irradiation of semiconductor surfaces in our laboratory. The instantaneous concentrations of free electrons induced at the semiconductor surface by the laser irradiation were calculated in Section I to be on the order or less than  $10^{19}$   $\text{cm}^{-3}$ . Hence, as has already been noted, in the frequency regime above the band gap frequency where the semiconductor is strongly absorbing ( $\alpha \geq 10^4 \text{ cm}^{-1}$ ), optical absorption due to the photoexcited electrons is less than the band-to-band absorption, and hence, the effect of free electrons on the absorption coefficient can be neglected.

## APPENDIX B

### NUMERICAL SOLUTION OF THERMAL AND IMPURITY DIFFUSION DURING LASER-INDUCED PROCESSING

#### Abstract

The temperature profiles obtained in heavily damaged semiconductors after the application of a strongly absorbed laser pulse to the semiconductor surface have been evaluated numerically. The profiles were obtained for several pulse shapes, widths and powers. The laser power required to raise the surface temperature close to the semiconductor melting temperature is a strong function of the optical absorption coefficient,  $\alpha$ , of the semiconductor. For  $\alpha = 10^4 \text{ cm}^{-1}$ , the required powers are on the order of  $10^7 \text{ W/cm}^2$  for a 10 nsec pulse. The temperature profiles were evaluated with the help of an advanced code PDECOL which solves a set of nonlinear partial differential equations. This was the first time PDECOL was used in DSSG.

The impurity profiles in the semiconductor after the application of the laser pulses to the semiconductor have also been obtained. However, impurity diffusion in the semiconductor solid state is very slow. Therefore, numerical methods have been developed which seek redistribution of impurities as a function of the number of the applied pulses, rather than of time. A typical number of the pulses required to induce impurity diffusion of  $100 \text{ \AA}$  is on the order of  $10^5$  pulses. This large number practically eliminates the use of pulsed lasers for inducing impurity diffusion in the semiconductor solid state.

## I. TEMPERATURE DISTRIBUTION

### PROBLEM

The temperature distribution in the semiconductor after the application of the laser pulse in the one-dimensional approximation is obtained by solving the thermal transport equation

$$\frac{\partial T}{\partial t} - \frac{\partial}{\partial x} \left( \frac{\kappa}{c_p} \frac{\partial T}{\partial x} \right) = \frac{S(x,t)}{c_p}, \quad (1)$$

where  $c_p$  and  $\kappa$  are the specific heat and thermal conductivity, respectively, and where the source function  $S$  is equal to the rate of the density of the absorbed power per unit length,

$$S(x,t) = \alpha F(t) e^{-\alpha x}, \quad (2)$$

where  $\alpha$  is the optical absorption coefficient and  $F(t)$  describes the shape of the laser pulse. Equation (2) assumes that the laser energy converts to the thermal energy instantaneously, such as in heavily damaged materials. Thus, for the square, triangular, and "Gaussian" pulse shape, respectively,  $F(t)$  is,

#### Square Shape Pulse

$$F(t) \begin{cases} F_0 & 0 < t < t_p \\ 0 & \text{otherwise} \end{cases}, \quad (3)$$

#### Triangular Pulse

$$F(t) \begin{cases} F_0(t/t_m) & 0 < t < t_m \\ F_0 \frac{t_p - t}{t_p - t_m} & t_m < t < t_p \\ 0 & \text{otherwise} \end{cases}, \quad (4)$$

#### "Gaussian" Pulse

$$F(t) \begin{cases} F_0 \left( 1 - \frac{(t-t_m)^2}{t_m^2} \right) & 0 < t < t_m \\ F_0 e^{-\frac{(t-t_m)^2}{t_m^2}} & \text{otherwise} \end{cases}, \quad (5)$$

where  $t_p$  is the pulse length and  $t_m$  designates peaks of the triangular and "gaussian" pulse. Neglecting the loss of the heat irradiated from the

front surface (it has been estimated to be typically six orders of magnitude smaller than the incoming flux), Eq.(1) is solved subject to the following initial and boundary conditions:

$$T(x,t=0) = T_0 \quad (6)$$

$$\frac{\partial T(x=0,t)}{\partial x} = 0 \quad (7)$$

$$T(x=\ell,t) = T_0 \quad , \quad (8)$$

where  $\ell$  is the sample thickness and  $T_0$  is temperature of the heat sink at the back side of the sample.

It is possible to develop analytical methods for solving Eq. (1) by using Green's function techniques if  $c_p$  and  $\kappa$  are constants; however, these are not applicable if  $c_p$  or  $\kappa$  are functions of temperature. Therefore, in order to solve Eq. (1), computational methods were used. These are described in Attachment 1, "Program THDIFFS." The shapes of the thermal conductivity  $\kappa = \kappa(T)$  used for silicon and GaAs, are shown in Figure 1a and 1b, respectively.

### RESULTS

Thermal distributions for several cases of interest were obtained. The distributions were obtained for GaAs and silicon for various values of the optical absorption coefficient, incident laser power, pulse length and shape. The temperature was calculated as a function of the distance away from the semiconductor surface, for various times after the application of the laser pulse. Several representative cases are listed in Table 1. The corresponding graphical plots are shown in Figures 2-10.

The first case (Figure 2) is for  $\alpha = 10^2 \text{ cm}^{-1}$ . This comparatively weak absorption corresponds to the tail of the silicon absorption edge, such as for the absorption of Nd:Yag laser in silicon. Figures 3-6 correspond to ruby laser absorption in silicon ( $\alpha = 5 \times 10^3 \text{ cm}^{-1}$ ), and Figures 7-10 to ruby laser absorption in GaAs ( $\alpha = 5 \times 10^4 \text{ cm}^{-1}$ ). The cases shown are for the

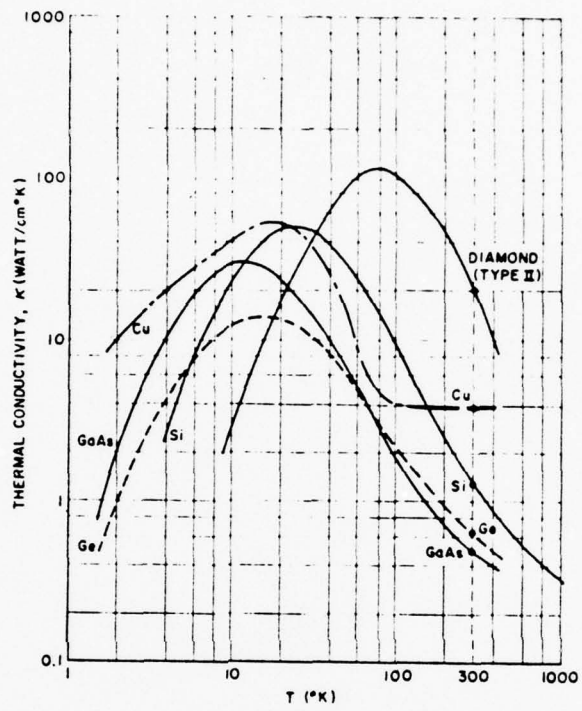


Figure 1. Measured thermal conductivity vs. temperature for pure Ge, Si, GaAs, Cu and diamond type II. The thermal conductivity is lower than indicated here for samples with high impurity concentrations.

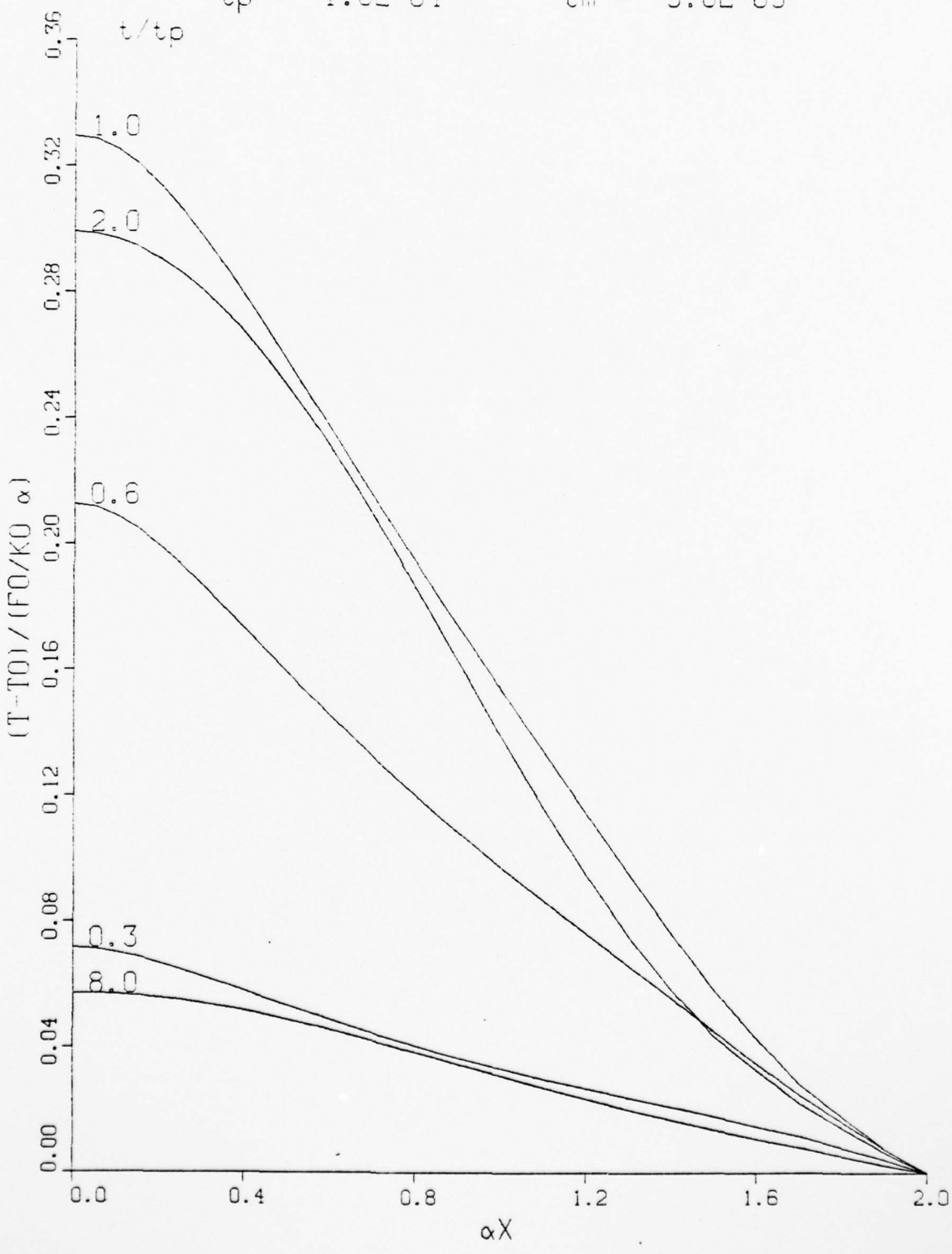
Table I  
THERMAL DISTRIBUTION CASES

Material	$\alpha$ ( $\text{cm}^{-1}$ )	$t_m$ (sec)	$F_0$ ( $\text{W/cm}^2$ )	Pulse Shape
Silicon	$10^2$	$5 \times 10^{-5}$	$5 \times 10^5$	Gaussian
		$5 \times 10^{-9}$	$3 \times 10^7$	
		$5 \times 10^{-9}$	$2 \times 10^7$	Gaussian
		$1.5 \times 10^{-8}$	$2 \times 10^7$	
		$2.5 \times 10^{-7}$	$2 \times 10^7$	
GaAs	$5 \times 10^3$	$1.5 \times 10^{-8}$	$5 \times 10^6$	
		$1.5 \times 10^{-8}$	$1 \times 10^7$	
		$5 \times 10^{-9}$	$1 \times 10^7$	
		$1 \times 10^{-9}$	$1 \times 10^7$	Gaussian

"Gaussian" pulse shape. Temperature profiles created by the triangular pulse have also been evaluated. As expected, there is no significant difference between profiles created by the various pulse shapes. No losses such as the reflection losses were considered; therefore, the listed powers are the actually absorbed powers.

The profiles are shown as a function of the distance away from the front surface, with time (in fractions and multiples of the pulse length,  $t_p$ ) as a parameter. The initial rise and decay of the temperature pulse after the end of the laser pulse are clearly seen. In the cases shown,

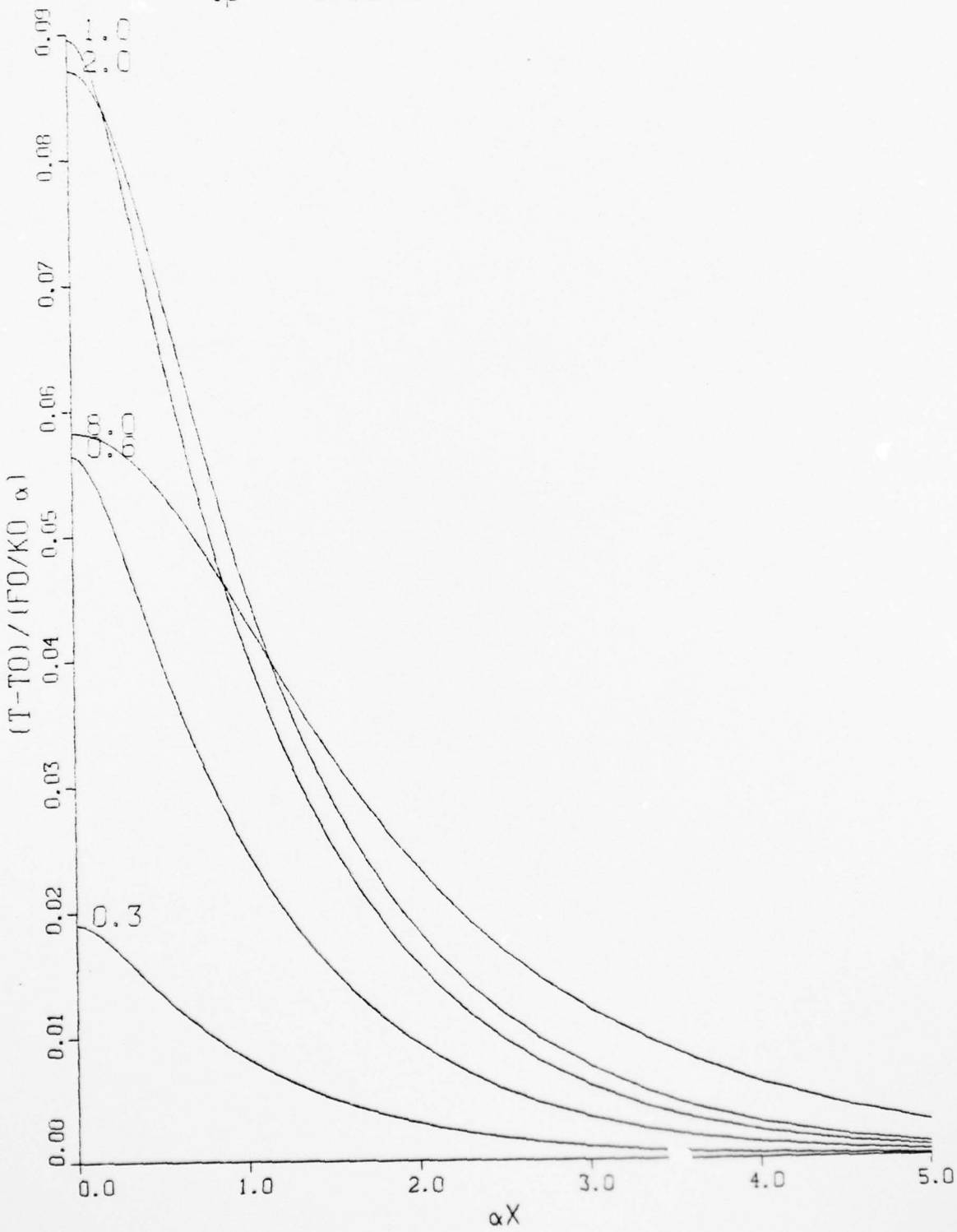
JOB XGEN004 PLOT NO. 1 TIME 16.21 DATE 10/13/78 015SP1B, TNS/TSS V.1



JOB N808022 PLOT NO. 3 TIME 11.12 DATE 10/13/78 DISSPLA, TRN/TSS V.1

1. 1. 2 /

Figure 3.  
THERMAL DIFFUSION FOR SILICON  
 $\alpha = 5.0E+03$        $T_0 = 300$   
 $F_0 = 3.0E+07$ , GAUSSIAN  
 $t_D = 1.0E-08$        $t_m = 5.0E-09$



JOB

PLOT NO. 4

M808022

L...&gt;2

Figure 4.

## THERMAL DIFFUSION FOR SILICON

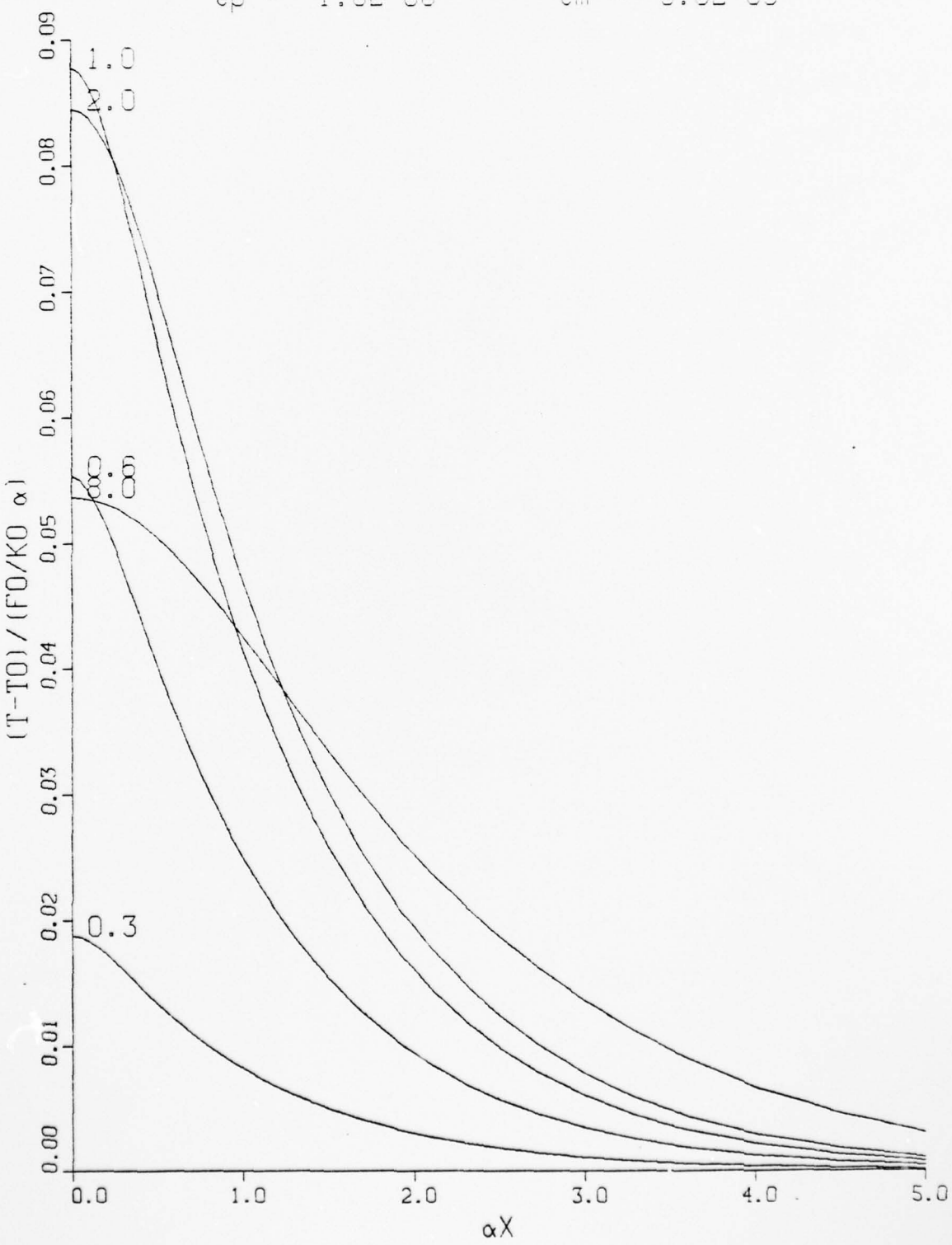
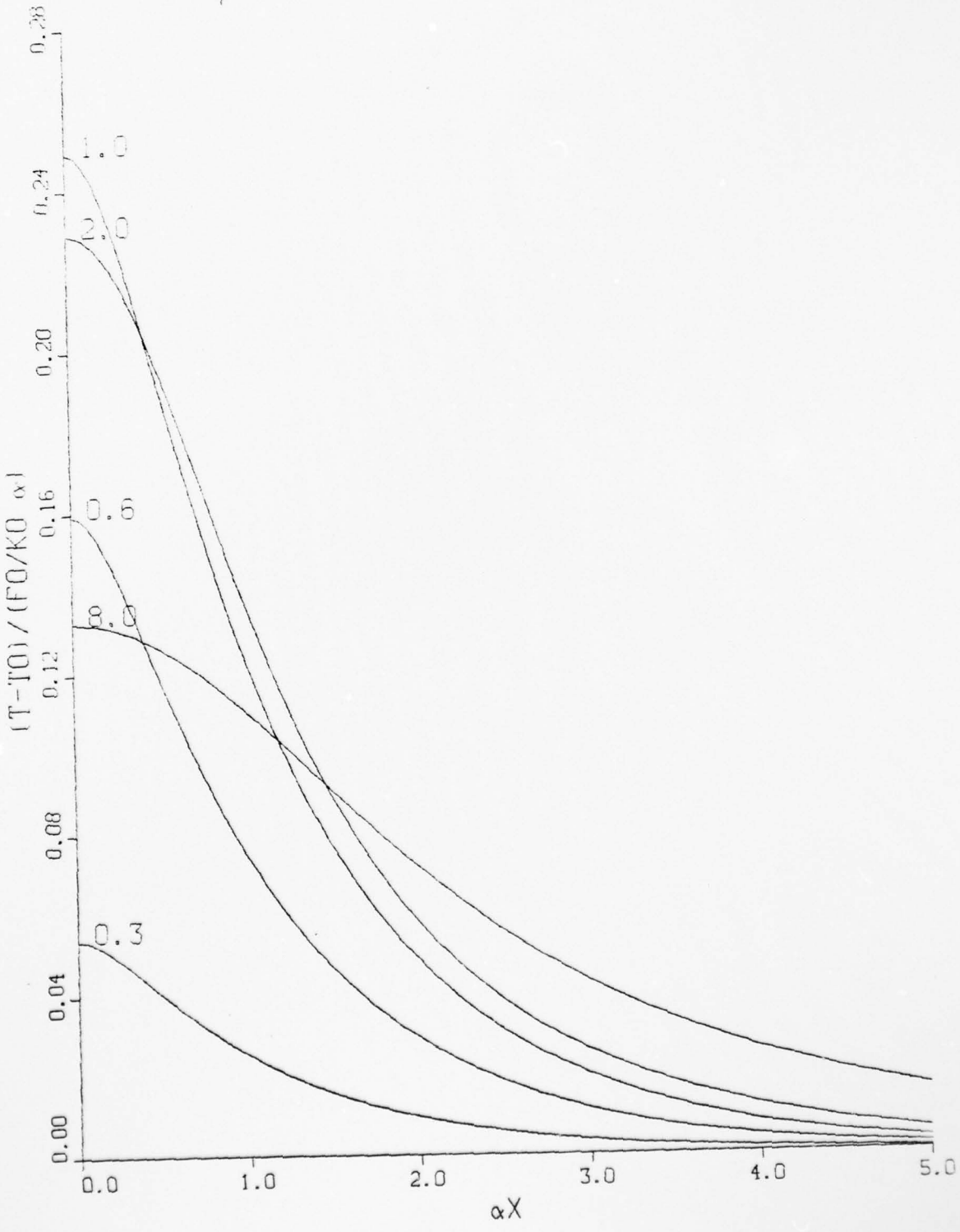
 $\alpha = 5.0E+03$        $T_0 = 300$  $F_0 = 2.0E+07$ , GAUSSIAN $t_p = 1.0E-08$        $t_m = 5.0E-09$ 

Figure 5.

Thermal Diffusion for Silicon

$\alpha = 5.0E+03$        $T_0 = 300$   
 $t/t_p$        $F_0 = 2.0E-07$ , GAUSSIAN  
 $t_p = 3.0E-06$        $t_m = 1.5E-06$



JOB VMXCO01 PLOT NO. 1 TIME 11.96 DTIME 01.12729

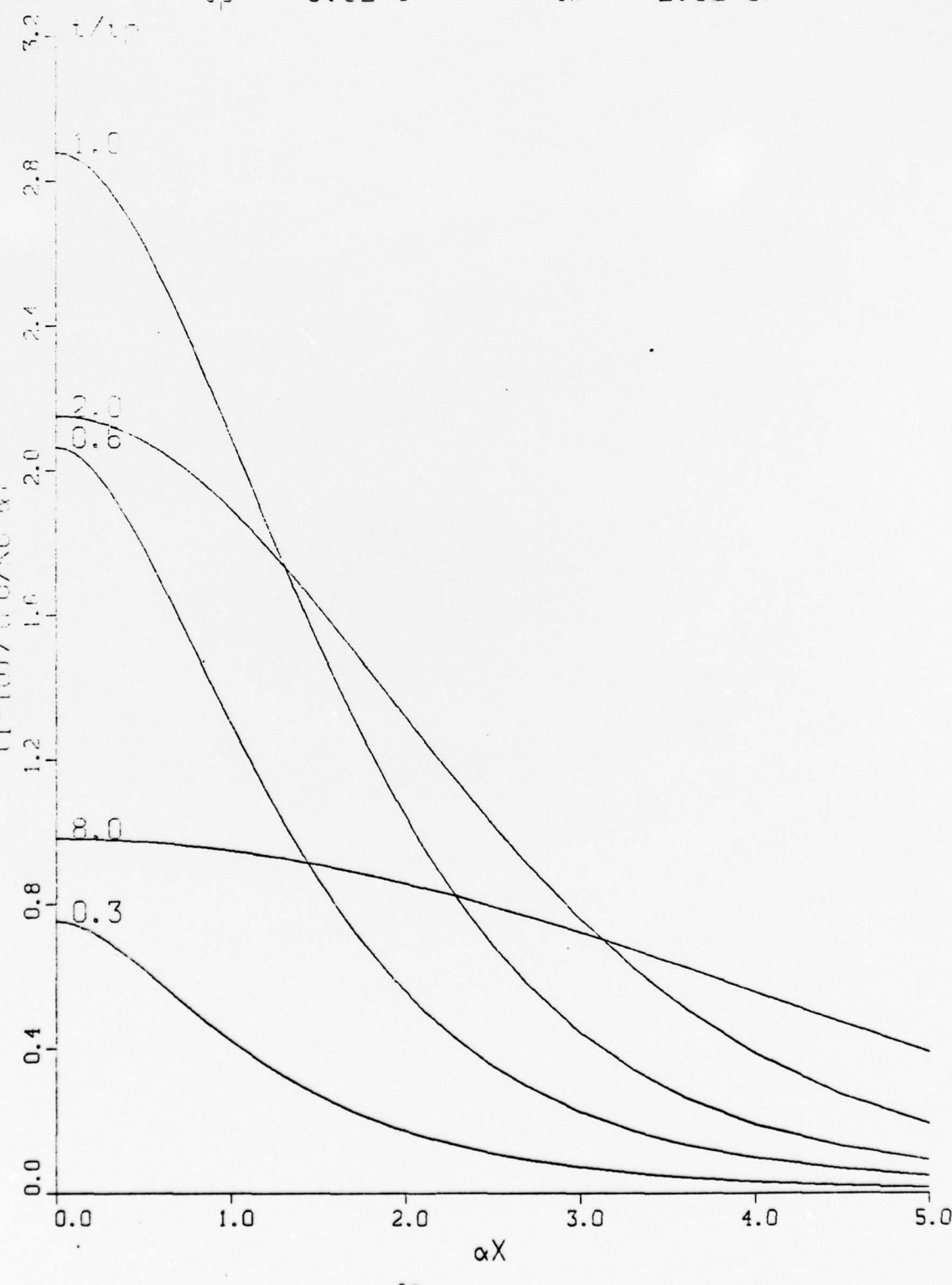


Figure 7.  
 THERMAL DIFFUSION FOR GaAs  
 $\alpha = 5.0E+04$        $T_0 = 300$   
 $F_0 = 5.0E+06$ , GAUSSIAN  
 $t_p = 3.0E-08$        $t_m = 1.5E-08$

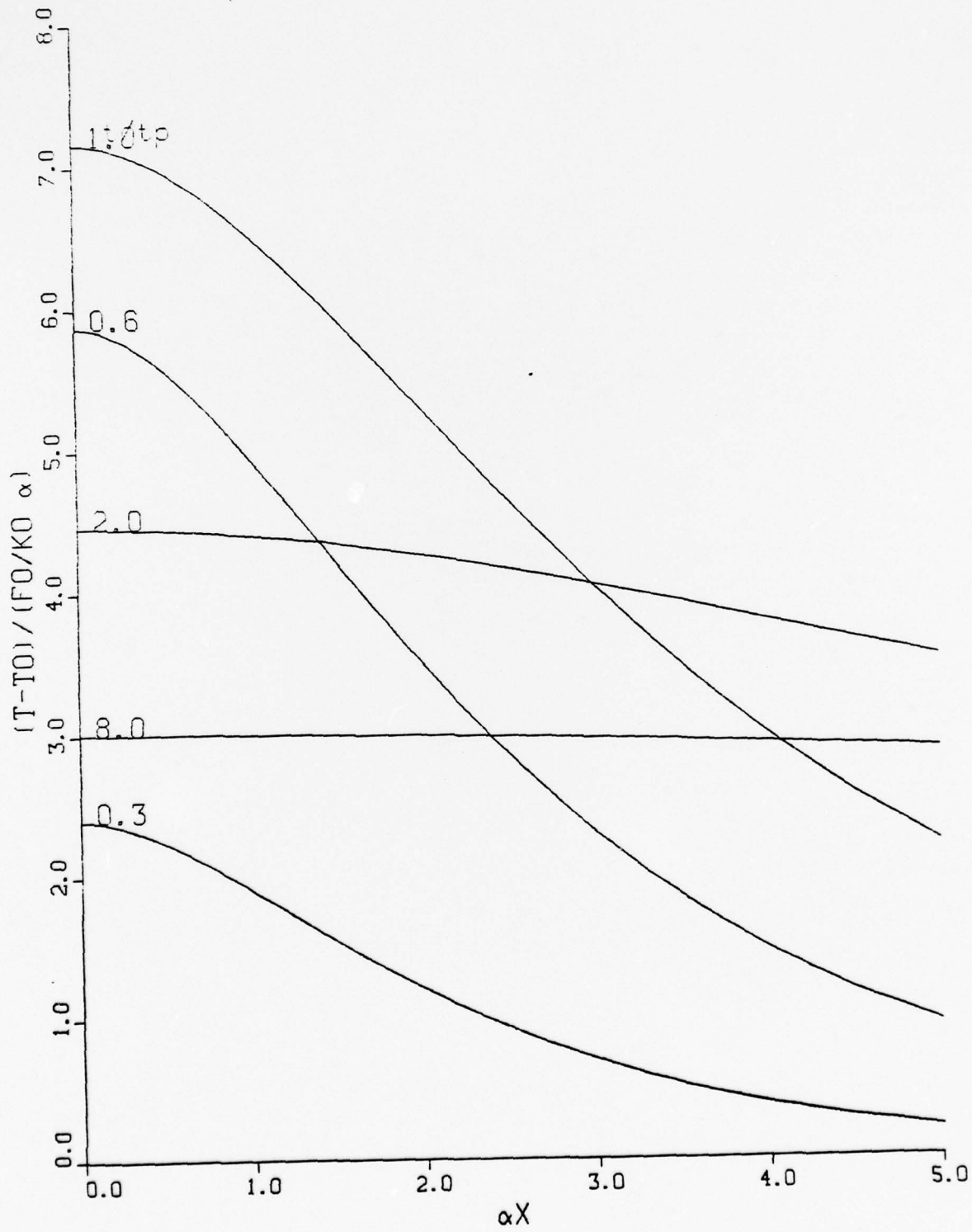


Figure 8.

THERMAL DIFFUSION FOR GaAs

$\alpha = 5.0E+04$        $T_0 = 300$

$F_0 = 1.0E+07$ , GAUSSIAN

$t_p = 3.0E-08$        $t_m = 1.5E-06$

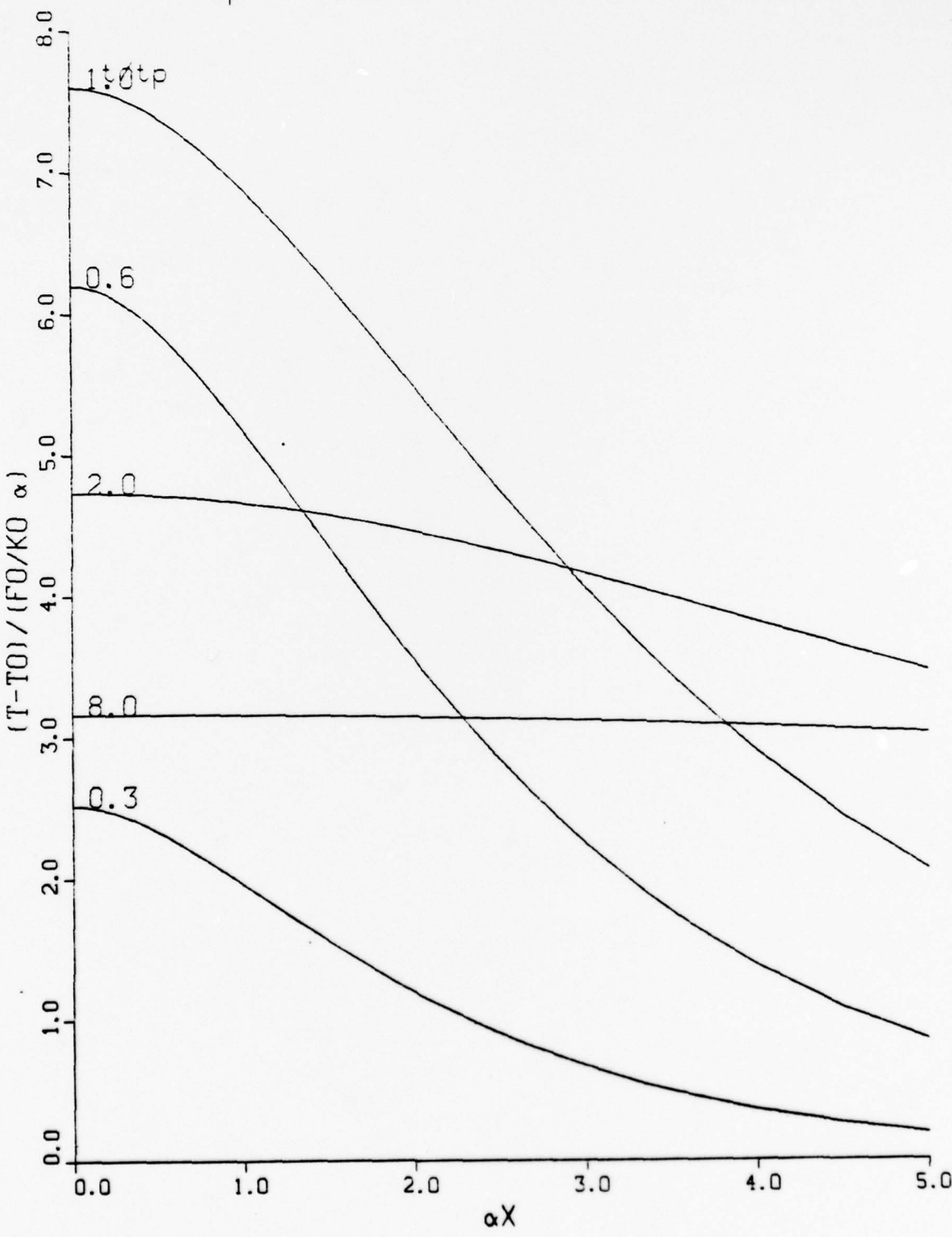


Figure 8a

THERMAL DIFFUSION FOR GaAs

$\alpha = 5.0E+04$        $T_0 = 300$

$F_0 = 1.0E+07$ , GAUSSIAN

$t_p = 3.0E-08$        $t_m = 1.5E-08$

$\kappa = \text{const} (= 0.5)$

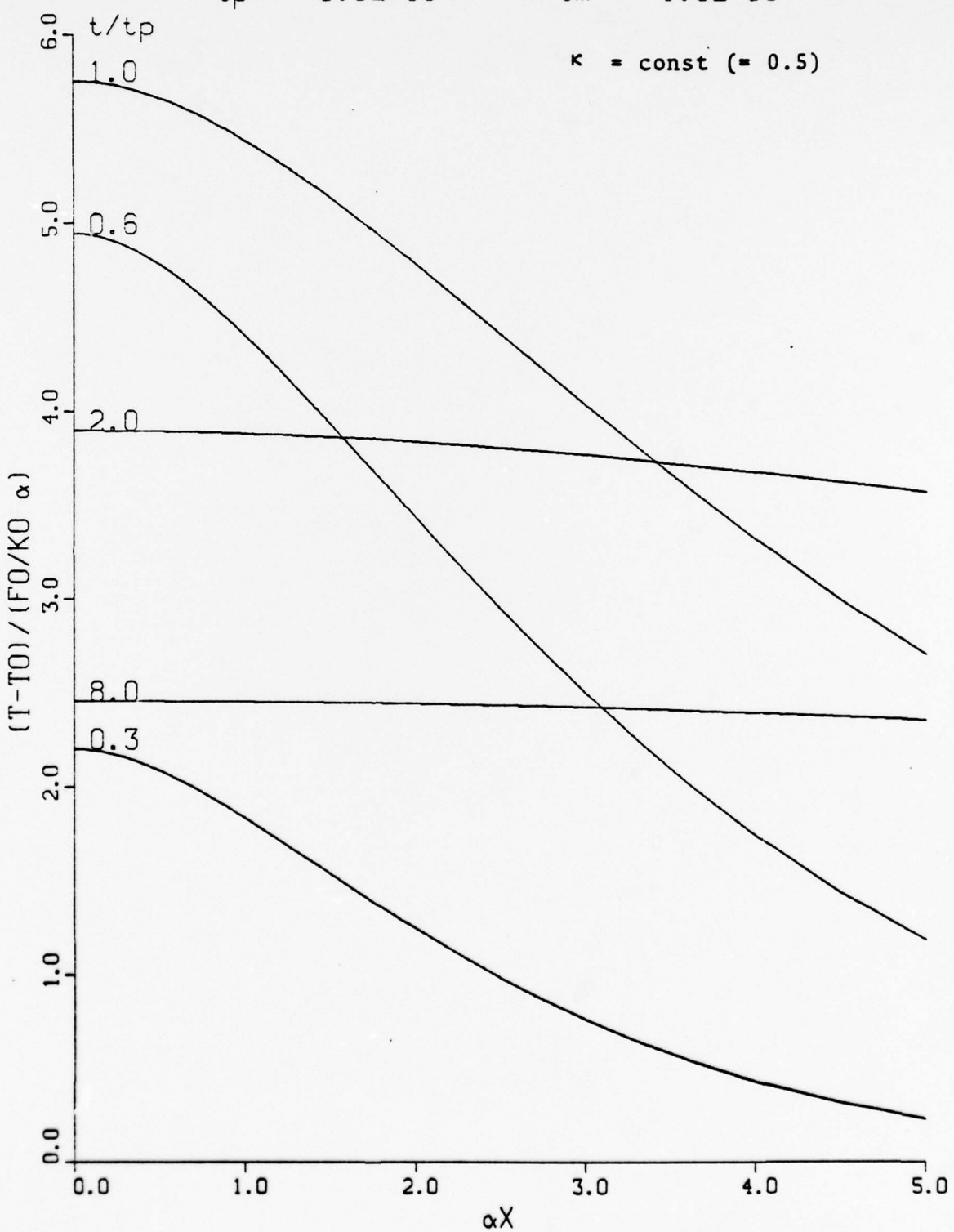


Figure 9.

THERMAL DIFFUSION FOR GaAs

$\alpha = 5.0E+04$        $T_0 = 300$

$F_0 = 1.0E+07$ , GAUSSIAN

$t_p = 1.0E-08$        $t_m = 5.0E-09$

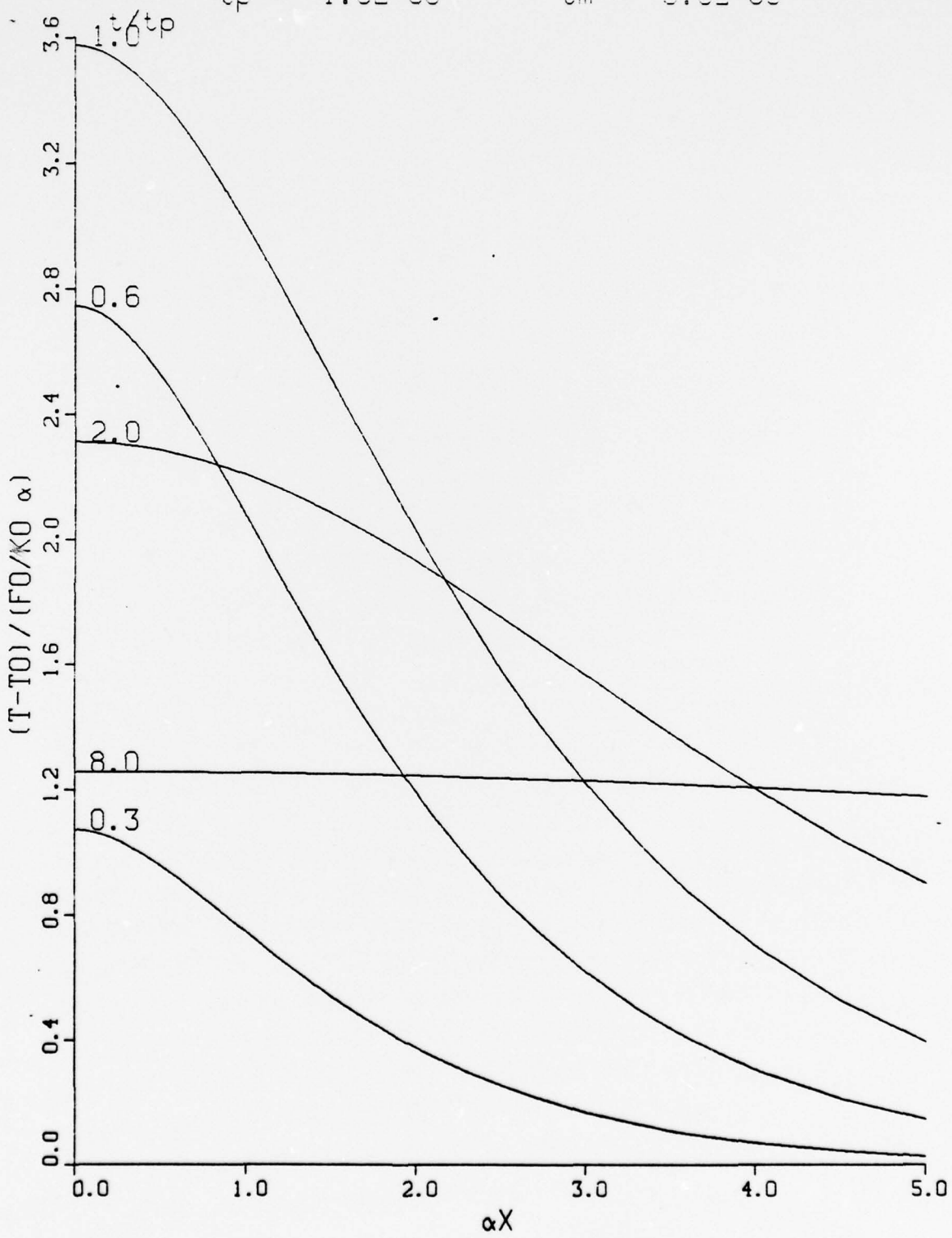


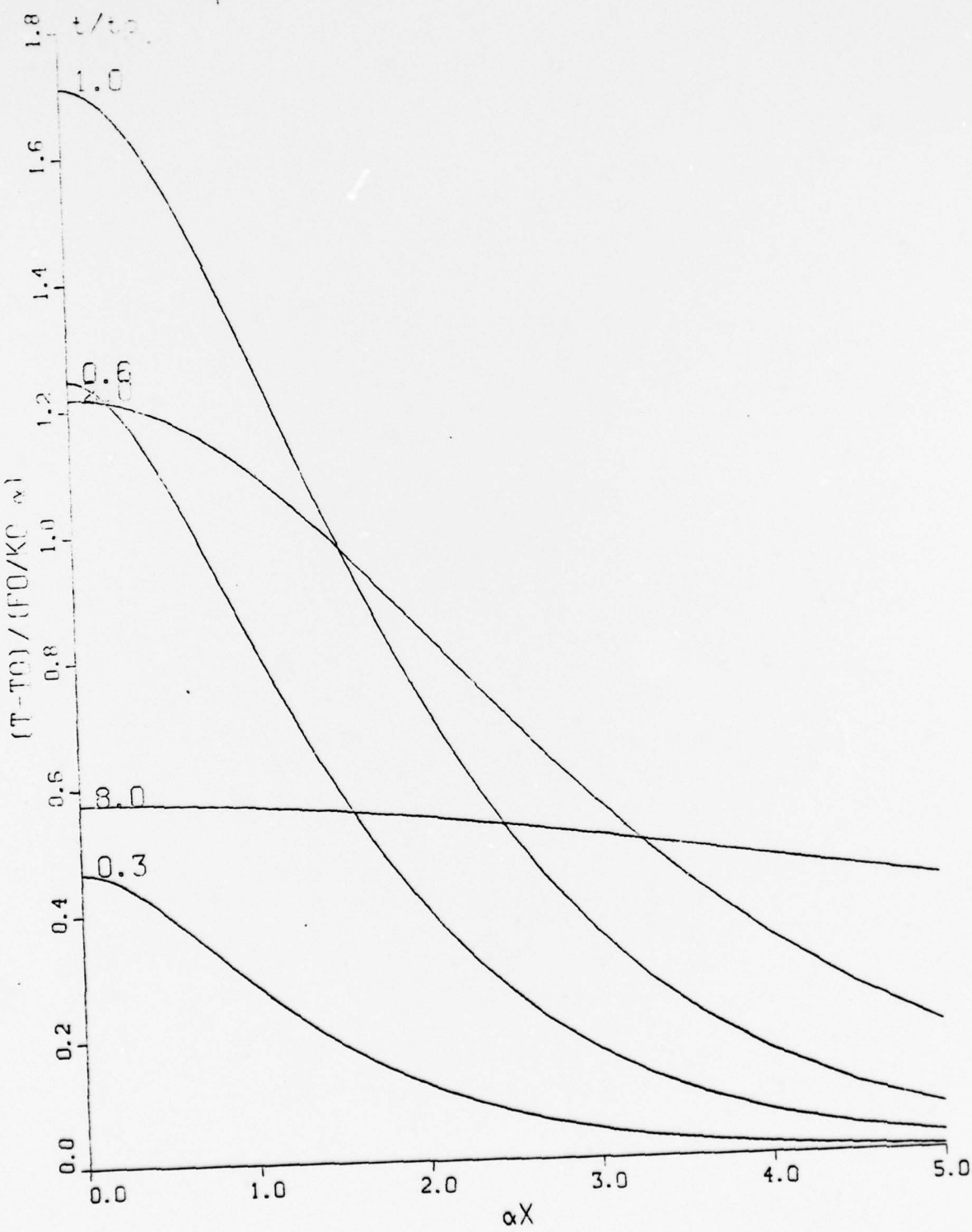
Figure 10.

THERMAL DIFFUSION FOR GOF

$\alpha = 5.0E+04$        $T_0 = 300$

$F_0 = 1.0E+07$ , GAUSSIAN

$t_p = 2.0E-09$        $t_m = 1.0E-09$



the surface temperature reaches the maximum value at the "end" of the laser pulse, i.e., at the time  $t_p = 2t_m$ , where  $t_m$  designates the pulse peak. After the end of the laser pulse, the surface temperature rapidly drops, to about 1/3 of its maximum value in the time interval of  $10 t_p$ . Simultaneously with the application of the laser pulse, the created heat propagates into the crystal bulk. In all cases shown (except Figure 2), the thermal profile broadens after the end of the laser pulse, according to the thermal transport relation,  $x^2 \approx 4\kappa_p t/c_p$ . Figure 2 does not show this type of broadening of the thermal pulse; this is because of the overall rather wide temperature distribution, in this case due to the comparatively weak absorption.

Inspecting Figures 2-10, the effects of varying the laser power, pulse length, and optical absorption coefficient are clearly seen. Comparing Figures 3 and 4, and 7 and 8, it is clear that for all other parameters being equal, the maximum surface temperature increases linearly with the laser peak power. Comparison of Figures 4, 5 and 6, and 8, 9 and 10 shows the effect of pulse length on halfwidth of the thermal distribution and the surface temperature. The maximum surface temperature follows the approximate relationship,

$$T_s - T_0 \approx \frac{F_0 t_p}{c_p} \frac{1}{\ell_{eff}} , \quad (9)$$

where  $\ell_{eff}$  is the effective halfwidth of the thermal distribution at  $t = t_p$ ,

$$\ell_{eff} = \sqrt{\frac{1}{(2\alpha)^2} + \frac{t_p \kappa}{2c_p}} . \quad (10)$$

That is,  $\ell_{eff}$  is the larger of the quantities  $(2\alpha)^{-1}$  and  $(\kappa t_p / 2c_p)^{1/2}$ . For fast thermal diffusion ( $\alpha^{-1} < \sqrt{\kappa t_p / c_p}$ ), the region of the high

temperature is limited by the thermal diffusion length (within the pulse duration). For slow thermal diffusion, the region is limited by the penetration depth of the laser radiation. The widths of the profiles (silicon) in Figures 3, 4 and 5 are optical absorption depth-limited ( $t_p \lesssim 10^{-7}$  sec). The profile in Figure 6 is thermal diffusion-limited ( $t_p \gtrsim 10^{-7}$  sec). For GaAs, the widths of the curves in Figures 7, 8 and 9 are thermal diffusion-limited ( $t_p \gtrsim 10^{-9}$  sec), and in Figure 10 optical penetration depth-limited ( $t_p \lesssim 10^{-9}$  sec). The optical penetration depth-limited profiles (short pulses) are generally narrower than the thermal diffusion-limited profiles.

Equations 9 and 10 say that for sufficiently short pulses,  $T_s$  grows linearly with  $t_p$ . That this is indeed the case is immediately seen by comparing Figures 4 with 5 and 8 with 9. For long pulses, this increase is slower, the surface temperature approaching saturation for very long pulses. Clearly, the heating is most efficient when  $t_p = t_{th} = c_p/\kappa\alpha^2$ .

## II. IMPURITY REDISTRIBUTION

### PROBLEM

Redistribution of impurities induced by the elevated temperature during the application of the laser pulse to the semiconductor surface is obtained by solving Fick's laws for impurity diffusion,

$$\frac{\partial N}{\partial t} = \frac{\partial}{\partial x} (D \frac{\partial N}{\partial x}) , \quad (11)$$

where the diffusion coefficient  $D$  is a material parameter characterizing the rate of the diffusion, which, for solids, increases steeply with temperature according to the exponential law,

$$D(t) = D_0 \exp(-\frac{E_A}{kT}) , \quad (12)$$

where  $E_A$  is activation energy for impurity diffusion, and the temperature inside the semiconductor,  $T = T(x,t)$ , is the solution of Eq. (1). Equation (11) describes time development of the impurity concentration, whatever the initial distribution may be. In the absence of an external source of the impurities, Eq. (11) is subject to the following boundary conditions,

$$\frac{\partial N(x=0,t)}{\partial x} = 0 \quad (13)$$

$$\frac{\partial N(x=\ell,t)}{\partial x} = 0 \quad . \quad (14)$$

The initial condition is distribution of impurities before the application of the laser pulse,

$$N(x,t=0) = N_0(x) \quad . \quad (15)$$

Since Eq. (11) is a nonlinear second order partial differential equation, it again has to be solved numerically.

#### NUMERICAL METHODS

Equation (11) can be solved by using the same numerical code which was used for computation of the thermal diffusion, Eq. (1), and described in the preceding section. However, there is one important difference between the thermal and impurity diffusion. Whereas there is a very rapid thermal diffusion after the application of a single laser pulse, the impurity diffusion is very slow. Before applying the code to Eq. (11), it is therefore very important to realize that Eq. (11), with the initial condition, Eq. (14), describes time development of impurity distribution during the application of one laser pulse. Due to the very slow impurity diffusion (in the solid phase of the semiconductor), the diffused distances during one laser pulse will be very small. Assuming an average diffusion constant of  $D = 10^{-10} \text{ cm}^2 \text{ s}^{-1}$  during the pulse duration of  $t_p \approx 25 \text{ nsec}$ , the number of pulses,  $n$ , which have to be applied to the semiconductor in order to achieve impurity diffusion of, say,  $100 \text{ \AA}$ , is

$$n = \frac{x^2}{4Dt_p} \approx \frac{10^{-12}}{4 \times 10^{-10} \times 2.5 \times 10^{-8}} \approx 10^5 \quad , \quad (16)$$

which is rather large. Since it is quite unreasonable to ask the computer to solve Eq. (11) repeatedly  $10^5$  or more times, we have reformulated the problem such that, in the new formulation, we seek development of impurity concentration as a function of the number of the applied pulses, rather than in time. This has been done as follows.

Assuming that solution of Eq. (10) at time  $t = t_0$  is  $N(x, t_0)$ , the formal solution of distribution  $N(x, t)$  at some later time  $t$  is

$$N(x, t) = U(t, t_0, \frac{\partial}{\partial x}, \frac{\partial^2}{\partial x^2}, \dots) N(x, t_0) , \quad (17)$$

where the time-development operator  $U$  is

$$U = \exp \left\{ \int_{t_0}^t dt' \frac{\partial}{\partial x} (D \frac{\partial}{\partial x}) \right\} . \quad (18)$$

Assuming that the  $n$ -th laser pulse was applied at time  $t_0 = 0$ , and  $(n+1)$ th pulse at the later time  $t$ , and that the length of the laser pulse  $t_p$  is much shorter than the time interval between the application of the pulses,

$$t_p \ll t - t_0 , \quad (19)$$

the distribution which is obtained as the result of the application of the  $n$ th pulse is then equal to

$$N(x, \infty) = U(\infty, 0, \frac{\partial}{\partial x}, \frac{\partial^2}{\partial x^2}, \dots) N(x, 0) , \quad (20)$$

where  $N(x, \infty)$  and  $N(x, 0)$  are the final distribution resulting from the application of the  $n$ th and  $(n-1)$ th pulse, respectively (final distribution after the application of the  $(n-1)$ th pulse is the initial distribution before the application of the  $n$ th pulse). Equation (20) may then be rewritten as

$$N_n(x) = U(\infty, 0, \frac{\partial}{\partial x}, \frac{\partial^2}{\partial x^2}, \dots) N_{n-1}(x) , \quad (21)$$

where the operator

$$U = \exp \left( \int_0^\infty dt' \frac{\partial}{\partial x} (D \frac{\partial}{\partial x}) \right) , \quad (22)$$

and where  $N_n(x)$  is the final distribution after the application of the  $n$ th pulse. Equations (21) and (22) describe the development of impurity distribution as a function of the number of applied pulses.

Equation (21) is evaluated by expanding the time development operator  $U$  into the power series,

$$U = 1 + \int_0^\infty dt' \frac{\partial}{\partial x} (D \frac{\partial}{\partial x}) + \text{higher order terms} . \quad (23)$$

Using Eq. (23), Eq. (24) then becomes

$$N_n(x) = \left( 1 + \frac{\partial}{\partial x} \int_0^\infty dt' (D \frac{\partial}{\partial x}) \right) N_{n-1}(x) , \quad (24)$$

where we have neglected the higher order terms of Eq. (23) due to the extreme slowness of the diffusion. Defining "integrated diffusivity"  $M(x)$  by the expression,

$$M(x) = \int_0^\infty dt' D(x, t') , \quad (25)$$

Equation (22) is finally rewritten as

$$\frac{\partial N(x, v)}{\partial v} = \frac{\partial}{\partial x} \left( M(x) \frac{\partial}{\partial x} N(x, v) \right) , \quad (26)$$

where, for small changes in  $N_{n-1}(x)$  to  $N_n(x)$ , we have replaced the discrete steps in  $n$  by the continuous variable  $v$ .

Equation (26), with the integrated diffusivity, Eq. (23), is our final equation used for computation of the impurity distribution. It gives distribution of impurities as a function of the number of the applied pulses,  $v$ , and is solved numerically by using the same numerical code which was used for solution of the thermal equation, Eq. (1). The computational methods are described in Attachment 1, "Program IMPDIFS."

## RESULTS

Impurity distributions were obtained for several cases of interest. Three examples of the calculated distributions are shown in Figures 11, 12 and 13.

Figures 11 and 12 show distributions obtained after the application of  $10^4$  laser pulses to silicon in the absence of an external impurity source. The initial impurity profiles were assumed Gaussian with halfwidths of  $\sigma = 0.1$  and  $0.5 \mu\text{m}$ , respectively. The activation energy for diffusion,  $Q$ , was assumed to be 2 eV, and the diffusion constant,  $D_0$ , was  $1 \text{ cm}^2/\text{sec}$ . The peak laser power utilized for heating the material was  $F_0 = 1.5 \times 10^7 \text{ W/cm}^2$ , the pulse was triangular with length  $t_p = 30 \text{ nsec}$ . The optical absorption coefficient  $\alpha = 10^4 \text{ cm}^{-1}$ . The material was silicon. The distributions are plotted as a function of the distance away from the semiconductor surface. Both the initial and the final ( $10^4$  pulses) distributions are shown.

The common feature of Figures 11 and 12 is the qualitative change in the shape of the modified distributions. In both cases, the impurities diffuse away from the semiconductor surface into the bulk. However, since the semiconductor interior is "cold", thus preventing it in any significant impurity diffusion, impurity profiles tend to "bulge" beneath the semiconductor surface at a distance which depends on the optical penetration depth, pulse length and halfwidth of the initial impurity distribution. This results in profiles which (after application of many laser pulses) are steep, approaching an abrupt "step" junction.

There are quantitative differences between Figures 11 and 12. The figures differ in the degree of modification of the initial profiles. For the initial halfwidth much smaller than the optical penetration depth, the high temperature affects all impurities. For the initial halfwidth on the order of, or wider than, the optical penetration depth, impurities located somewhat farther away from the surface will not be affected by the high temperature. Thus, in the former case (Figure 11), the profiles will be modified considerably more than in the latter case (Figure 12). In the latter

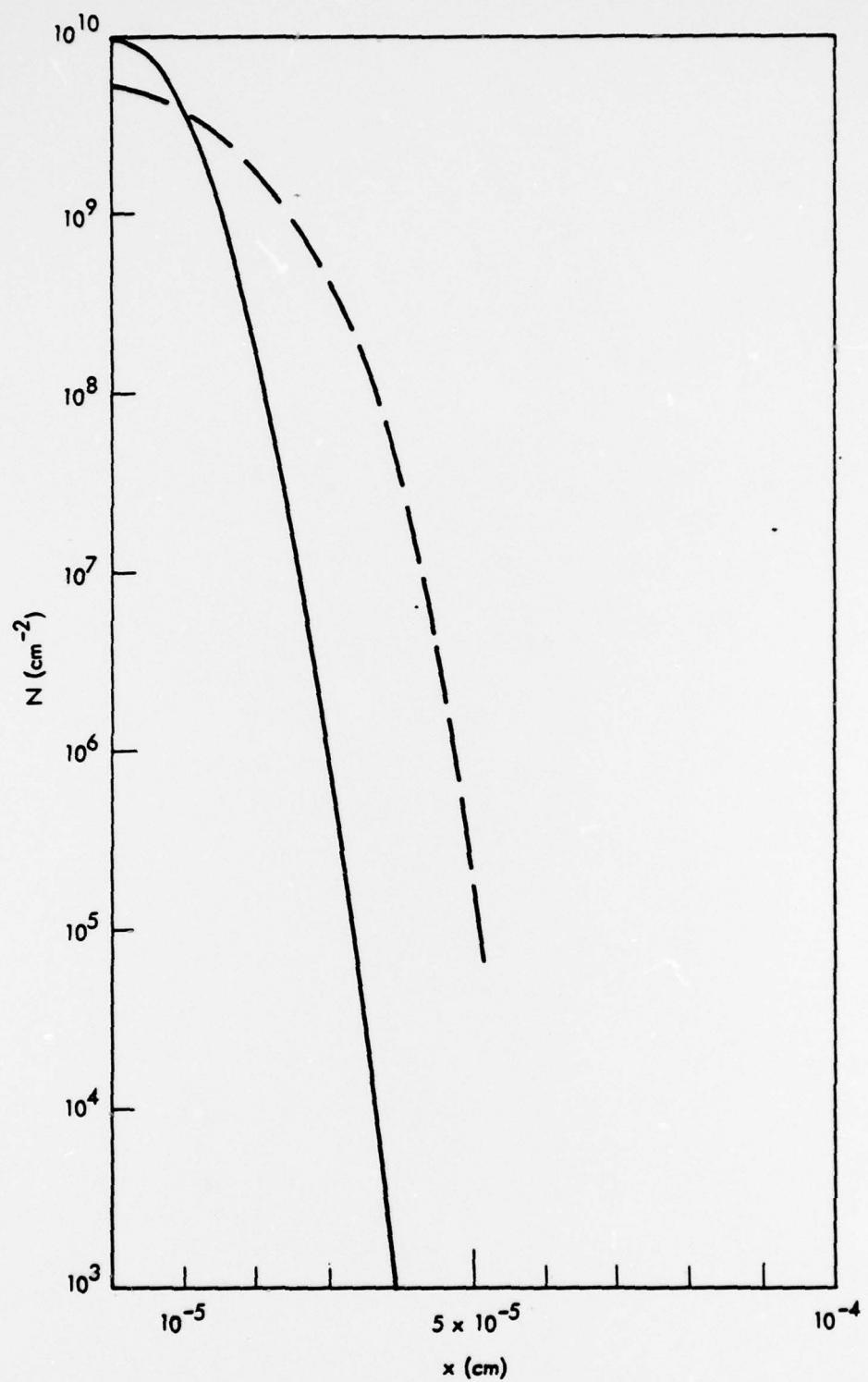
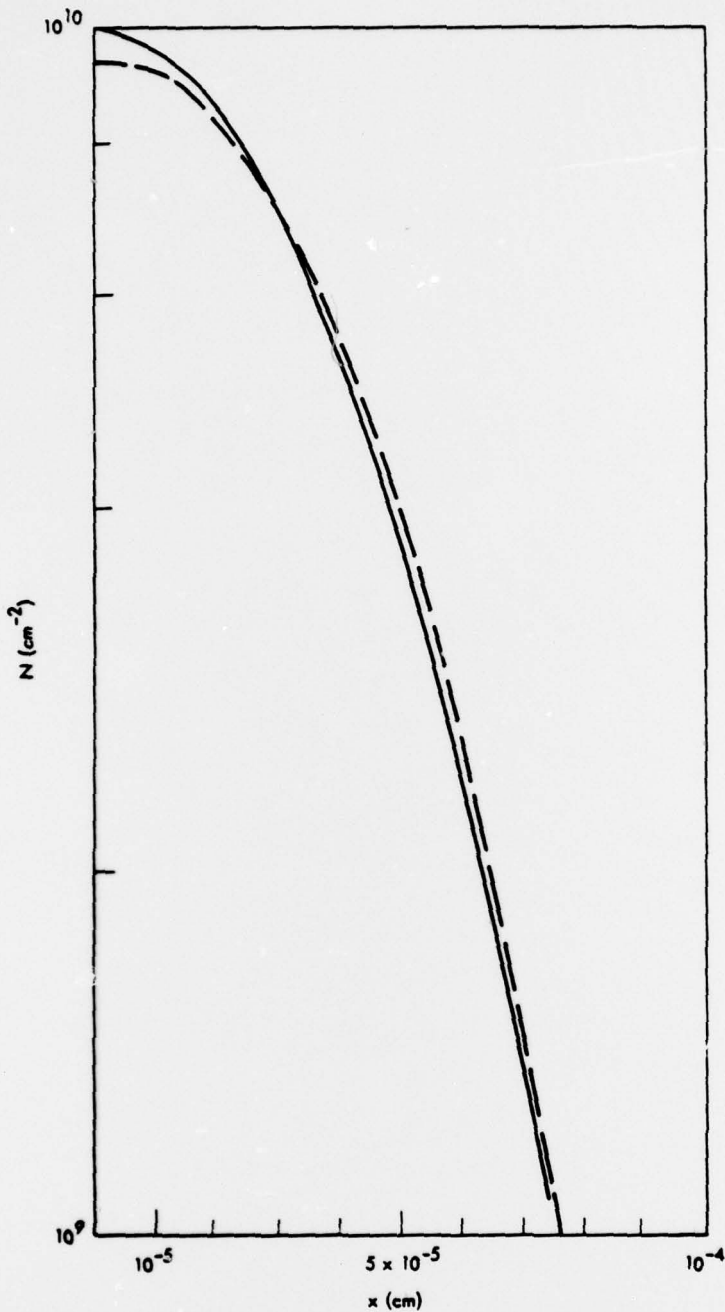


Figure 11. Impurity profiles before and after laser-induced diffusion. Laser parameters:  $F = 1.5 \times 10^7 \text{ W/cm}^2$ ,  $t = 20 \text{ nsec}$ , number of laser pulses  $10^4$  pulses. Optical absorption coefficient  $\alpha = 10^4 \text{ cm}^{-1}$ . Diffusion activation energy  $Q = 2 \text{ eV}$ , diffusion coefficient  $D_0 = 1 \text{ cm}^2 \text{ s}^{-1}$ . The initial distribution halfwidth  $\sigma = 0.1 \mu\text{m}$ .



**Figure 12.** Impurity profiles before and after laser-induced diffusion.  
 Laser parameters:  $F = 1.5 \times 10^7 \text{ W/cm}^2$ ,  $t = 30 \text{ nsec}$ , number of laser pulses  $10^4$  pulses. Optical absorption coefficient  $\alpha = 10^4 \text{ cm}^{-1}$ . Diffusion activation energy  $Q = 2 \text{ eV}$ , diffusion coefficient  $D_0 = 1 \text{ cm}^2 \text{ s}^{-1}$ . The initial distribution halfwidth  $\sigma = 0.5 \mu\text{m}$ .

case, impurities located at the distance  $\alpha^{-1}$  beneath the semiconductor surface will in effect, have been stopped. We have calculated profiles for the initial depths  $\alpha^{-1}$ , and also thicker than  $\alpha^{-1}$ . For  $10^4$  pulses, there was practically no change in the initial impurity distribution.

Figure 13 shows the distribution obtained after the application of  $10^4$  and  $10^6$  pulses. The material was GaAs with  $Q = 2$  eV,  $D_0 = 1 \text{ cm}^2/\text{sec}$ , and  $\alpha = 2 \times 10^4 \text{ cm}^{-1}$ . The initial impurity profile was gaussian with half-width  $\sigma = .5 \mu\text{m}$ . The laser pulse shape was gaussian, the effective pulse length was  $t_p = 10 \text{ nsec}$ , and the peak laser power was  $F_0 = 3 \times 10^7 \text{ W/cm}^2$ . The maximum temperature achieved in the semiconductor was its melting temperature.

The common feature of the  $10^4$  and  $10^6$  pulse curves is the qualitative change in the shape of the modified distribution. After the application of many laser pulses, the profiles become more abrupt than the initial distribution. Similarly, as in Figures 11 and 12, there is little quantitative change for  $10^4$  pulses. The profile clearly becomes an abrupt "step" junction after the application of  $10^6$  pulses. Thus, the application of many laser pulses with the optical absorption depth,  $\alpha^{-1}$ , matching the impurity profile halfwidth,  $\sigma$ , results in abrupt impurity profiles.

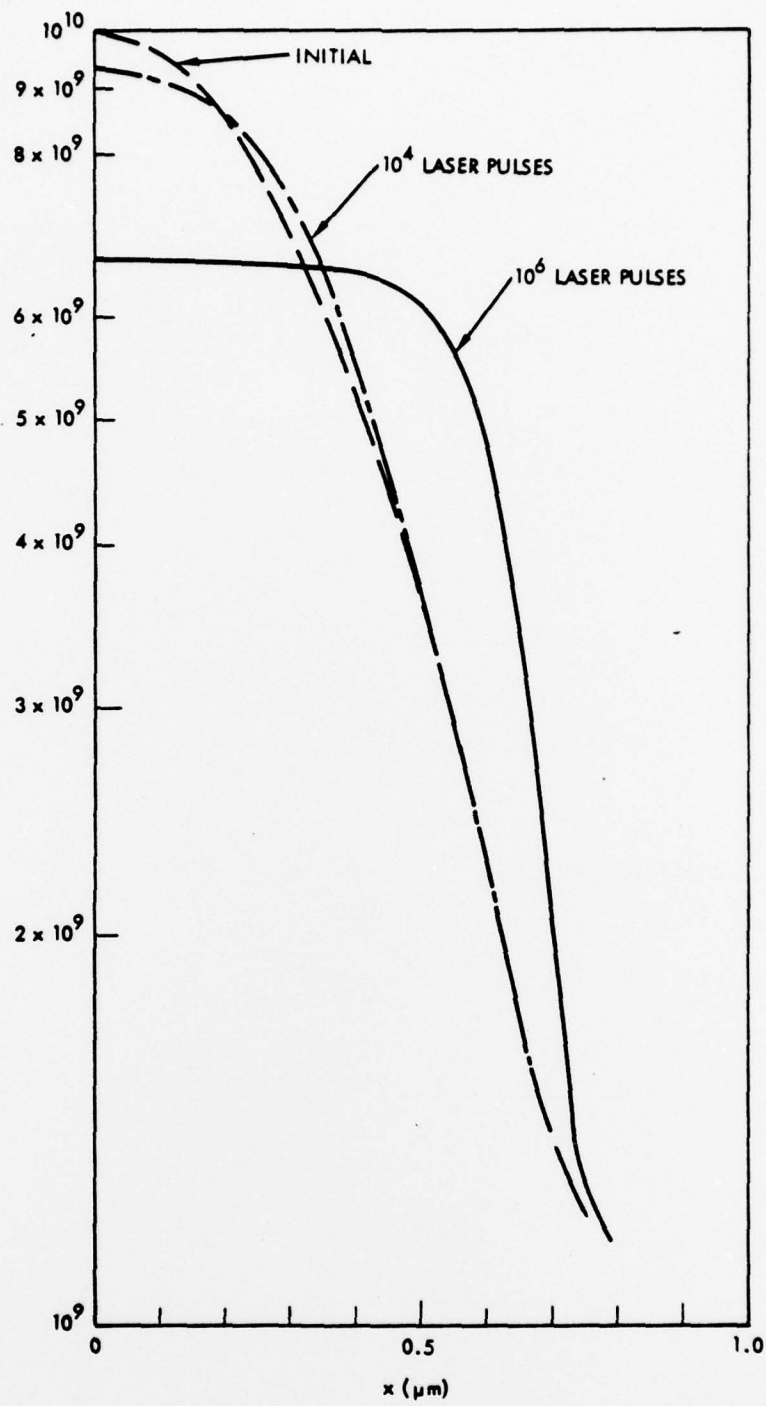


**Figure 13.** Impurity profile before and after laser-induced diffusion.  
 Laser parameters:  $F = 3 \times 10^7 \text{ W/cm}^2$ ,  $t_p = 10 \text{ nsec}$ ,  $\alpha = 2 \times 10^4 \text{ cm}^{-1}$   
 Material parameters: GaAs,  $Q = 2 \text{ eV}$ ,  $D_p = 1 \text{ cm}^2 \text{ s}^{-1}$ . The  
 initial impurity distribution halfwidth  $\sigma = .5 \mu\text{m}$  ( $\sigma = \alpha^{-1}$ ).  
 The laser pulse length is equal to the thermal diffusion time,  
 $t_p = t_{th} = c_p / \kappa \alpha^2$ .

## APPENDIX C

### RUBY LASER SYSTEM USED IN LASER PROCESSING EXPERIMENTS

#### 1.0 REQUIREMENTS

Desirable properties in a laser system for semiconductor processing are: controllable and spatially uniform energy density of 0 to  $2.5 \text{ J/cm}^2$  at the semiconductor surface. Pulse widths should be less than 50 or 100 nanoseconds, with even shorter pulses preferred. With the possible exception of beam uniformity, the ruby laser used in the LISP program performs nicely on all these counts.

#### 2.0 LASER SYSTEM DESCRIPTION

Figures 1 and 2 illustrate the optical layout of the laser. Not shown in the diagram are the flashlamp and Kerr cell drivers and the refrigerator and pump for the cooling water. The laser itself, the sample to be exposed and the beam monitoring instrumentation mount on one steel rail and a He-Ne alignment laser and an autocollimator mount on a parallel rail.

The laser consists of two parts, an oscillator and an amplifier. The mode of operation which has proved most effective in this program is to drive the oscillator hard to keep the pulse short and to obtain outputs of varying energy density (but constant pulse width) by adjusting the drive to the amplifier. The pulse width is unusually short for a laser of this type. By intention, the laser cavity was made as short as possible (40 cm), the outcoupling fraction is high (72% transmission) and the oscillator flashlamp is driven very hard. The pulse width from the oscillator varies from 8 nanoseconds at 4.8 kilovolts drive to 20 nsec at 4.3 kv drive (see Figure 3).

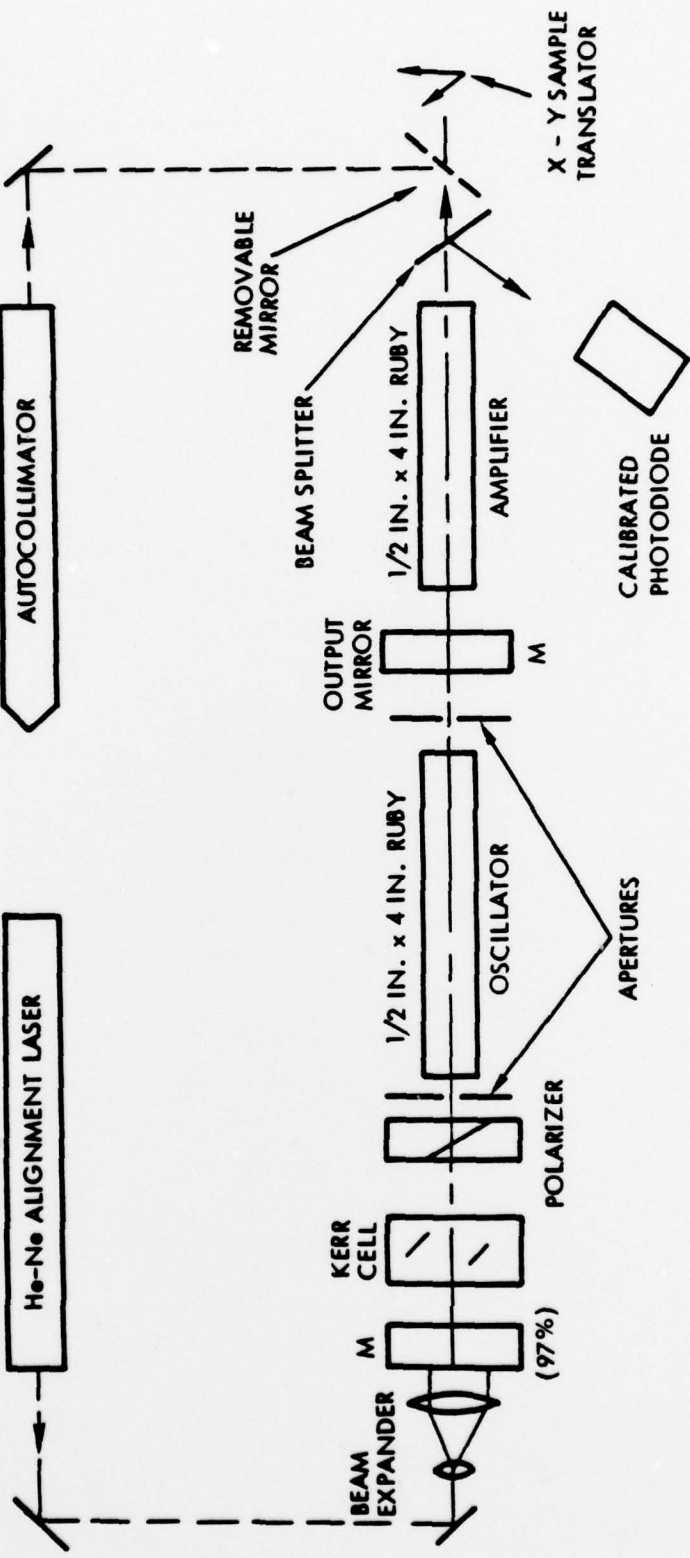


Figure 1. Schematic of Q-switch Ruby Laser Oscillator and Amplifier System Used in Laser Processing Experiments.

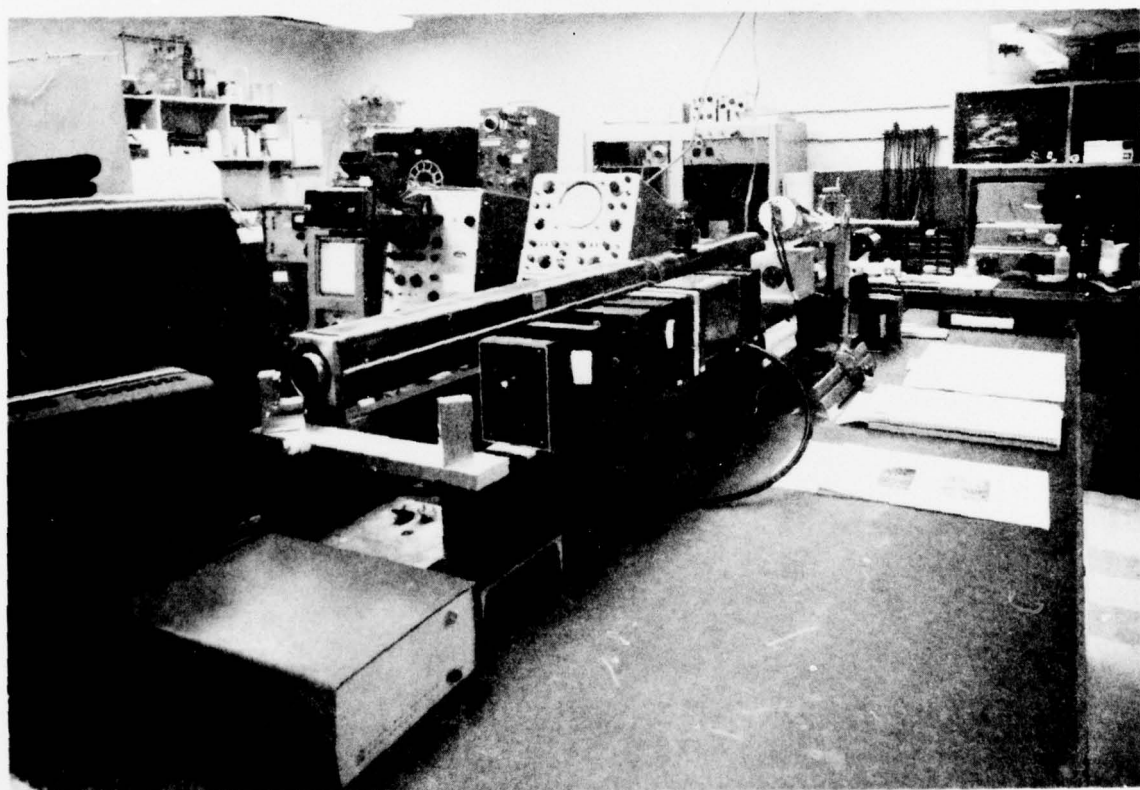
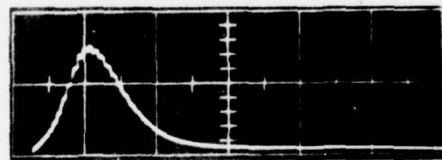


Figure 2. Photograph of Ruby Laser System Shown Schematically in Figure 1.



4.8 kv drive  
45 v/div, 20 nsec/div



4.3 kv drive  
18 v/div, 20 nsec/div

Figure 3. Pulse Shape vs Oscillator Drive Voltage

The amplifier provides 3X gain at 4.0 kv drive and 1X at 3.0 kv. Below 3 kv, the output is attenuated about a factor of two per 500 volts reduction in amplifier band voltage. Table 1 shows the range of energy densities available. The exact numbers for pulse width and output energy vary considerably when ruby rods or flashlamps are changed, but the qualitative behavior stays the same.

Table 1.

Energy Density of Laser Pulse vs Amplifier Bank Voltage  
With Oscillator Drive at 4.8 kv.

Pulse Width = 10 nsec FWHM For All Shots

Amplifier Drive kv	Energy Density j/cm <sup>2</sup>
4.0	2.51
3.5	1.56
3.0	.83
2.5	.36
2.0	.125